Experimental Investigation and Analysis of Chip Rebonding Phenomenon in Turning Superalloys

by

Jae Wook Oh

A dissertation submitted in partial fulfillment
of the requirements for the degree of
Doctor of Philosophy
(Mechanical Engineering)
in The University of Michigan
2013

Doctoral Committee:

Professor Jun Ni, Chair
Professor James R. Barber
Professor Xiaoqing Pan
David A. Stephenson, Ford Motor Co.

DEDICATION

To my family

ACKNOWLEDGMENTS

I would like to express my gratitude to all those who have contributed to this dissertation. In the first place, I would like to thank my advisor and mentor Professor Jun Ni throughout my academic career at the University of Michigan. This work would not have been possible without his trust and support. He oriented me in the correct direction and closely worked with me in all the time of research for and writing of this dissertation. I would also like to thank my dissertation committee members, Professors James Barber, Professor Xiaoqing Pan, and Dr. David Stehphenson, for their stimulating suggestions and comments that improved my study.

I am sincerely grateful to all those at GE Aviation for presenting me with challenging research opportunities, including Roger Lindle, Howard Weaver, and Kevin Meyer. Special thanks to all those in the S. M. Wu Manufacturing Research Center, Dr. Seungchul Lee, Dr. Cindy Kuo, Dr. Xiaoning Jin, Xianli Qiao, Xun Liu, Dr. Chaoye Pan, Dr. Adam Brzezinski, Ahmad Almuhtady, Dr. Hao Yu, Dr. Kwang-Hyun Park, Xi Gu, Dr. Saumil Ambani, Dr. Roland Chen, Dr. Li-Jung Tai along with many others. I would also like to thank Professor Sihyung Ryu and Dr. Hongseok Yoon for their stimulating suggestions and comments. Especially, I am deeply indebted to my writing advisor Elizabeth Hildinger for her support and encouragement.

Most importantly, I am forever indebted to my parents, the most caring and giving parents I know, whose trust and support enabled me to complete this work.. I would also like to thank my brother and sister, Jehong and Mihyang, who always show the boundless trust and love. Finally, I thank my loving wife, Jinsuk, for her consistent support and love.

TABLE OF CONTENTS

LIST OF FIGURES

LIST OF TABLES

LIST OF APPENDICES

ABSTRACT

Inconel 718, a representative superalloy, is widely used in the aerospace industries due to its high temperature endurance properties and good corrosion resistance. However, the machining of Inconel 718 generates more heat in the cutting zone than that of most other materials, which makes this material prone to surface defects. Among several possible surface defects, the chip rebonding phenomenon is investigated in this study. To avoid this defect and achieve a high surface quality, it is necessary to understand the mechanism of chip rebonding.

In order to identify the root causes of chip rebonding in turning Inconel 718, chip rebonding samples are observed. Overall observations of the machined surface show that chip rebonding occurs periodically along a feed mark, and that the chip's side edge is periodically torn and curled. On the basis of the observations, the torn chips at the side edge of the chip are assumed to be smeared periodically by the tool along the feed mark. A chip curl blocking device is designed in order to test this hypothesis and the test results with the chip curl blocking device are shown.

Residual stress distribution, which is important for material life, is affected by chip rebonding. When chip is bonded to the machined surface, it causes changes in residual stress distribution because it undergoes higher thermal expansion than the base material. To evaluate the chip rebonding effect on residual stresses, a FE model is developed to

simulate the chip rebonding phenomenon. The changes of residual stress distribution in subsurface material are simulated while chip rebonding occurs and after the material cools down. Subsurface residual stresses are measured by the nanoindentation method and compared with simulation results.

In order to identify the key variables that influence the occurrence of chip rebonding, a parametric study is performed in dry and wet cutting conditions. DOE is carried out to study the effect of each cutting parameter on chip rebonding in dry cutting. In wet cutting, various MWFs including pure water and two kinds of commercial lubricants in varying concentrations and viscosity are used to investigate their effect on chip rebonding occurrence.

This dissertation research provides an in-depth understanding of the chip rebonding phenomenon in turning of Inconel 718 and a method to control the machining conditions to avoid chip rebonding.

CHAPTER 1 INTRODUCTION

1.1 Overview

Superalloys are nickel, nickel-iron, and cobalt-based alloys generally used at temperatures above 540 ºC [1]. Superalloys have been developed and widely used in various fields because of their numerous advantages; they preserve their mechanical and chemical properties at high temperatures and have good corrosion resistance, as well as resistance to creep, thermal fatigue, and erosion [2].

Superalloys have a broad range of applications as shown in Table 1.1. The aircraft engines as shown in Figure 1.1 are representative examples of high temperature applications of superalloys. The alloys used in aviation engines had traditionally been alloys of steel, nickel, titanium and aluminum. Since aviation engines are limited by the weight and thermal capacity of the available materials, aluminum and steel have given way to superalloys with properties and features adequate for extreme environments.

Materials in aircraft engines should provide high temperature endurance properties, corrosion resistance, and high strength-to-weight ratio, resulting in efficient fuel consumption and longer operational life. Figure 1.2 shows the percentage by weight of each material used in a typical aviation engine. Nickel-based alloys can be used at a higher fraction of their melting temperature than any other materials [1]. Consequently, it has been reported that the use of nickel-based alloys has been significantly increased over time [3].

Table 1.1 Some applications of superalloys [1]

Application	Part
Aircraft/industrial gas turbine components:	Disks, bolts, shafts, cases, blades, vanes, combustors, afterburners
Steam turbine power plant components:	Bolts, blades, stack-gas re-heaters
Automotive components:	Turbochargers, exhaust valves
Medical components:	Dentistry, prosthetic devices
Space vehicle components:	Aerodynamically heated skins, rocket-engine parts
Heat treating equipment:	Trays, fixtures, conveyor belts
Nuclear power systems:	Control-rod drive mechanisms, valve stems, springs, ducting
Chemical and petrochemical industries:	Bolts, valves, reaction vessels, piping, pumps

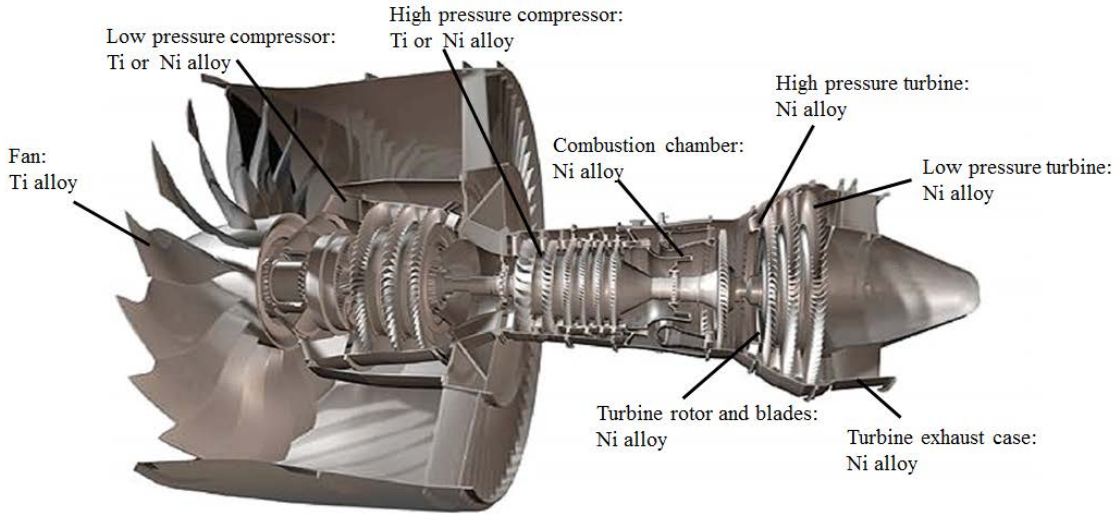

Figure 1.1 Aircraft engine modules (courtesy of Pratt and Whitney)

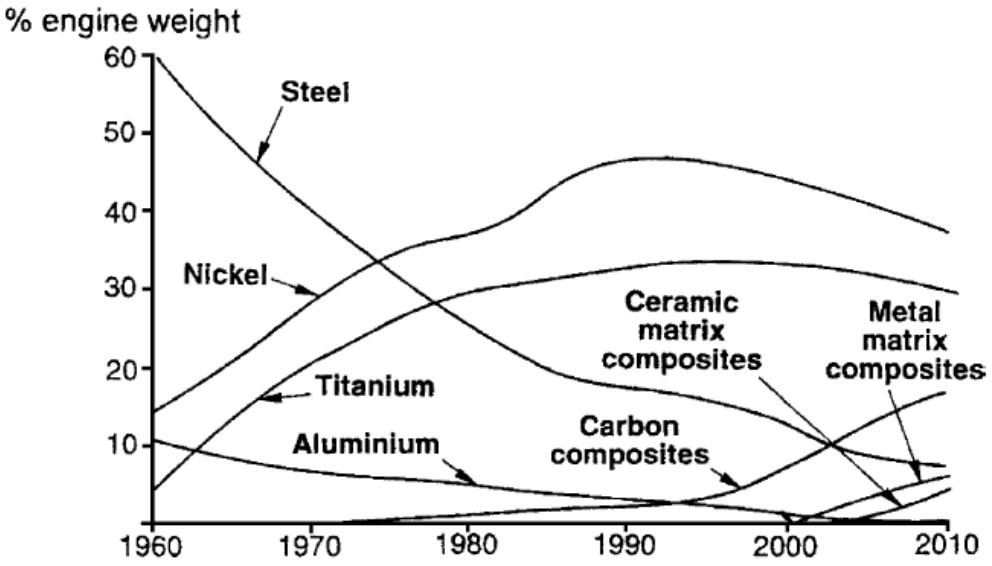

Figure 1.2 Evolution of materials use in aircraft engines [3]

One of these nickel-based alloys, Inconel 718, is widely used in the aerospace industries. The material has been analyzed extensively and its material behavior is known well. Its material components are indicated in Table 1.2. The microstructure of Inconel 718 is comprised of an austenitic face centered cubic (FCC) matrix phase, which is a solid solution of Fe, Cr, and Mo in nickel, together with other secondary phases [4]. The principal characteristics of nickel as an alloy-base are high phase stability of the FCC nickel matrix and outstanding strength retention up to 0.7 T_m (melting point) [5]. These characteristics encourage use of Inconel 718 in a number of applications subjected to high temperatures [6].

Table 1.2 Material composition of Inconel 718 [4]

Element	Content Wt.%
Ni	53.58
Cr	17.52
Mo	2.87
(NB+Ta)	5.19
Ti	0.95
Al	0.57
Co	0.39
C	0.034
S	0.002
Mn	0.12
Si	0.07
B	0.004
Cu	0.05
P	0.006
Fe	Bal.

In manufacturing aircraft engines, major methods of machining Inconel 718 include drilling, broaching, milling, and turning. In this research, we focus primarily on the turning process. The turning of Inconel 718 generates more heat in the cutting zone and higher tool wear for a given cutting condition than that of most other materials. Moreover, the machining of Inconel 718 requires a larger cutting force, which increases concern for tool strength.

Carbide, cubic boron nitride (CBN), ceramic, and HSS tools are commonly used in turning Inconel 718. Among these tools, carbide inserts can be used for the roughing and finishing, but HSS tools are preferred to carbide tools because of their better shock resistance. CBN tools are also used for machining of Inconel 718, but more commonly used in turning the harder nickel-based alloys including cobalt-base cast alloys. Ceramic tools are generally used for the roughing. Although the relatively low fracture toughness of ceramics easily produces notching of the tools, these tools have been improved such that they are now capable of meeting tooling requirements for higher cutting speed [7].

Appropriate cutting speeds depend on material, and Figure 1.3 shows results of studies defining the proper cutting speeds for various types of material [8]. Conventional machining has evolved into high speed cutting (HSC) because of its high performance [9]. HSC has demonstrated superior advantages, such as increased productivity and capability of generating high quality surfaces, burr-free edges, and virtually stress-free components after machining. HSC is widely used in aerospace and automotive industries, but researchers have not yet determined the optimal machining conditions in HSC of nickel-based alloys such as Inconel 718.

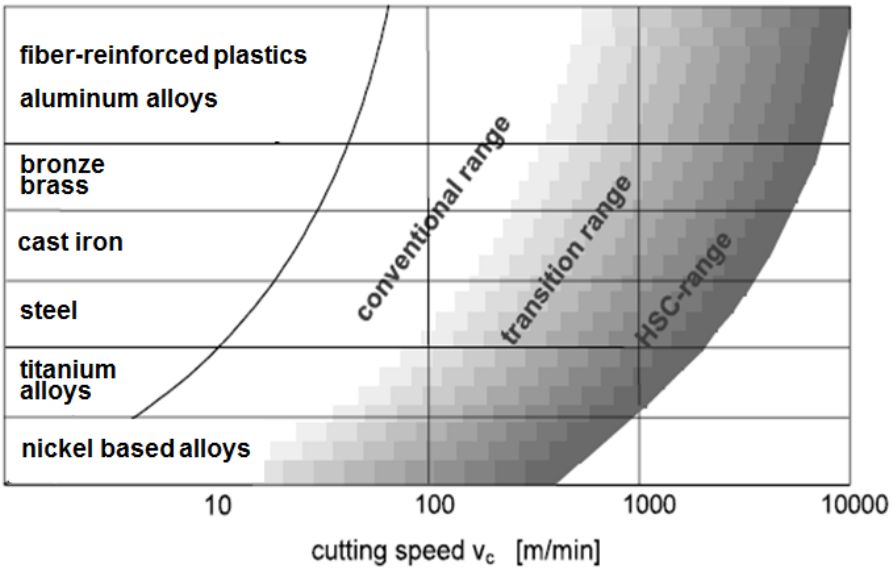

Figure 1.3 Recommended cutting speeds for different materials [8]

Machining conditions are directly connected to the surface integrity of the final product. Surface integrity is a measure of the quality of a machined surface that describes the actual structure of both surface and subsurface. Severe failures produced by fatigue, creep and stress corrosion cracking start at the surface of components. Therefore, in machining any component, it is necessary to satisfy the surface integrity requirements.

Several features are used to determine the surface integrity, such as residual stress distributions, micro hardness, micro crack, surface roughness, and metallurgical structure, as shown in Figure 1.4. There have been a number of studies of the effects of operation parameters on residual stress and surface roughness [10, 11]. These studies have focused on external features or internal features themselves. However, only limited research has been done on the effect of external features on internal features [12, 13].

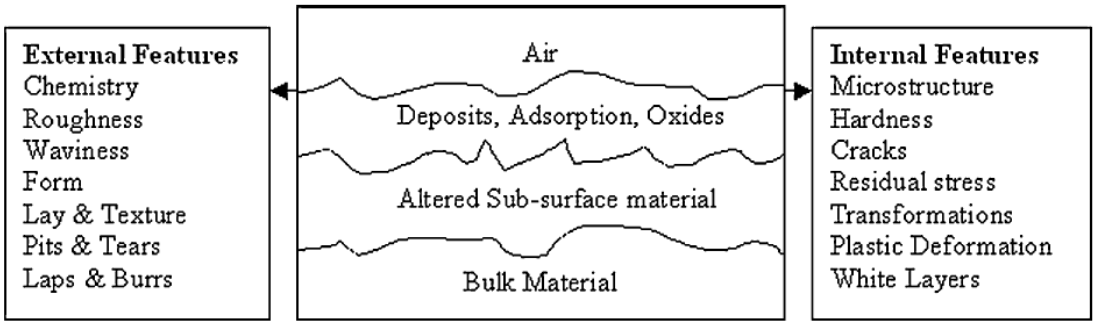

Figure 1.4 Schematic section through a machined surface [14]

Among those aspects of surface integrity, primary surface defects in micro dimensions, such as metal debris, smeared material, carbide cracking, and tearing on the surface, as depicted in Figures 1.5 - 1.8, have recently been reported. These defects are important to consider with regard to Inconel 718, because this material is prone to such surface defects, which cause detrimental effects on the fatigue life of the machined part [15, 16]. These surface defects were observed by several researchers in turning of Inconel 718 [10, 11, 17-19].

Among several surface defects, this study focuses on the rebonding of chips in the machining of Inconel 718. Terms such as chip re-deposition, smeared material, and material build-up have also been used to describe the phenomenon in which some part of a chip is rebonded to the machined surface after being dragged back to the cutting zone [11, 18]. In this research, the phenomenon is referred to as “chip rebonding.”

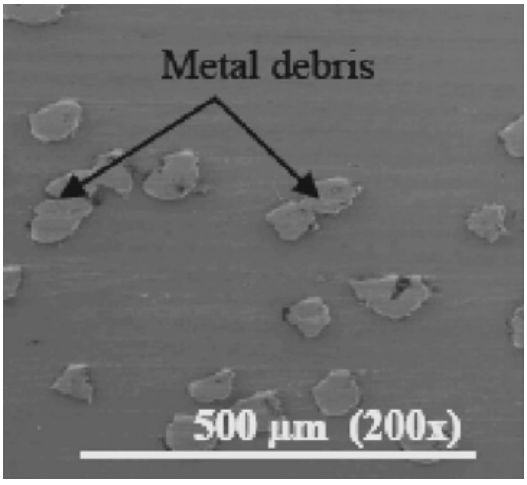

Figure 1.5 Metal debris on the machined surface after cutting Inconel 718 [11]

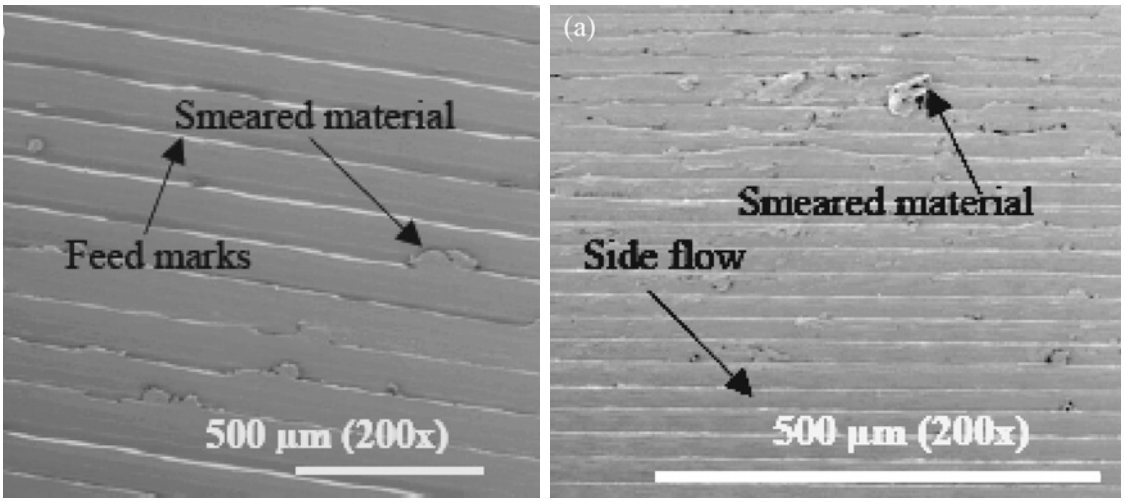

Figure 1.6 Smeared material after turning of Inconel 718 [11]

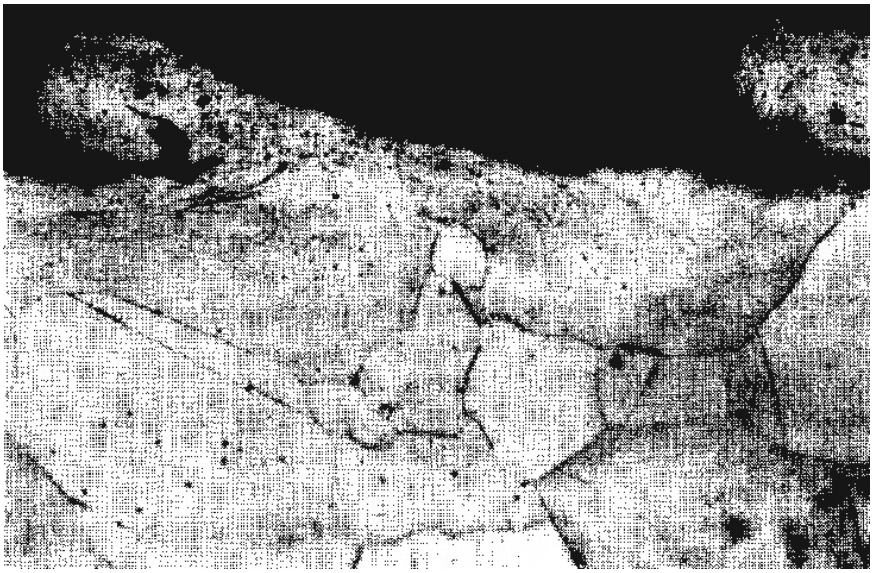

Figure 1.7 Tearing on the machined surface after cutting Inconel 718 (500×) [17]

Figure 1.8 Carbide cracking after turning Inconel 718 (250×) [19]

1.2 Research Motivation

Failure of an aircraft structural part can be catastrophic and may result in loss of millions of dollars and many lives. In general, failures occur when a component or structure is no longer able to withstand the stresses imposed on it during operation. Commonly, failures are associated with stress concentrations which can occur for the following reasons, including [20]:

- Design errors, e.g., the presence of holes and notches, and tight fillet radii,
- Voids and inclusions in the microstructure of the material,
- Local stress concentration generated by corrosive attack of the material, and
- Anomalies such as a scratch, a chip re-bonded material and a micro crack during manufacturing process.

Fatigue is a process whereby cracking occurs under the influence of repeated or cyclic stresses, which are normally substantially below the nominal yield strength of the material. Components that fail by fatigue usually undergo three separate stages of crack growth, which are described as follows:

1) Initiation of a fatigue crack,
2) Propagation of the fatigue crack, and
3) Final sudden failure.

Although fatigue behavior of most metals and alloys is well understood, fatigue cracking remains the most common cause of structural failure in aircrafts. Materials and their design can be taken into consideration so that the probability of fatigue cracks occurring can be reduced. Therefore, many aircraft structural components are designed with a safe or inspection-free life, below which fatigue cracking is improbable. Table 1.3 shows a summary of the common fatigue crack initiation sites that have led to accidents in aircrafts [21]. Material surface defects such as scratch, fretting, chip rebonding can increase the local stress, producing a concentration at these points that could initiate fatigue much quicker than expected.

Table 1.3 Summary of fatigue initiation sites observed in fixed wing aircraft [21]

Initiation Site	Number of Accidents	%
Bolt, stud or screw	108	24
Fastener hole or other hole	72	16
Weld	57	13
Corrosion	53	12
Thread	43	10
Manufacturing defect or tool mark	32	7
Scratch, nick or dent	27	6
Fretting	26	6
Surface or subsurface flaw	13	3
Improper heat treatment	6	1.3
Maintenance-induced crack	4	0.9
Work-hardened area	2	0.4
Wear	2	0.4

Therefore, this research focuses on manufacturing induced anomalies for turbine disk failures in aircraft engines. Rotor disk failure in aero-gas turbine-engines is critical and must be avoided at all costs. The failure of machined mechanical components in service often occurs by fatigue, creep and stress corrosion through the initiation of cracks because of degradation of the surface region [22]. The precise details of the failure process are heavily dependent on the mechanical, physical and chemical state of the surface region that is controlled by the machining and environmental conditions employed in production [16]. In Figure 1.9, chip rebonding can be seen to reduce the fatigue strength below that of the base specimens. In some cases, fatigue crack initiation started from chip rebonding shown in Figure 1.10.

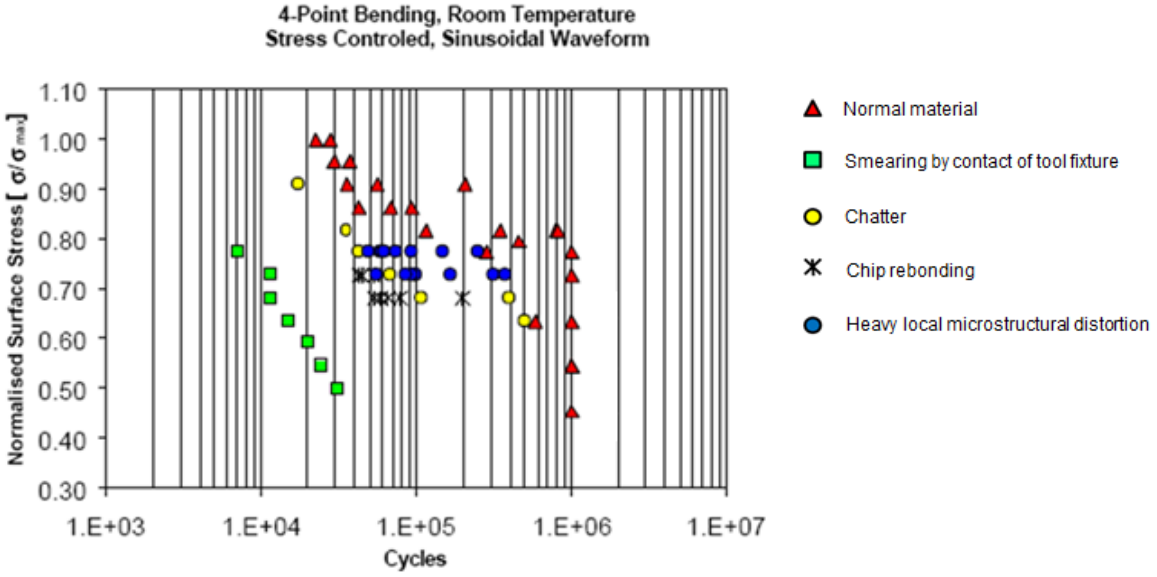

Figure 1.9 Low cycle fatigue results from turned specimen [16]

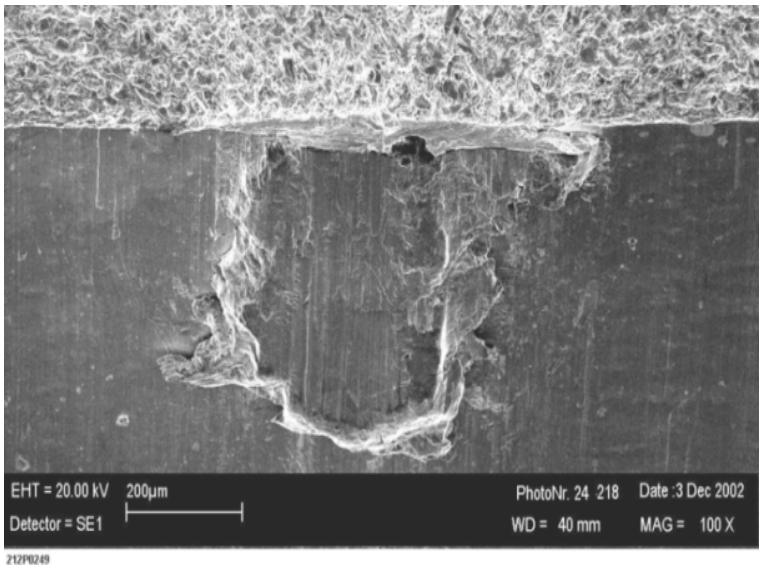

Figure 1.10 Fatigue crack initiation site associated with chip rebonding (100×) [16]

It has been recognized that design engineers should have information about the surface region characteristics of components in addition to those mechanical and physical properties that are generally considered essential. It is important to know the extent to which alterations in surface region characteristics degrade mechanical and physical properties. If surface region degradation occurs, then remedial machining procedures must be developed.

1.3 Research Objectives

The objectives of this research are to investigate the mechanism of anomalies such as chip rebonding on surface after a machining process, to investigate the effect of chip rebonding on subsurface residual stresess, and to find optimal cutting conditions for

achieving a high surface quality in machining of Inconel 718. These objectives are pursued through the following three directions:

1. Observation of chip rebonding on the machined surface, and experimental investigation of the root causes of chip rebonding: to determine the mechanism of chip rebonding occurrence;

2. Analysis of the effect of chip rebonding on subsurface residual stresses by combining a numerical simulation with an analytical calculation, and measurements of residual stresses on the machined surface with chip rebonding; and

3. Investigation of the effect of cutting parameters on chip rebonding to minimize and/or eliminate the chip rebonding phenomenon on the machined workpiece, and the evaluation of the effect of metal working fluid on chip rebonding occurrence.

1.4 Dissertation Outline

This dissertation contains five chapters.

Chapter 1 introduces the background of this research, and presents the motivation and objectives of this research.

Chapter 2 investigates how chip rebonding occurs during the face turning of Inconel 718 with a round tool insert. First, we observe samples with chip rebonding and perform a metallographic analysis. To explain the mechanism of chip rebonding occurrence, we hypothesize that this chip rebonding formation is mainly due to torn chips at the side edge

of the main chip. In order to confirm this hypothesis, a chip curl-blocking device is designed. Using all these observations of chip rebonding and tests with the chip curl-blocking device, we are able to explain the mechanism of chip rebonding occurrence.

In Chapter 3, we investigate the effect of chip rebonding on residual stresses. When partial chips stick to the machined surface, the partial chips with higher temperature produce residual stresses. Because they stick to the workpiece with higher thermal expansion, they cause the change of residual stress distribution as they cool down. To evaluate the chip rebonding effect on residual stresses, first we need to calculate the temperature of chip rebonding. To do it, we develop an analytical model that predicts heat flux at the chip rebonding. Then, the calculated heat flux of chip is applied to a finite element model to predict the temperature of chip rebonding. To calculate the residual stresses after machining from the previous path, we develop a FE model for orthogonal machining. By using the predicted residual stresses on a machined surface, we create another FE model to simulate the chip rebonding phenomenon and investigate the effect of chip rebonding on residual stresses according to cutting parameters. We verify the models with experimental results.

In Chapter 4, we identify the key variables that influence the occurrence of chip rebonding to prevent chip rebonding. We perform a parametric study in dry and wet cutting conditions. Under conventional cutting conditions in dry cutting, the feed rate has the strongest effect on chip flow direction and chip characteristics. The chip morphology at the chip's side edge is relevant to chip rebonding occurrence. To investigate the effect of metal working fluid (MWF) on chip rebonding, different concentrations of MWF are examined.

We find that the size of the torn chips at the chip's side edge decreases as the viscosity of MWF increases. A particular range of sizes of torn chips leads to chip rebonding between a tool and workpiece depending on the viscosity of MWF. By increasing viscosity, MWF produces small sizes of torn chips at the chip's side edge and thus we can prevent chip rebonding.

Chapter 5 summarizes the research work and the contributions that have been accomplished, and provides future direction in research.

CHAPTER 2 CHIP REBONDING MECHANISM IN TURNING INCONEL 718

2.1 Introduction

It has been known that Inconel 718 is a difficult material to machine, because its low thermal conductivity produces high cutting temperatures in the cutting zone. Temperatures rise from around 900°C at a low cutting speed of 30 m/min up to 1300°C at a high cutting speed of 300 m/min [23, 24]. At high temperatures, Inconel 718 chemically interacts with various tool materials to form an adhering layer that leads to tool wear [25, 26]. All of these characteristics of Inconel 718 make it difficult to machine [2, 7, 27-29].

Recently a number of studies have been done on machining nickel-based alloys with ceramic tools [30, 31]. Due to high material hardness at high temperatures, chemical stability, and wear resistance, ceramic tools demonstrated good results when machining nickel-based alloys [30]. To machine at cutting speed over 100 m/min, ceramic tools are usually used and they have been improved such that they are capable of meeting tooling requirements up to the cutting speed of 300 m/min [7]. However, the high temperatures and stresses with increased cutting speed in the cutting zone can produce microstructure changes that could lead to surface defects on the machined surface [17].

Among several surface defects, chip rebonding has been found on the machined surface after turning Inconel 718 as shown in Figure 2.1. To decrease the risk of failures due to

chip rebonding in aero-gas turbine engines, regions with chip rebonding have to be polished manually. This extra work increases labor costs and manufacturing times. In order to avoid them, cutting parameters are usually chosen based on an expert's experience or the manufacturer's handbook. However, these methods do not assure that cutting conditions are optimized to eliminate chip rebonding. Thus, we need to investigate how chip rebonding occurs to find optimal cutting parameters and do this without increasing manufacturing cost of products.

Although many publications about surface integrity have been released, this chip rebonding is little understood. Therefore, the following experimental work and observations reveal the mechanism of chip rebonding when turning Inconel 718 with round ceramic tools. The experimental setup and design are first introduced in Section 2.2, and results are presented afterwards.

(a) (b)

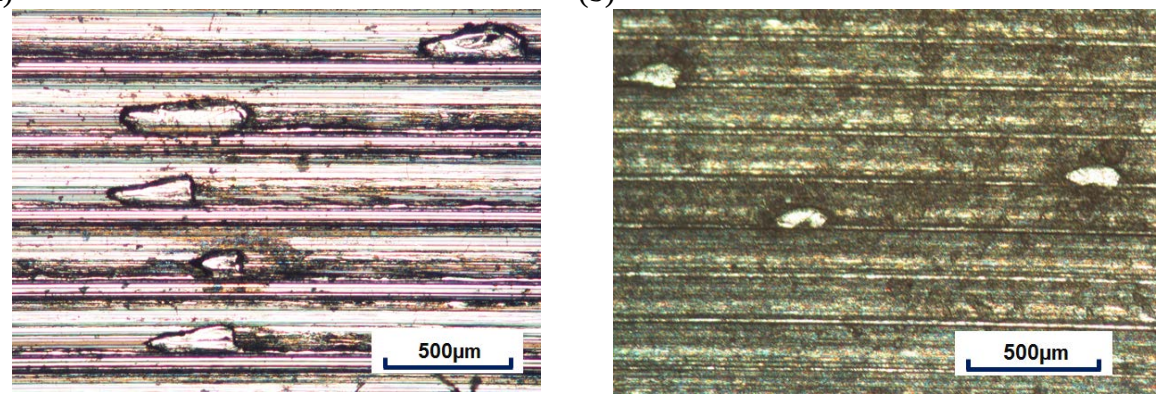

Figure 2.1 Chip rebonding (40×) (a) cutting conditions: v = 300 m/min, f = 0.3 mm/rev, d = 0.127 mm (b) cutting conditions: v = 150 m/min, f = 0.18 mm/rev, d = 0.05 mm

2.2 Experiment and Measurement to Assess Chip Rebonding

The experiments as shown in Table 2.1 were undertaken to reproduce chip rebonding in face turning of Inconel 718 with ceramic tools. Inconel 718 is used as the workpiece material and a whisker-reinforced ceramic round insert is used as the tool insert for each test. In Figure 2.2, a round insert is used for a face-finish turning in order to decrease the risk of tool breakage, and the tool holder has a rake angle and side rake angle of -5°.

Table 2.1 Experimental setup

Material	Inconel 718 with dimensions 150 mm OD, 40 mm ID, 200 mm thickness
Cutting tools	Whisker-reinforced ceramic (Si_3N_4 , WG-300)
Tool Holder	KENNAMETAL (MRGNLC-164D)
Dynamometer	KISTLER 9257A
Cutting speed	240 m/min
Feed rate	0.3 mm/rev
Depth of cut	0.127 mm
Metal working fluid	CIMTECH 310

(a)

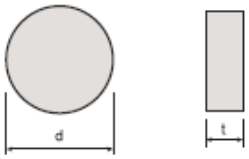

(d: 12.7 mm, t: 4.75 mm)

(b)

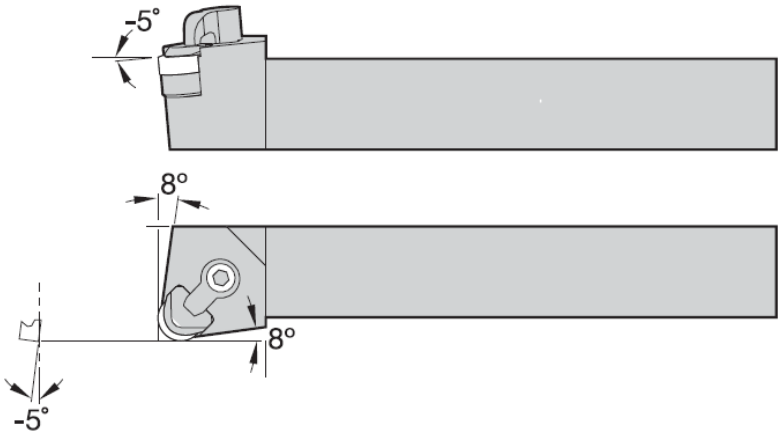

Figure 2.2 Tool geometry (a) tool insert (b) tool holder

Figure 2.3 (a) shows the overall finish turning process and the setup of a workpiece, tool holder and dynamometer. In Figure 2.3 (b) the workpiece rotates clockwise and the tool insert moves inwards. A WYKO2000 is used to produce a 2D and 3D profile of a machined surface. Figure 2.4 (a) shows one example of a chip rebonding measurement. Figure 2.4 (b) shows the overall surface with chip rebonding.

(a)

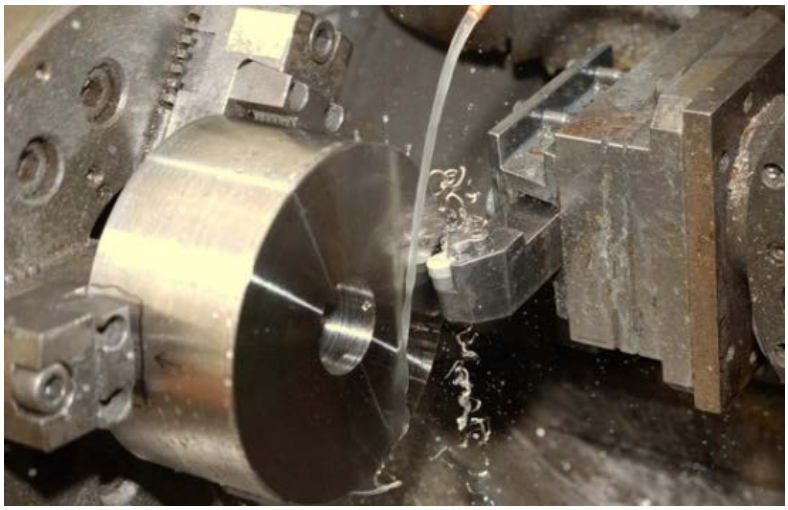

(b)

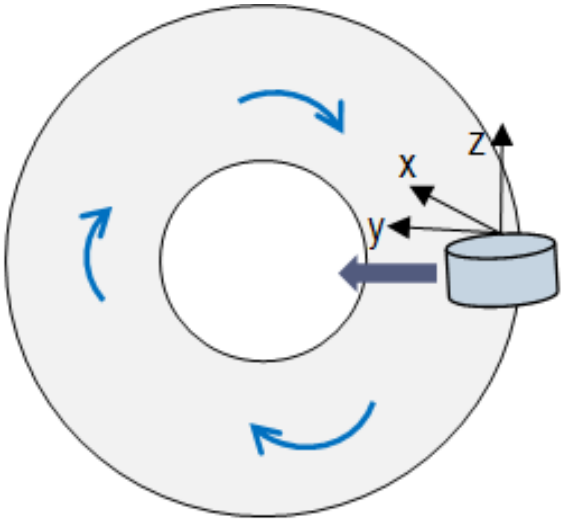

Figure 2.3 Turning experimental setup (a) cutting process (b) schematic diagram

(a)

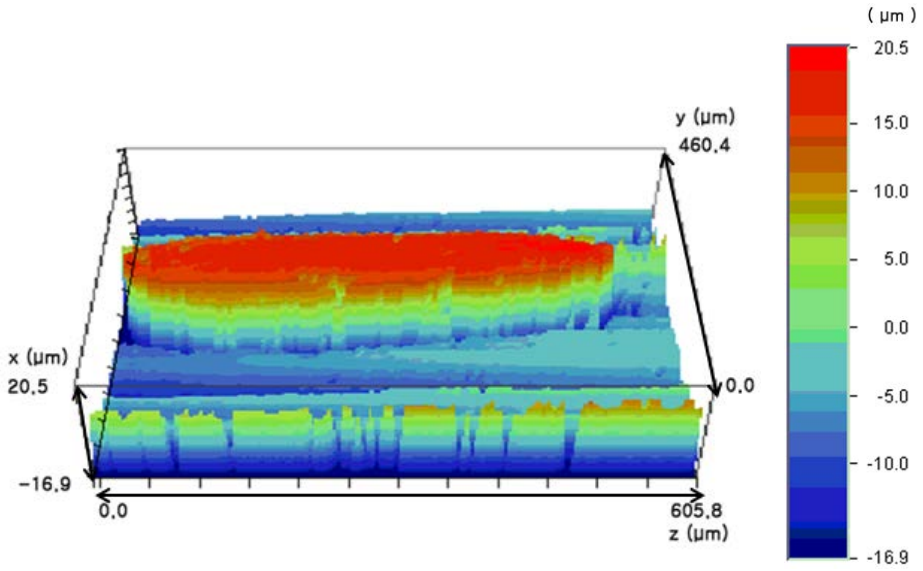

(b)

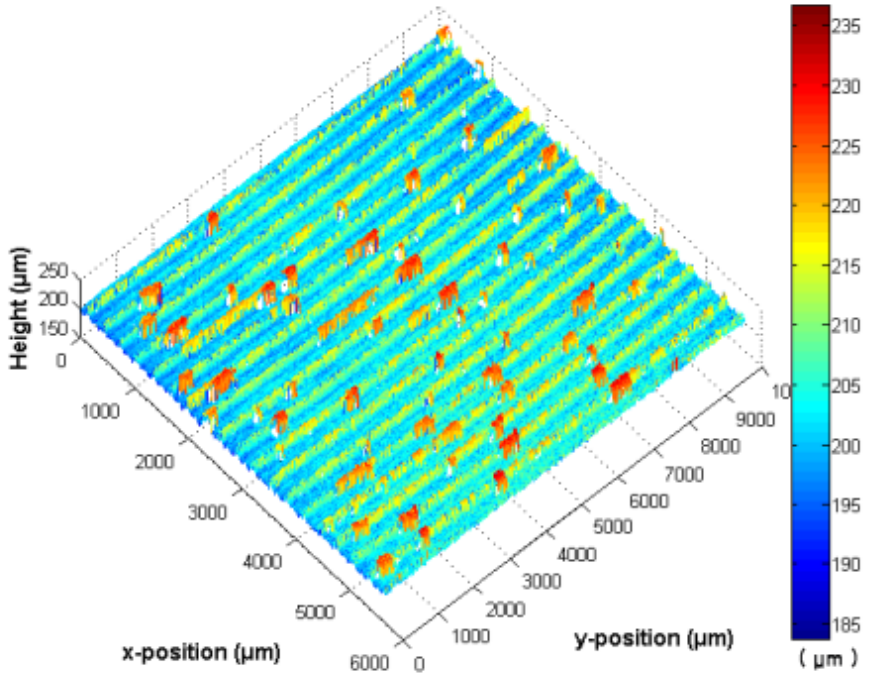

Figure 2.4 Surface measurement (a) measurement of one chip rebonding sample (b) measurement of overall surface with chip rebonding

During the experiment, cutting forces are measured using a KISTLER 9257A as shown in Figure 2.3 (a). After cutting, the roughness of the workpiece is measured with the WYKO2000, shown in Figure 2.4. After each test is completed, the workpiece surface undergoes a cleanup pass with an alternate tool.

2.2.1 Observation of Chip Rebonding Sample

In this section, we observe chip rebonding samples to understand the mechanism of chip rebonding occurrence. First, the cross sections of chip rebonding is observed, and then metallographic analysis is performed to see whether chip rebonding phenomenon is related to a chemical reaction between chip rebonding and a ceramic tool. Overall machined surface with chip rebonding, and chip morphology are observed to find any relevance for chip rebonding occurrence between them.

After finish machining of Inconel 718 using the cutting conditions given in Table 2.1, the chip rebonding on the machined surface is observed as shown in Figure 2.5 (a). A $5\times5\times5mm^3$ specimen containing chip rebonding is cut from the workpiece material along a feed line and perpendicular to a feed line for observation as shown in Figures 2.5 (c) – (f). The sample is prepared using wire EDM and subsequent grinding and polishing steps, which use a regime of progressively finer grit diamond papers and pastes. It should be noted that the sample is polished so that the cross section of chip rebonding could be observed.

Figure 2.5 (a) shows overall chip rebonding on the machined surface, and Figure 2.5 (b) shows a top view of one chip rebonding sample. In Figure 2.5 (b), the left side of the chip,

which has a straight edge, is seen to be rebonded along the feed mark. In the top view, one cannot recognize whether the deposited material comes from the workpiece or the smeared chip. Using a microscope and SEM, the cross-section views of chip rebonding area are captured, as shown in Figures 2.5 (c) – (f). During machining, an insert moves from right to left while it smears the chip to the machined surface with a uniform thickness as shown in Figure 2.5 (c). Figure 2.5 (d) shows the cross section of chip rebonding perpendicular to the feed line. Figures 2.5 (e) and (f) are a magnification of the left and the right ends of Figure 2.5 (c), which are stuck to the workpiece, and Figures 2.5 (e) and (f) show a gap at both ends between base material and re-bonded material. The presence of this gap implies that chip rebonding is not generated from the workpiece and that part of a chip has been smeared onto the workpiece. We further observe that rebonded chips have uniform thickness, around 30 μm, and have severe plastic deformation, seen in the shear flow lines in Figures 2.5 (e) and (f).

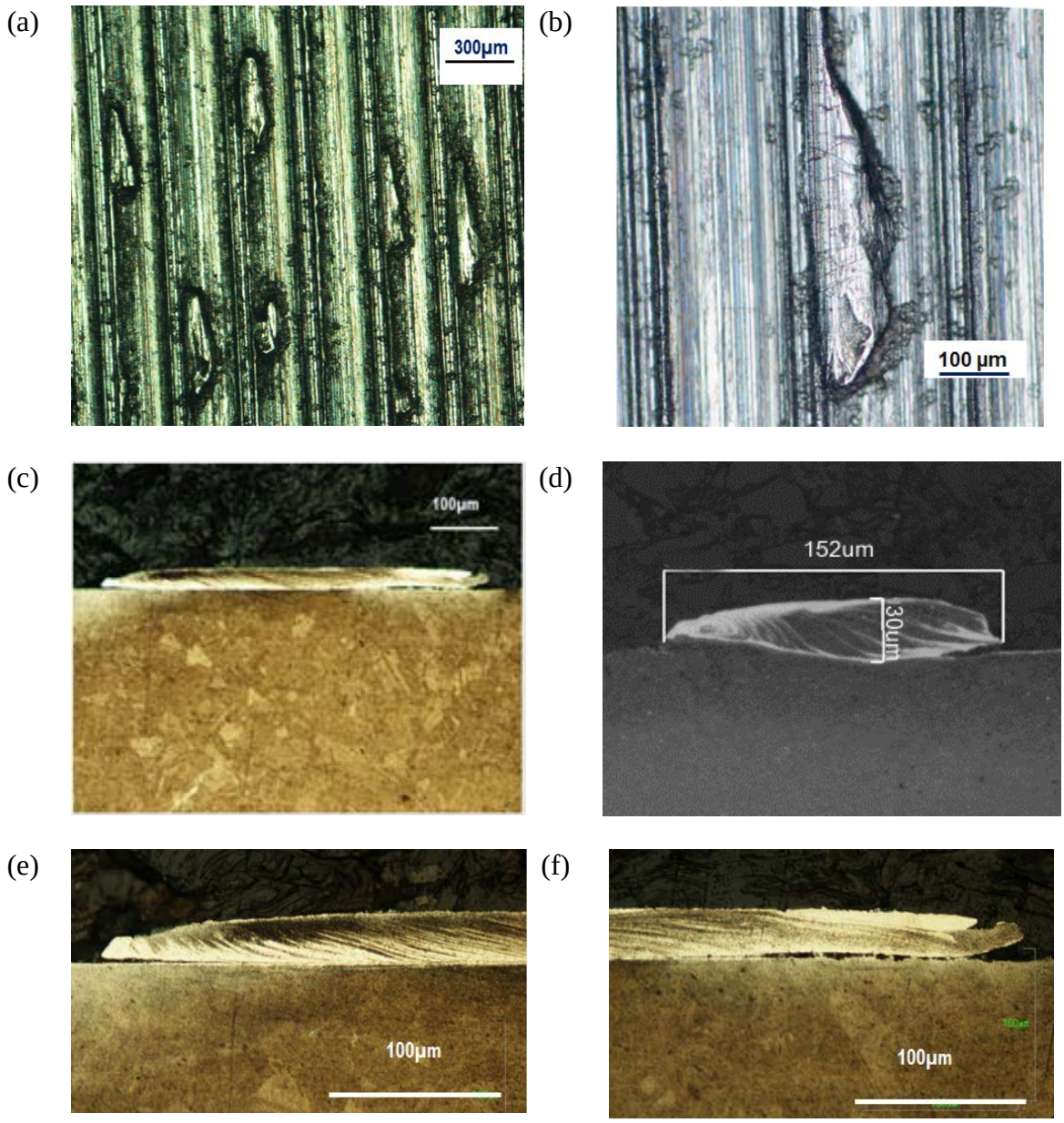

Figure 2.5 Machined surface with chip rebonding (a) overall surface (40×) (b) optical top-down view (100×) (c) optical cross-section view (100×) along feed line (d) SEM cross-section view perpendicular to feed line (250×) (e) magnified left cross section of Figure 2.5 (c) (250×) (f) magnified right cross section of Figure 2.5 (c) (250×)

In order to check whether a potential chemical/diffusive reaction between a ceramic tool and a workpiece are the cause for chip rebonding, the chemical compositions of the

base material with chip rebonding were analyzed. Composition analysis was performed on a 10µm×10µm sample in chip rebonding (Area 1) and base material (Area 2). The EDAX software's Spot Spectrum Collection feature was used to determine semi-quantitative percentages of each elemental constituent at a chosen spot on the material. Characteristic peaks for Area 1 and Area 2 illustrated the similar presence of individual elements as shown in Figure 2.6, and chemical compositions between Area 1 and Area 2 were almost the same as shown in Table 2.2. From this analysis, it can be concluded that there were no chemical reactions between the workpiece material and the ceramic tool. Thus, the bonding mechanism between the rebonded chip and the workpiece is determined to be mechanically driven.

(a)

(b)

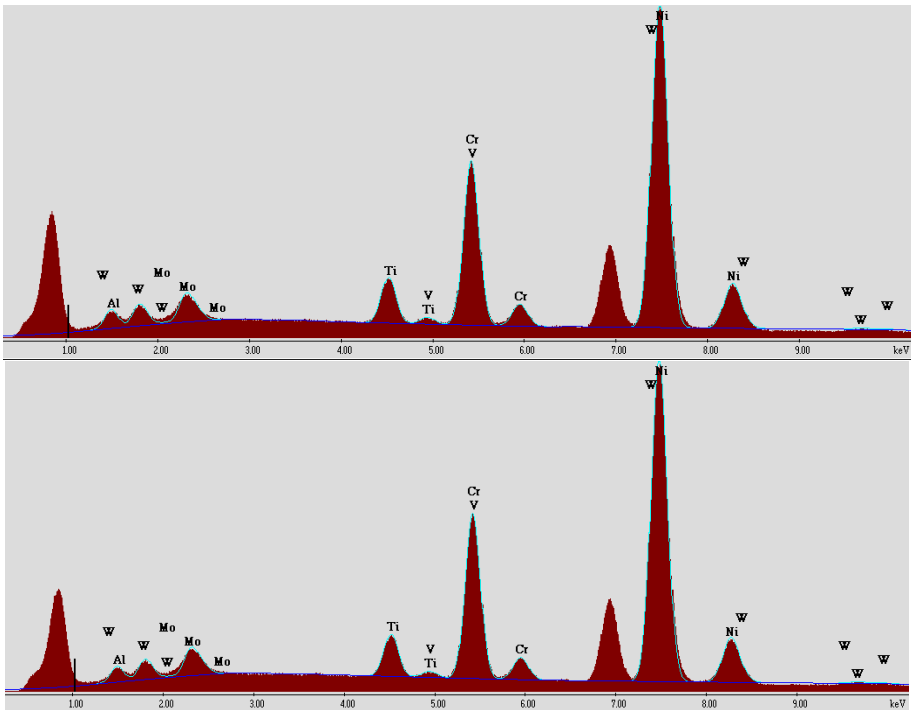

Figure 2.6 Spot analysis using EDAX (a) Area 1: chip rebonding material (b) Area 2: base material

Table 2.2 Chemical compositions of Area 1 and Area 2 in weight percent

	Ni	Cr	Mo	Ti	Al	W	V
Area 1	59.96	19.46	5.04	5.16	9.51	0.8	0.07
Area 2	59.91	19.5	5.11	5.12	9.4	1.3	0.06

2.2.2 Observation of Overall Machined Surface and Chip

In Figure 2.7, the overall machined surface is observed in order to analyze the chip-rebonding-occurrence pattern. The arrows in Figure 2.7 represent feed marks in a turning operation. The tool insert moves from right to left in every rotation of workpiece and the workpiece rotates clockwise. In this figure, the workpiece moves downwards.

In Figure 2.7, we observed a figure of chip rebonding and found common features on the overall machined surface that the left side of the rebonded chips is straight, aligned to the feed marks.

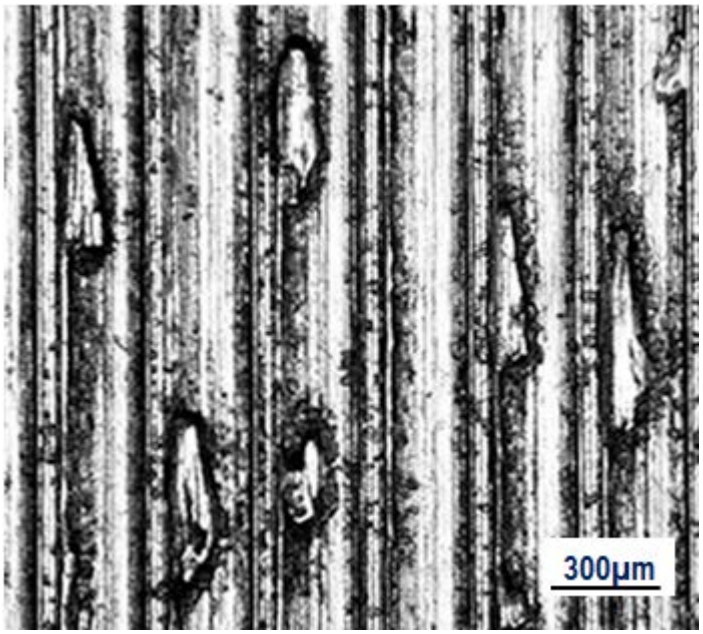

Figure 2.7 Overall machined surface with chip rebonding (40×)

Different morphology of chip rebonding in Figure 2.7 can be explained from Figure 2.8. A few chip rebondings are separated while they are formed. Figure 2.8 (a) shows the case of separated chips; Figure 2.8 (b) is magnified to compare the shapes of fractured parts. Another example in Figures 2.8 (c) and (d) also confirms that two parts in Figure 2.8 (d) are originally one body until the tool insert strikes and separates them.

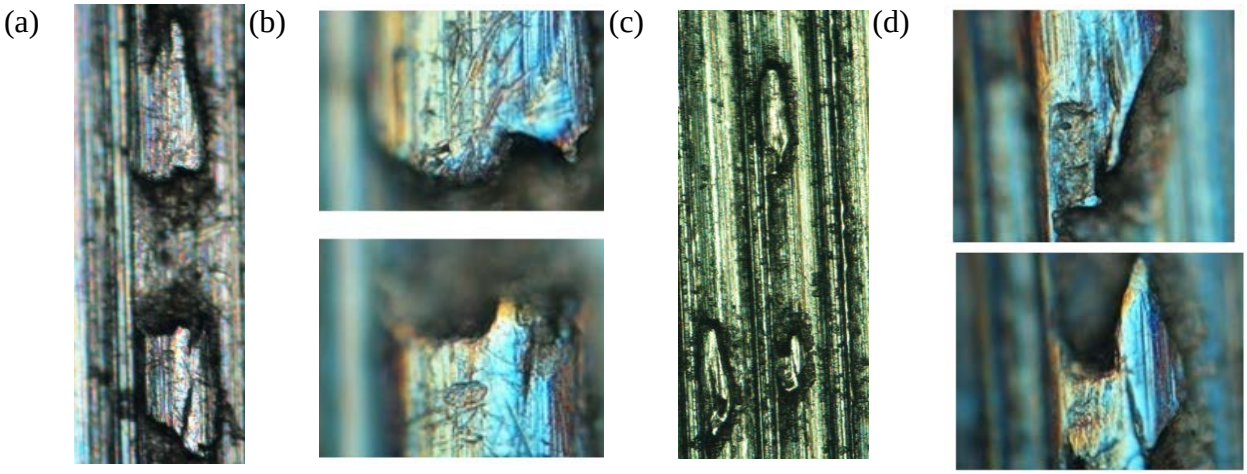

Figure 2.8 Examples of separated chip rebonding , (a) and (c): 40×, (b) and (d): 250×

In Figure 2.9 (a), the WYKO2000 produces a 2D profile of the machined surface. The size of the piece is 6 mm by 4.5 mm. To observe the locations of chip rebonding, the figure is converted to gray scale as shown in Figure 2.9 (b). It is observed in Figure 2.9 (b) that the chip rebonding occurs periodically on the surface and for the considered case the period is around 1.3 mm. Figure 2.9 (d) is a magnified version of the edge of the chip in Figure 2.9 (c); the length of the intervals between torn chips at the chip side edge in Figure 2.9 (d) is almost the same as the periodic length of chip rebonding occurrences in Figure 2.9 (b).

From these observations, we can explain that torn chips have a strong relationship with chip rebonding occurrences.

(a)

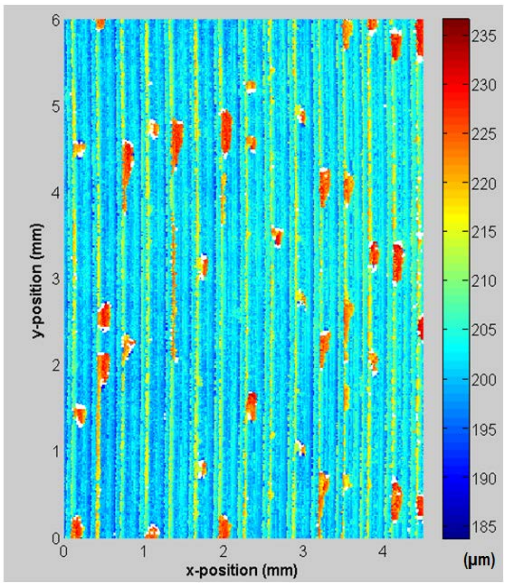

(b)

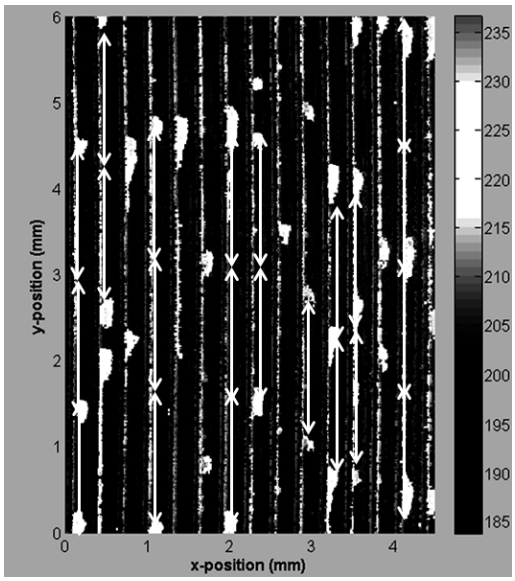

(c)

(d)

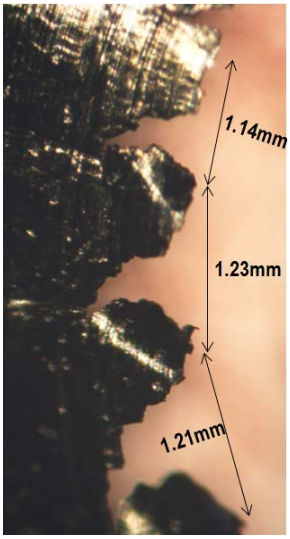

Figure 2.9 Periodic chip rebonding occurrence (a) measured profile of machined surface (b) periodic occurrence of chip rebonding (c) entire chip morphology (40×) (d) torn chips at the side edge of chip (40×)

2.3 Hypothesis on Positions of Chip Rebonding Occurrence

Figure 2.10 describes the face turning process at the given geometric conditions; the workpiece moves in the negative z direction and the tool moves at the feed rate of 0.3 mm/rev in the positive y direction. When chip flows out along the rake face, chip rebonding phenomenon occurs.

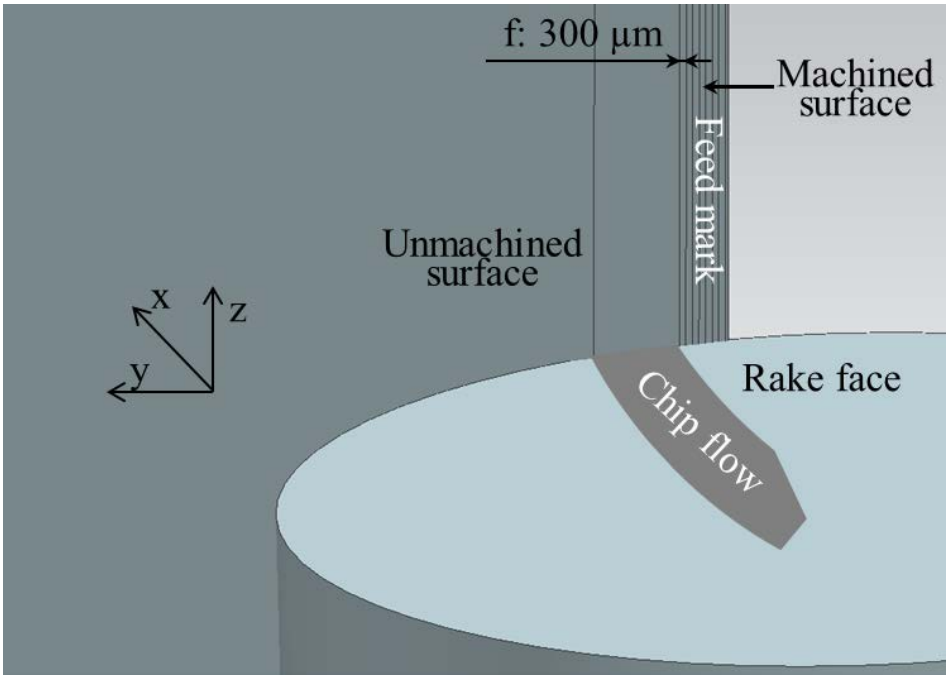

Figure 2.10 Diagram for a face turning process

In Section 2.2.2, we observed that chip rebonding could occur from the torn chips at the side edge of a chip. Another possible occurrence of chip rebonding is under the flank surface of a tool. The built up edge on the cutting edge could be smeared under the flank surface. This phenomenon is known as burnishing. We assume that 'Chip Rebonding 1' occurs from burnishing and 'Chip Rebonding 2' arises from torn chips at the side edge of a

chip in Figure 2.11; a dashed line represents an uncut chip cross section in the x-y plane of Figure 2.11 (a) and a dashed line in Figure 2.11 (b) is cut away while the workpiece rotates.

(a)

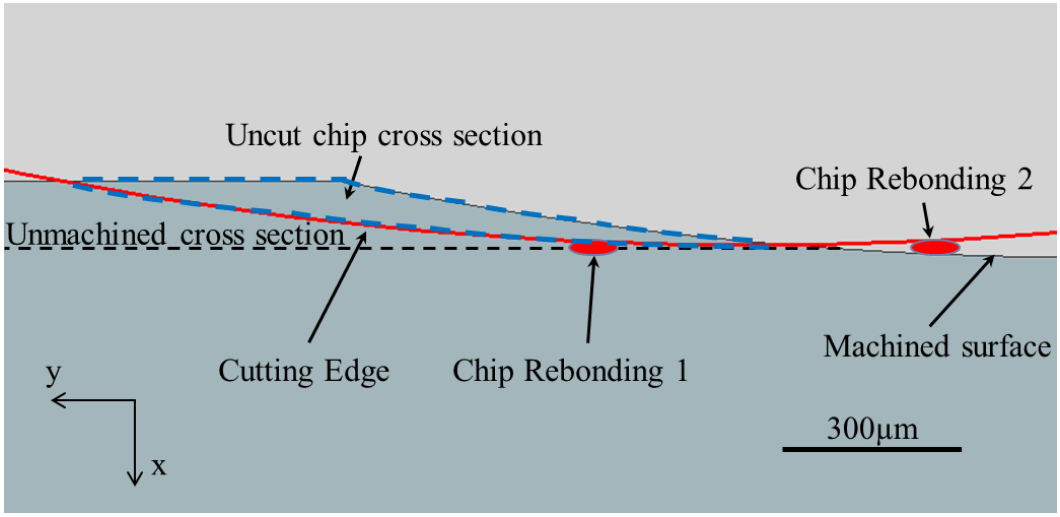

(b)

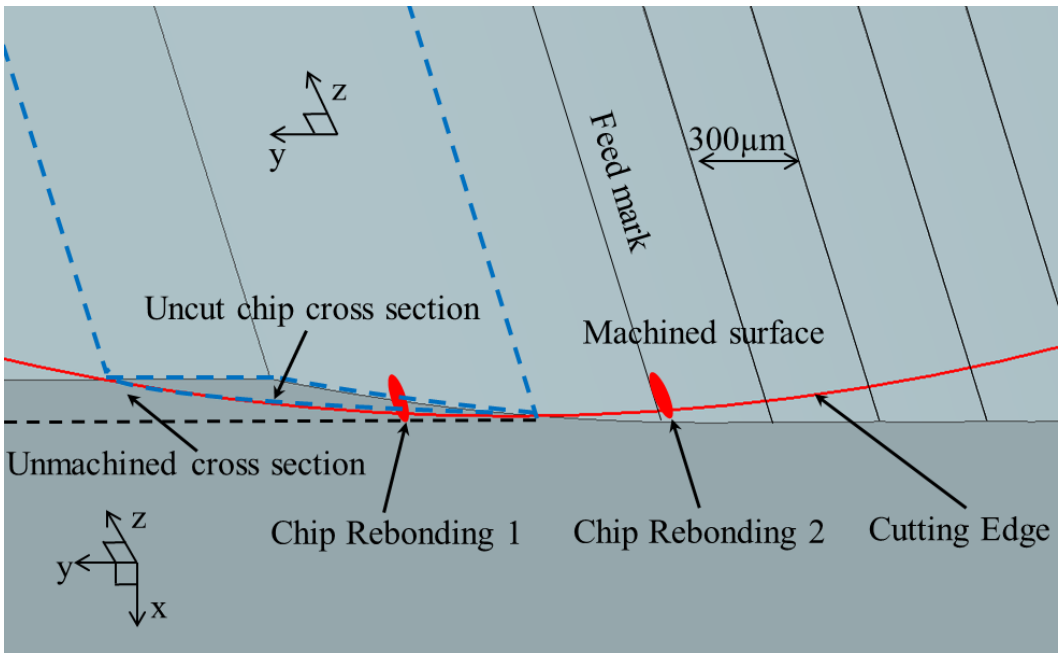

Figure 2.11 Possible chip rebonding positions (a) uncut chip cross section in the x-y plane (b) uncut chip cross section in 3D

2.4 Verification Tests

Next, the test of a chip blocker was performed to verify the hypothesis on the position of chip rebonding occurrence. Because the conventional clamped type chip-breaker in machining of Inconel 718 does not break chip into pieces and affect chip flow direction much, in this experiment a special chip curl blocking device was designed as shown in Figure 2.12. This designed blocker can block the chip flow between the position of 'Chip Rebonding 1' and 'Chip Rebonding 2' in Figure 2.11.

(a) (b)

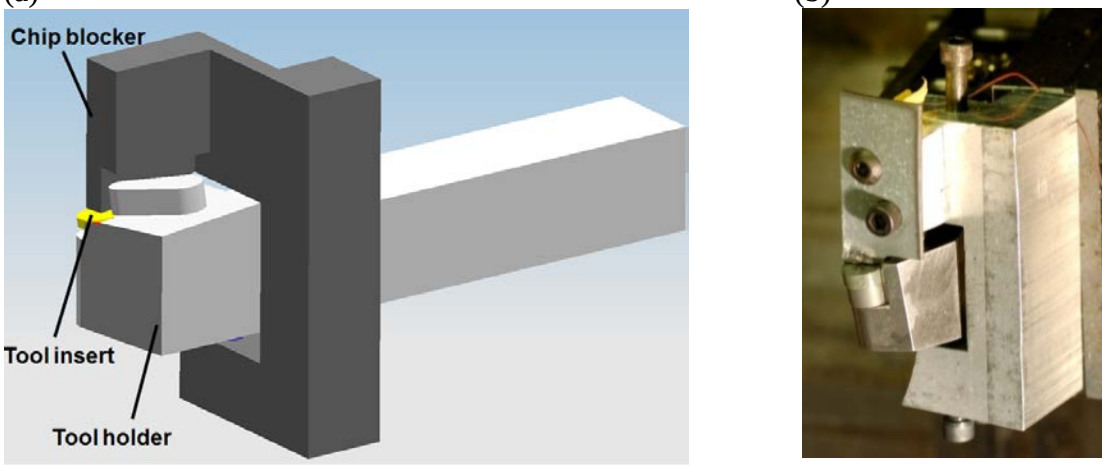

Figure 2.12 Chip blocker (a) CAD design of chip blocker (b) installed chip blocker

When machining at a cutting speed of 240 m/min, a feed-rate of 0.3 mm/rev, and a depth of cut of 0.3 mm, differences in cutting forces can be seen between the tests with and without the chip curl blocking device. As shown in Figure 2.13, the force traces are smoother during the test using the chip blocking device. Fluctuations in the cutting force represent how a chip flow affects cutting force between the tool and workpiece. Tangled chips and torn chips stuck between tool and machined surface might cause the fluctuations.

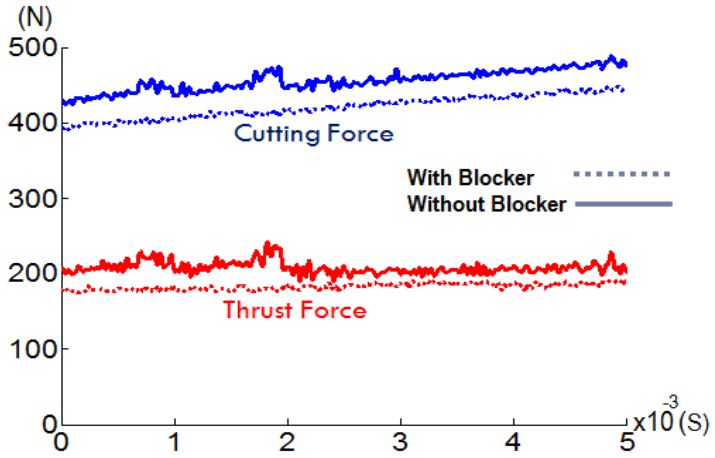

Figure 2.13 Comparison of cutting forces with chip blocker

In Figure 2.14 and Table 2.3, surface roughness descriptors R_a and R_t with the chip blocker are compared with R_a and R_t without the chip blocker. As seen from the results, better surface quality and no chip rebonding are produced when the chip blocker is applied. This result validates the hypothesis of 'Chip Rebonding 2'; that is, the torn chips are curling back toward the workpiece and stuck into the cutting zone to be rebonded.

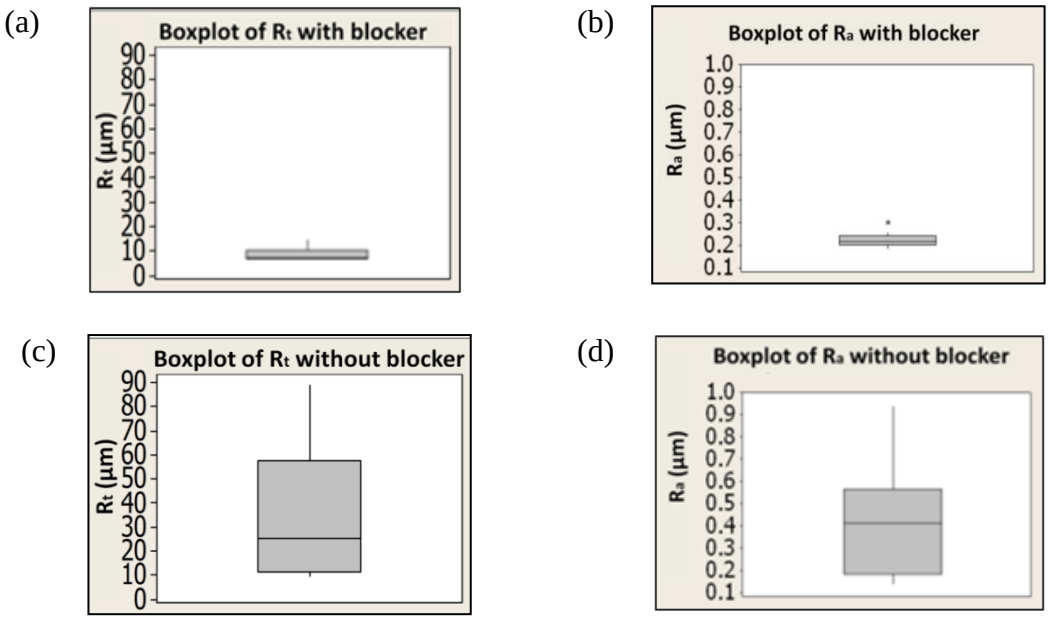

Figure 2.14 Comparison of R_a and R_t (a) R_t with chip blocker (b) R_a with chip blocker (c) R_t without chip blocker (d) R_a without chip blocker

Table 2.3 Comparison of average R_a and R_t in dry cutting

	With blocker	Without blocker
R_a (µm)	0.21	0.54
R_t (µm)	6.32	32.93

The mechanism of chip rebonding is explained on the basis of previous observations and tests. The explanation rests on a description of the moving direction of the tool, workpiece, and chip flow in Figure 2.3 (b): a workpiece rotates clockwise and a tool insert with a rake and side rake angle of -5° as shown in Figure 2.2 (b) moves inward.

Figure 2.15 shows a more specific description of the cutting zone. When chip rebonding happens, Figure 2.15 (a) depicts the moment of an occurrence of chip rebonding. Part of the torn chip goes into the gap between the tool insert and workpiece. Subsequently the tool insert smears it as the workpiece rotates. Figure 2.15 (b) shows the change of position of chip rebonding resulting from the rotation of the workpiece. During the transition, the smeared chip is bonded onto the machined surface. The tool insert cuts out the left part of the smeared chip. Thus, the thickness of the rebonded chip is uniform because of the constant size of the gap between the tool insert and workpiece, and the boundary shape of chip rebonding adjacent to the feed mark is straight.

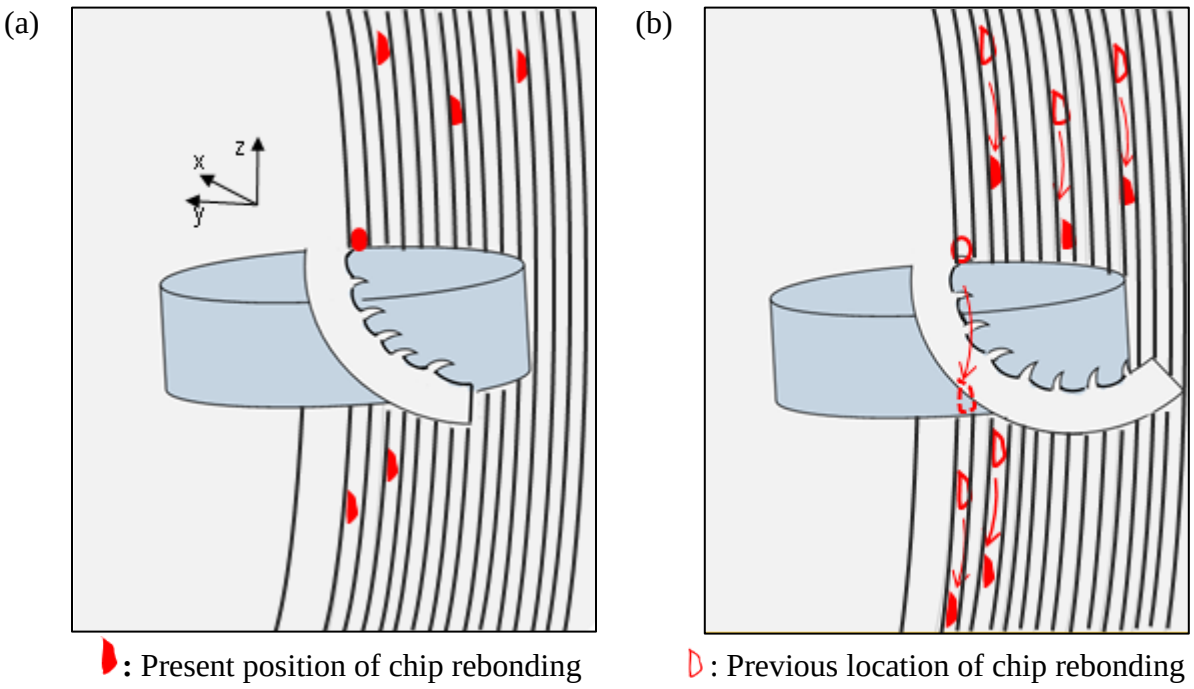

Figure 2.15 Chip rebonding occurrence (a) before chip rebonding occurrence (b) smeared chip rebonding by tool insert during rotation

2.5 Conclusions

This chapter focused on revealing the mechanism of chip rebonding occurrence during the face turning of Inconel 718 by a round ceramic insert.

The formation of chip rebonding in the machining process decreases the service life of the machined component. In order to identify the root causes of chip rebonding, chip rebonding samples were first observed. From the observations, we found that the thickness of rebonded chip is uniform and that the rebonded chip has severe plastic deformation. From the component analysis of the chip rebonding part and workpiece, we could conclude that the chip rebonding part is not caused by a chemical reaction from the ceramic tool. The gap between chip rebonding and a workpiece explains that the chip was separated from the workpiece and then smeared to the workpiece.

Overall observations of the machined surface show that chip rebonding occurs periodically along a feed mark, and that the chip's side edge is periodically torn and curled. From these observations, we could hypothesize that chip rebonding formation is mainly due to the torn chips that are periodically located at the side edge of the chip and smeared by the tool along the workpiece feed mark.

A chip curl blocking device was designed in order to confirm this hypothesis and resulted in no significant chip rebonding. Thus, our hypothesis was confirmed.

CHAPTER 3 THE EFFECT OF CHIP REBONDING PHENONMENON ON RESIDUAL STRESSES

3.1 Overview

In safety related components such as parts of aero engines, the surface quality is critically important [21, 32], since surface defects can initiate fatigue fractures on the machined surfaces [16, 33]. Generally, compressive residual stresses are beneficial to fatigue life, whereas tensile residual stresses decrease fatigue life. After machining, plastic deformation on the machined surface usually results in compressive residual stresses, while additional local heating on the machined surface can cause tensile residual stresses [34].

In Chapter 2, the mechanism of chip rebonding was shown to be the result of smearing of a partial chip on the machined surface. When the chip was smeared, the chip's temperature would be increased. This local heating from the rebonded chip may lead to tensile residual stresses on the subsurface material. Since chip rebonding decreased the life of the workpiece for low cycle fatigue tests [16], these tests also indicate that the chip rebonding phenomenon can be linked to residual stresses.

For the chip rebonding phenomenon to occur, high temperature and pressure are necessary at the interface between chip and base material. Although precise details of rebonding process at the joint are not yet known, evidence suggests that turning process of Inconel 718 involves high temperature and high pressure at the joint; chip temperature can

rise up to 1300ºC at the cutting zone [24] and high pressure can be expected when a tool smears a chip on a machined surface. As shown in Figure 3.1, the machined surface near chip rebonding exhibits oxidation marks that indicate the presence of high temperature.

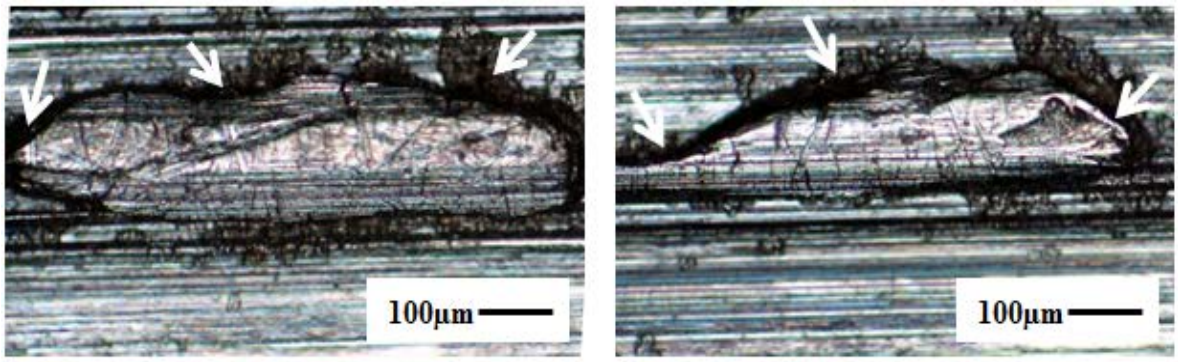

Figure 3.1 Examples of oxidation marks near chip rebonding (250×)

Though residual stresses have been widely studied in recent years, the influence of chip rebonding on residual stresses of Inconel 718 has not been studied. In case of finding chip rebonding after machining of Inconel 718, the factory workers polish the surface manually without any information for the polishing depth.

In this chapter, we focus on evaluating the effect of chip rebonding on residual stresses, specifically after face turning of Inconel 718 with a round ceramic tool. The simulation model of chip rebonding occurrence is developed through finite element method to understand better the process of chip rebonding occurrence and the effects of chip rebonding on residual stress distribution in the workpiece subsurface. Modeling process is first introduced, and residual stress measurements of the workpiece subsurface with chip

rebonding are then presented. Finally, the results of simulation are compared with the experiment measurements.

3.2 Modeling Approach

The modeling of chip rebonding-induced residual stress on the machined surface is divided into three main parts. Figure 3.2 shows a simplified flowchart of the modeling procedure. The first part of this study models the temperature in the chip that will cause chip rebonding. Many experimental techniques such as using an infrared camera [35], thermocouples [36], or tool-foil thermocouples [37] have been used to measure the temperature at the cutting zone. However, the infrared camera cannot be used in wet cutting, it is difficult to achieve good accuracy with the embedded thermo couples, and the tool-foil thermocouple method cannot be used for ceramic tools.

For modeling the temperature in the chip, the cutting forces with given cutter geometry are calculated analytically and then heat fluxes are predicted according to the cutting forces along the chip cross section. The heat fluxes are applied to a finite element (FE) model to predict the temperature distribution along the chip section. From this model, we can predict the temperature of the chip's side edge, which is the main contributing factor in chip rebonding occurrence.

As the second part, transient residual stresses of the machined surface from the previous cutting passes are modeled using a FE model, since the investigation of the mechanism of chip rebonding has shown that partial chips were rebonded on the previously machined surface where thermal stresses still exist.

Last, to model the chip rebonding effect on residual stresses, we create another FE model to simulate the chip rebonding phenomenon with the previously predicted data and investigate the effect of chip rebonding on residual stresses according to cutting parameters.

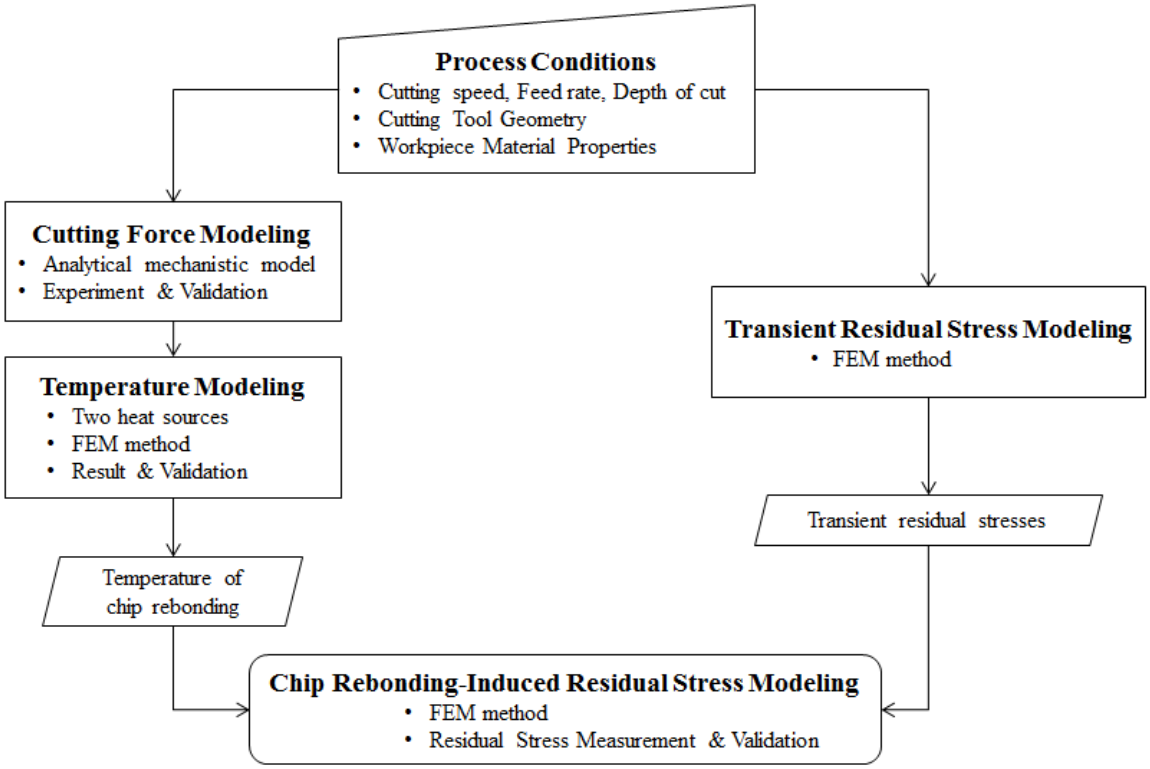

Figure 3.2 Modeling procedure for predicting residual stresses caused by chip rebonding

3.3 Temperature Modeling of Chip Rebonding

3.3.1 Literature Review of Analytical Cutting Force Model

As the understanding of the mechanism of cutting processes was improved, analytical models were formulated for cutting forces in various machining processes [38-40]. The fundamental orthogonal-cutting model proposed by Merchant, and its extension to oblique-cutting by Shaw et al. has been the basis of several force models [39, 41]. This approach is commonly known as the shear plane approach. Pal et al. applied the shear-plane model for orthogonal and oblique cutting to model the cutting forces at an element [42].

A mechanistic approach has been used to predict the force system in turning [43]. Armarego and Wright attempted to obtain the basic cutting data for the oblique cutting force prediction such as the shear stress, the chip-length ratio and the friction angle from classical orthogonal-cutting tests on a lathe. The modeling approach relied on experimentation and was mostly empirical [44].

Another approach is based on the idea that the cutting edge is divided into segments called elementary cutting tool (ECT). The cutting forces on each elementary cutting edge are calculated with a fundamental mechanistic oblique cutting model, as shown in Figure 3.3, and that summing all the forces gives the total cutting force on the cutting edge. The specific cutting forces are empirically related to fundamental machining parameters, and the model coefficients are determined from calibration experiments. This modeling approach has been successfully applied to predict the forces for various types of tool geometry [45, 46].

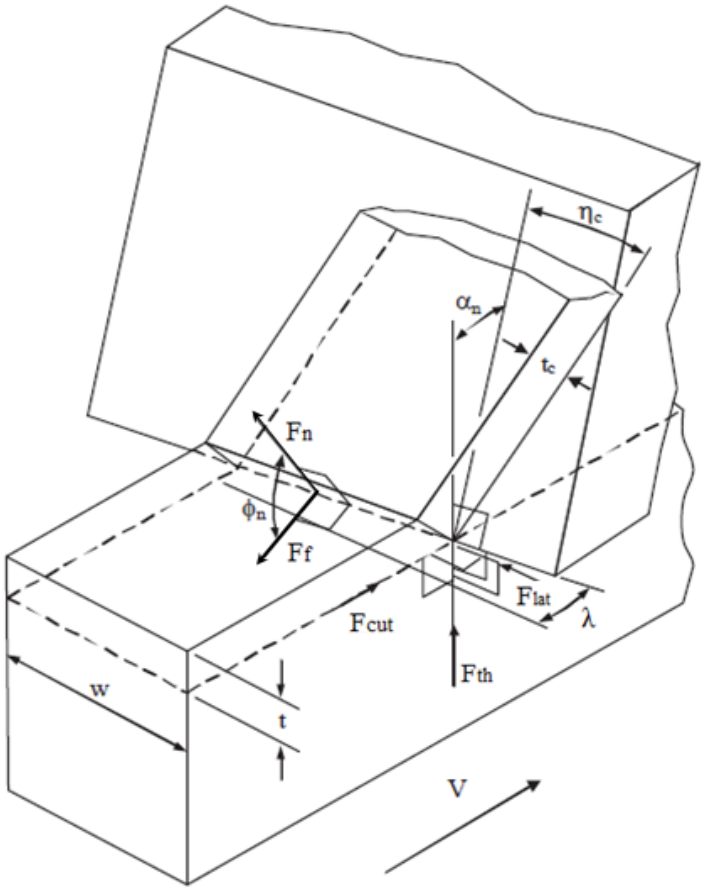

Figure 3.3 Oblique cutting model [39, 41]

3.3.2 Analytical Cutting Force Model

The mechanistic force model for elementary cutting edges of a round tool requires the calculation of the friction and normal forces on the tool rake surface. The magnitude of the friction force F_f and normal force F_n are calculated from the mechanistic equation at the rake with uncut chip area:

$$\left|\overline{F}_n\right| = K_n A_c, \qquad \left|\overline{F}_f\right| = K_f A_c \tag{3.1}$$

where K_n, K_f, and A_c are the specific normal cutting pressure, the specific friction cutting pressure, and the chip area, respectively. Chandrasekharan et al. used K_n and K_f of the form [47]:

$$\ln K_n = a_0 + a_1 \ln t_c + a_2 \ln V + a_3 \ln(1 - \sin \alpha_n) + a_4 \ln t_c \ln V \tag{3.2}$$

$$\ln K_f = b_0 + b_1 \ln t_c + b_2 \ln V + b_3 \ln(1 - \sin \alpha_n) + b_4 \ln t_c \ln V \tag{3.3}$$

where t_c, V, and α_n represent the uncut chip thickness, cutting velocity, and normal rake angle, respectively. The model coefficients for a ceramic tool and the workpiece of Inconel 718 are determined from calibration experiments as shown in Table 3.1; the procedure for which was described in Hamade et al.'s study [48].

Table 3.1 Coefficients of K_n and K_f for a ceramic tool and Inconel 718

a_0	a_1	a_2	a_3	a_4	b_0	b_1	b_2	b_3	b_4
14.021	-2.804	0.854	-0.092	2.842	13.113	-3.913	2.259	1.130	5.4356

In Figure 3.3, cutting force , thrust force F_{th} and lateral force F_{lat} for each elementary cutting edge can be calculated from normal force F_n and friction force F_f. Moreover, the angle relations can be simplified with the assumption of Stabler's Rule equals to the inclination angle λ. The following equations for turning process are simplified from the mechanistic force model of drilling process [47]:

$$\left|\vec{F}_{i\_th}\right| = \left|\vec{F}_{i\_f}\right| \cos\phi\cos\alpha - \left|\vec{F}_{i\_n}\right| \sin\alpha \tag{3.4}$$

$$\left|\vec{F}_{i\_cut}\right| = \left|\vec{F}_{i\_f}\right| (\sin^2\phi + \cos^2\phi \sin\alpha) + \left|\vec{F}_{i\_n}\right| \cos\phi\cos\alpha \tag{3.5}$$

$$\left|\vec{F}_{i\_lat}\right| = \left|\vec{F}_{i\_f}\right| (\cos\phi\sin\phi\sin\alpha - \sin\phi\cos\alpha) + \left|\vec{F}_{i\_n}\right| \sin\phi\cos\alpha \tag{3.6}$$

The magnitude of the thrust, cutting, and lateral forces for elementary cutting edge can be obtained by summing the forces at all the elements in that region.

$$\begin{aligned} \left|\vec{F}_{all\_th}\right| &= \sum_{i=1}^{n} \left|\vec{F}_{i\_th}\right| \\ \left|\vec{F}_{all\_cut}\right| &= \sum_{i=1}^{n} \left|\vec{F}_{i\_cut}\right| \\ \left|\vec{F}_{all\_lat}\right| &= \sum_{i=1}^{n} \left|\vec{F}_{i\_lat}\right| \end{aligned} \tag{3.7}$$

where i is the i_{th} elements that engaged in cutting.

All vectors and parameters for each elemental cutting edge are calculated according to the geometry of tool and workpiece. The tool engagement region is calculated by depth of cut and feed rate in Figure 3.5. A loaded cutting edge of a round tool is divided into a number of finite elements, as shown in Figure 3.4. The elementary cutting edges (C_k) (division of a single cut) as shown in Figure 3.4 swipe along the direction of cutting velocity vector $\vec{V}$ and they produce a machined surface, as shown in Figure 3.5. From an elemental edge C_n, we can calculate a cutting edge vector $\vec{L}$. Then by a cross product of the $\vec{L}$ and the cutting velocity vector $\vec{V}$, a normal vector for the machined surface $\vec{N}$ is calculated in Figure 3.5

Formation of cutter boundary in face turning. From these calculations, the uncut chip thickness for each elementary cutting edge is calculated [47].

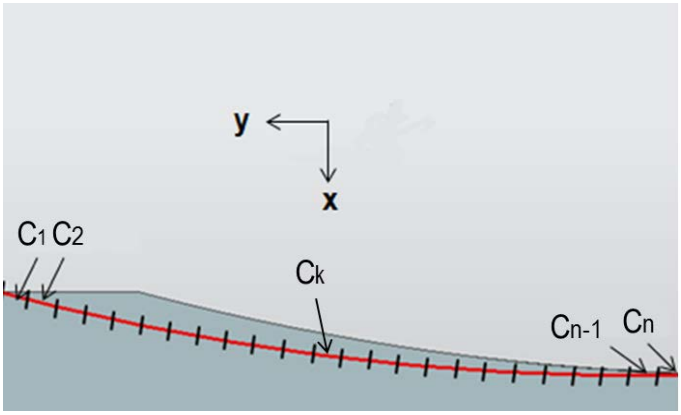

Figure 3.4 Illustration of the elementary cutting edge and boundary of uncut chip thickness in xy plane

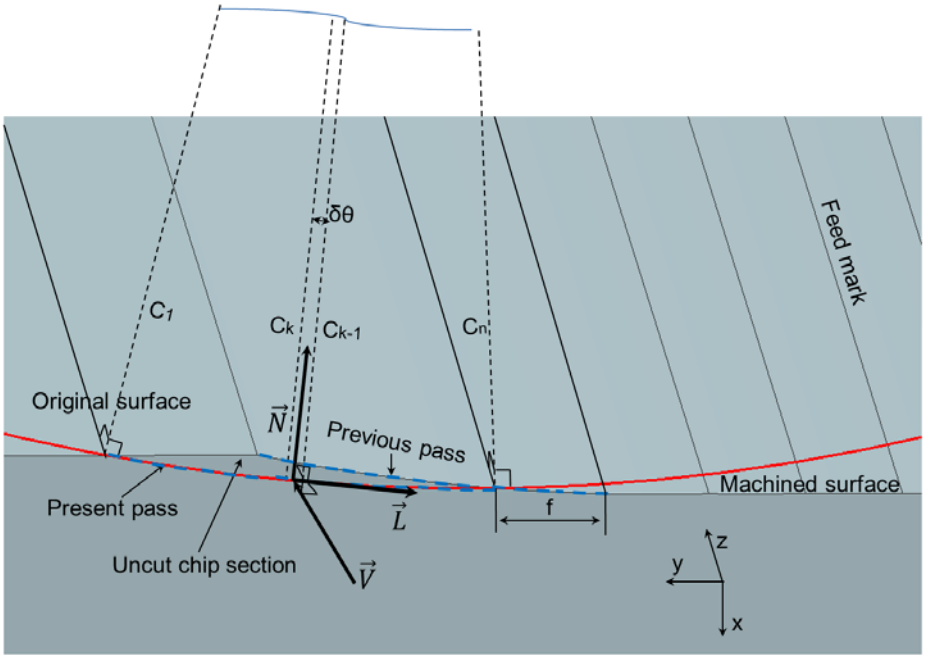

Figure 3.5 Formation of cutter boundary in face turning

To compare cutting force model with experiments, tests have been conducted. The experimental setup is the same as described in Chapter 2. Each test was performed three times with a new tool. Table 3.2 shows that the analytical force model is in good agreement with experimental results with less than 12% error over a range of machining conditions. However, the predicted forces are slightly smaller than the experimental results. This discrepancy may be due to the fact that the force model does not consider the plowing force, since we assume that a sharp tool is used.

Table 3.2. Test results for experiment and simulation

Cutting Speed (m/min)	Feed rate (mm/rev)	DOC (mm)	Experiment (N)			Simulation (N)			Error
			F_{cut}	F_{lat}	F_{th}	F_{cut}	F_{lat}	F_{th}	
55	0.076	0.076	100	13	110	92	8	96	11%
240	0.076	0.076	40	7	50	38	4	43	10%
240	0.38	0.076	120	16	110	116	9	83	12%
55	0.38	0.076	155	19	150	151	12	130	4%
55	0.38	0.38	560	110	450	541	96	434	5%
240	0.38	0.38	450	88	300	430	88	234	9%
240	0.076	0.38	150	46	155	141	32	125	12%
55	0.076	0.38	232	62	250	236	48	216	7%

After simulating a cutting process with two cutting conditions, we calculated cutting forces as normal and friction forces, and uncut chip section along the cutting edge; the results are shown in Figure 3.6.

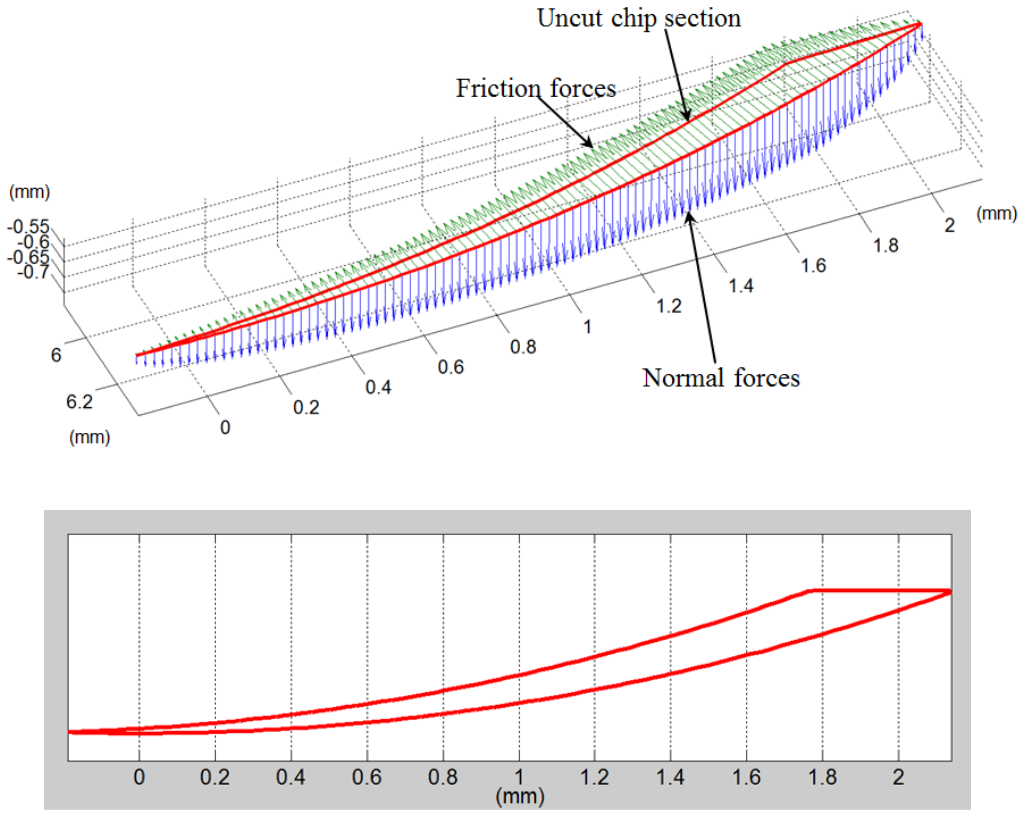

(a) Cutting speed: 240 m/min, feed rate:0.38 mm/rev, DOC: 0.38mm

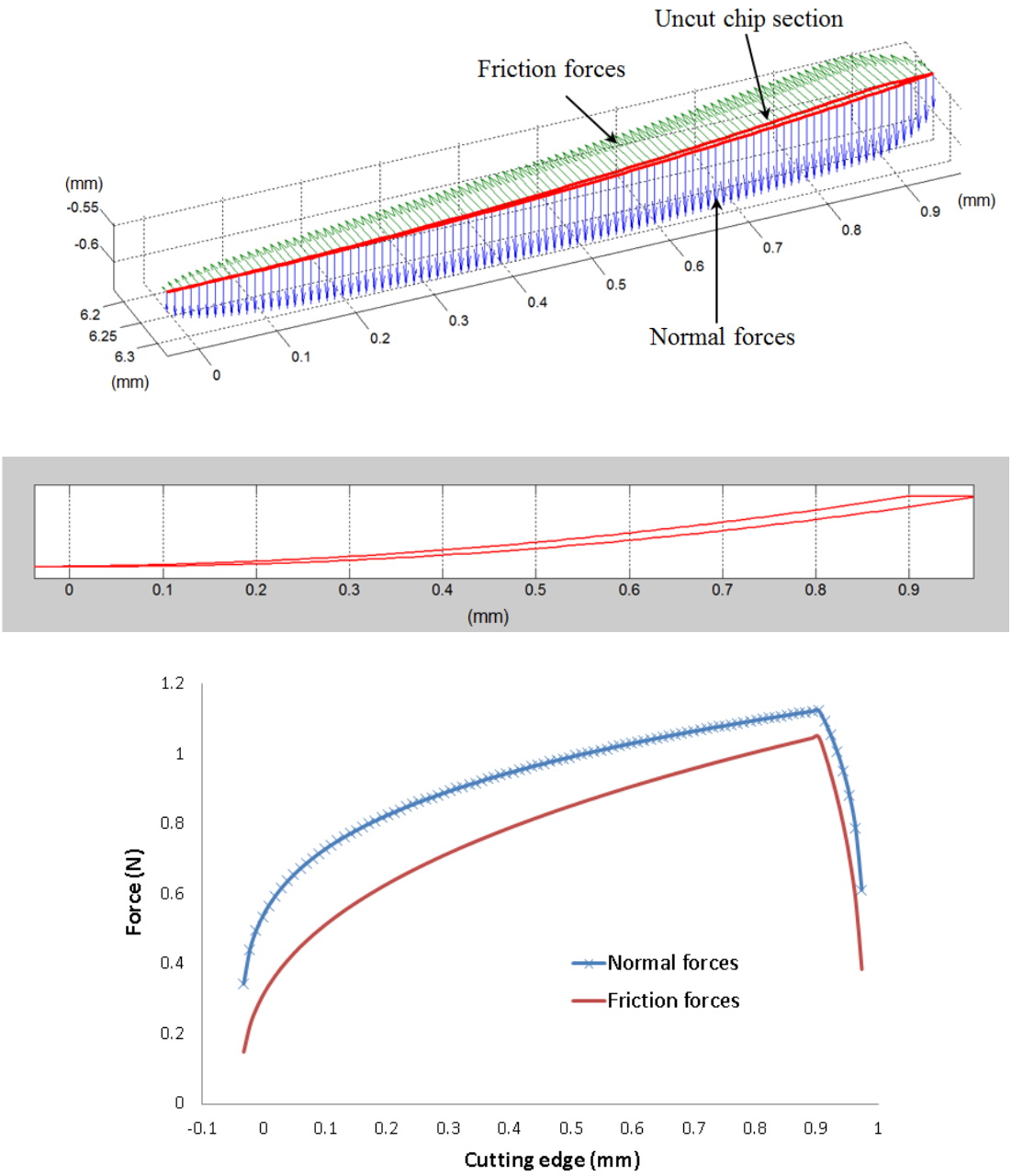

(b) Cutting speed: 55m/min, feed rate: 0.076 mm/rev, DOC: 0.076mm

Figure 3.6 Cutting force distribution along the cutting edge and uncut chip section

3.3.3 Temperature Model of Chip Cross Section

In modeling the chip temperatures, two heat sources are assumed to exist. The primary heat source (q_{shear}) is from plastic deformation in the shear zone and the secondary heat source ($q_{friction}$) comes from the friction between the tool and the chip, as shown in Figure 3.7. There is no friction heat source between tool and workpiece, since a perfectly sharp tool is assumed. The heat sources q_{shear} and $q_{friction}$ are determined from the cutting parameters and cutting forces. The resulting expressions for heat source at the shear plane and the interface between tool and workpiece are given by equations (3.8) and (3.9), respectively [49].

$$q_{shear} = \frac{\left[F_{cut}\cos(\alpha) - F_{th}\sin(\phi)\right]\cdot\left[V_{cut}\cos(\alpha)/\cos(\phi-\alpha)\right]}{t_{ch}\cdot r\cdot w\cdot \csc(\phi)} \tag{3.8}$$

$$q_{friction} = \frac{F_{fric}V_{chip}}{l_s\cdot w} \tag{3.9}$$

where t_{ch}, r, w, V_{cut}, V_{chip} and l_s represent chip thickness, chip thickness ratio, width of cut, cutting velocity, chip velocity, and tool-contact length respectively.

According to Lee and Shaffer [50], the tool-contact length can be calculated at each elementary cutting edge from equation (3.10);

$$l_s = t\frac{\sqrt{2}}{2sin\emptyset sin(45° + \emptyset - \alpha)} \tag{3.10}$$

where t is the uncut chip thickness, ∅ is the shear angle, and α is the rake angle.

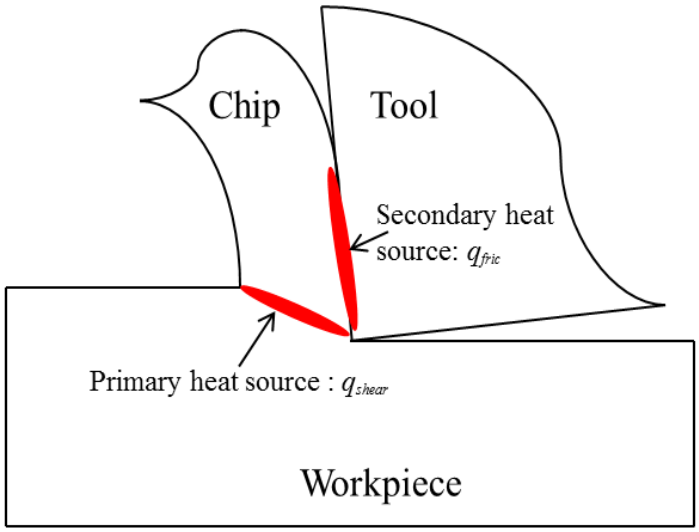

Figure 3.7 Heat sources in the orthogonal cutting

Heat fluxes are solved along the cutting edge and the modeling results according to the cutting speed are shown in Figure 3.8. As the cutting speed increases, heat flux for a shear zone and friction also increases.

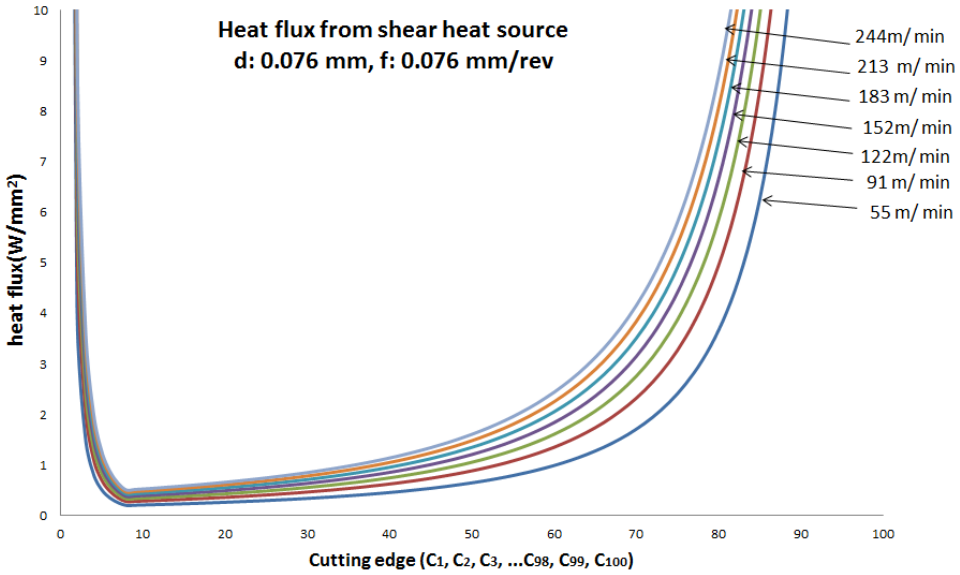

(a) Heat flux from shear heat source according to cutting speed

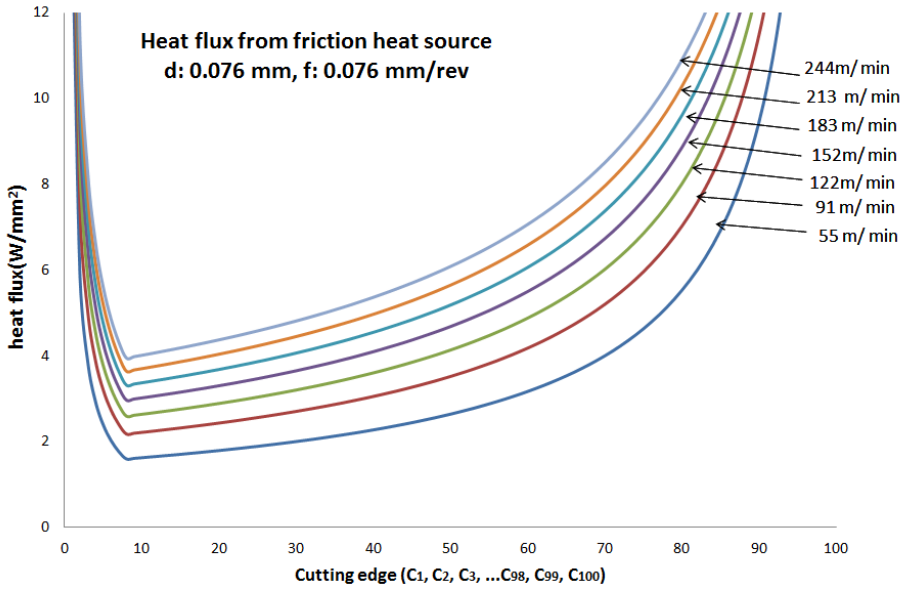

(b) Heat flux from friction heat source according to cutting speed

Figure 3.8 Results from heat flux model along the cutting edge

To predict temperature with the previous heat fluxes, the 3-D FE model is developed; the geometry is constructed from the cut chip thickness along the cutting edge, which is calculated from the uncut chip thickness calculation in Section 3.3.2. After the application of the heat flux loads to the 3D chip FE model, temperatures are distributed as shown in Figure 3.9. A quasi-static analysis is used for obtaining the stabilized temperature response. Temperatures at the both side edges are higher than those in the middle. The maximum temperature is 1187ºC at the thin side edge of the chip and the minimum temperature is 1053 ºC in the middle of the chip at the given cutting conditions.

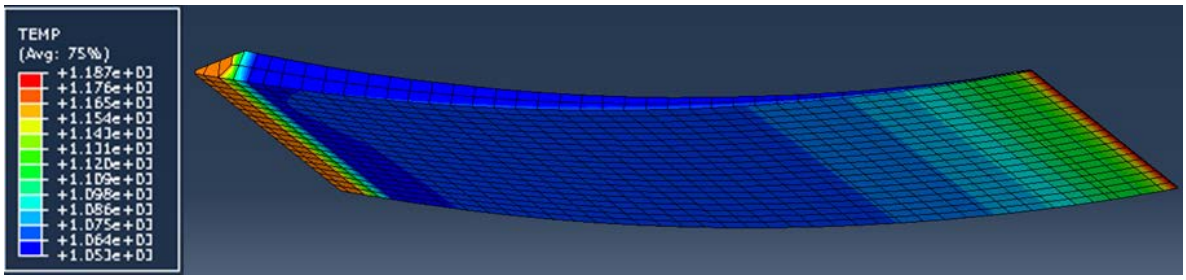

Figure 3.9 Temperature distribution of chip at the chip-tool interface at v = 300 m/min, d = 0.5 mm, f = 0.19 mm/rev

In Figure 3.10, the results from the chip temperature model are compared with experimental measurements conducted in Kitagawa's research [24]; he measured cutting temperature by embedding thermo couples at the tool-chip interface in a Si_3N_4 ceramic tool. He tested under the following cutting conditions: DOC of 0.5 mm, feed rate of 0.19 mm/rev and the cutting speeds in the range of 50- 300 m/min. After the temperatures are calculated for the same cutting conditions of his tests, the simulation results are compared to the experimental data in the range of chip temperatures obtained from the chip temperature

model, as shown in Figure 3.10. Results from the chip temperature model show good agreement with the experimental ones.

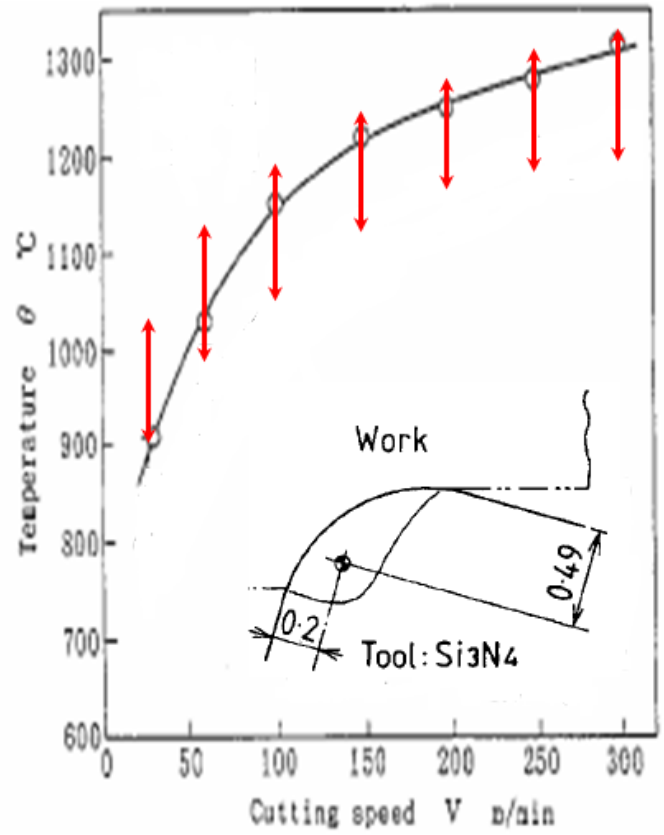

Figure 3.10 Temperature comparison of simulation results with experimental measurements [24]

3.4 Modeling of Subsurface Residual Stresses in Base Workpiece

3.4.1 Literature Review of Residual Stress Modeling

Residual stresses result from plastic deformation due to mechanical loading, thermal gradient, and phase transformation during a machining process [51]. Machining induced residual stress has been studied since the 1950s [52-56]. The modeling of residual stresses on the machined surface can be divided into two main categories: experimental approaches and analytical calculation.

El-Axir used an experimental model to predict residual stress distribution caused by turning [57]. In addition, other experimental methods such as regression analysis [58] or design of experiment methods [55, 59] have been used for the construction of a residual stress model. However, these experimental approaches are expensive and time consuming, since they require broad calibration based on the measurements of residual stresses from empirical tests.

As another approach to modeling residual stress, several researchers constructed analytical models to predict residual stress combining the effect of thermal and mechanical stresses in orthogonal machining [60-62]. However, analytical modeling is the most difficult method, since there are many unknown parameters that need to be solved with assumptions. Recently the finite element (FE) modeling has been increasingly utilized to model residual stress in machining. Ulutan et al. used this method to investigate the effect of friction on residual stresses [63, 64]. Chen et al. used a FE model to investigate the effect of flank wear and chip formation on residual stresses [65]. Liu et al. and Jawahir et al.

proposed a FE model to investigate the effect of sequential cuts on residual stresses in machining [66, 67]. Their predictions of residual stresses are generally in good agreement with the experimental measurements.

In the following section, numerical analysis for a cutting process in 2D is conducted to develop residual stress model at the machined surface. Before chip is smeared onto the machined surface, the workpiece has had residual stresses due to the previous cutting. First, a FE model is developed for orthogonal cutting of Inconel 718 to predict transient residual stresses at that time.

3.4.2 Finite Element Modeling of Subsurface Residual Stresses

The FE model is developed using ABAQUS software, which enables an explicit solution of the dynamic, coupled thermo-mechanical analysis.

The workpiece material is modeled by the Johnson-Cook model as shown in Equation (3.11) [68] .

$$\bar{\sigma} = (A + B\varepsilon^{n})\left(1 + C \cdot \ln\frac{\dot{\varepsilon}}{\dot{\varepsilon_0}}\right)\left[1 - \left(\frac{T - T_0}{T_{melt} - T_0}\right)^{m}\right] \tag{3.11}$$

where σ, ε, $\acute{\varepsilon}$, $\acute{\varepsilon}_o$, T, T_m, and T_o are flow stress, true strain, true strain rate, reference strain rate, work temperature, melting temperature, and ambient temperature respectively. Sivert et al. proposed parameters of the Johnson-Cook constitutive model for Inconel 718; A = 450 MPa, B = 1700 MPa, C = 0.017, n = 0.65, m = 1.3, T_{melt} =1297 ºC [69]. This model enables the description of the behavior of material as a function of strain, strain rate, and temperature for high speed machining. Mechanical properties and thermo physical

properties such as modulus of elasticity, thermal conductivity, thermal expansion, and heat capacity are given in Table 3.3.

Table 3.3 Material properties of Inconel 718 [70-73]

Temperature (ºC)	25	100	200	300	400	500	600	700	800	900	1000	1100	1200
Density(Kg/m^3)							8190						
Young's Modulus (GPa)	207.3	203.5	197.1	191.2	184.7	178.5	171.1	164.4	156.6	143.9	137.4	131.3	127.1
Poisson's ratio	0.3	0.3	0.31	0.31	0.31	0.32	0.33	0.34	0.35	0.36	0.36	0.37	0.37
Specific heat capacity (J/KgK)	331.7	360.8	397.2	433.6	470.0	506.4	542.8	579.2	615.6	620.1	640.1	668.3	710.1
Thermal expansion (μm/K)	12.83	13.5	14.2	14.4	17.6	19.3	21.0	22.7	24.4	26.6	27.1	28.4	29.1
Thermal conductivity (W/mK)	11.7	12.6	14.1	15.6	17.3	19.2	21.2	23.3	25.6	28.1	30.7	33.5	36.4

Chip formation is achieved through the Johnson-Cook shear failure model, which predicts that the failure occurs when the equivalent plastic strain reaches a critical value [74]. The expression is given by:

$$\varepsilon_f = (D_1 + D_2 \exp(\frac{D_3 \sigma_m}{\bar{\sigma}}) \left(1 + D_4 \ln \frac{\dot{\varepsilon}_{eq}^p}{\dot{\varepsilon}_0}\right) (1 + D_5 T) \quad (3.12)$$

where σ_m is the average stresses, $\dot{\varepsilon}_{eq}^p$ is the equivalent strain rate. Material constants D_1-D_5 for Inconel 718 were given from Singh et al.'s experiments [75]: $D_1 = 0$, $D_2 = 0.66$, $D_3 = -0.4$, D4 = - 0.017, D5 = 0.

Figure 3.11 shows the initial mesh of the workpiece and boundary conditions with the tool. A sharp tool having a rake angle of -5º is assumed as a rigid body. A CPE4RT is used as an element type. The friction between tool and workpiece is based on Coulomb's friction law. The friction coefficient is determined from experimental measurement as 0.2.

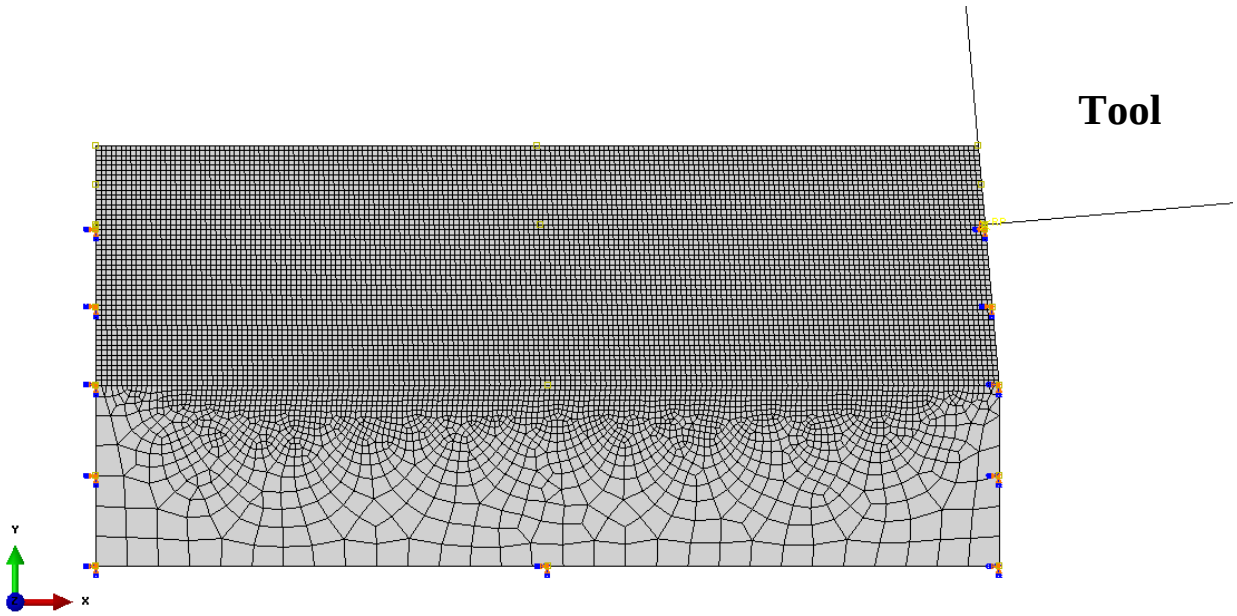

Figure 3.11 FE model configuration

3.4.3 Residual Stresses for Sequential Cuts

In a machining operation, it is often required that more than one cutting pass be made on the workpiece. During cutting, the material undergoes severe plastic deformation, and residual stresses remain in the machined surface layer. Therefore, when sequential cutting takes place, the workpiece undergoes in different material properties. Jawahir et al. and Liu et al. studied the effect of sequential cuts on the residual stresses, and they found that the distribution of residual stresses in the first cutting pass was significantly different from the distribution in the second cutting pass [66, 67].

In face turning with a round insert, there are a number of sequential cuttings passes. In the case of cutting conditions such as depth of cut of 0.127 mm, feed rate of 0.3 mm/rev, and cutting speed of 240 m/min, four sequential cuts are needed to cut up to 0.127 mm of depth. As shown in Figure 3.12 (a), chip rebonding occurs during the fifth cutting and then

the sixth cutting pass cuts out the left part of chip rebonding. These assumptions come from the observations reported in Chapter 2. As shown in Figure 3.12 (b), there are four sequential cuts before chip rebonding occurs for the selected cutting conditions.

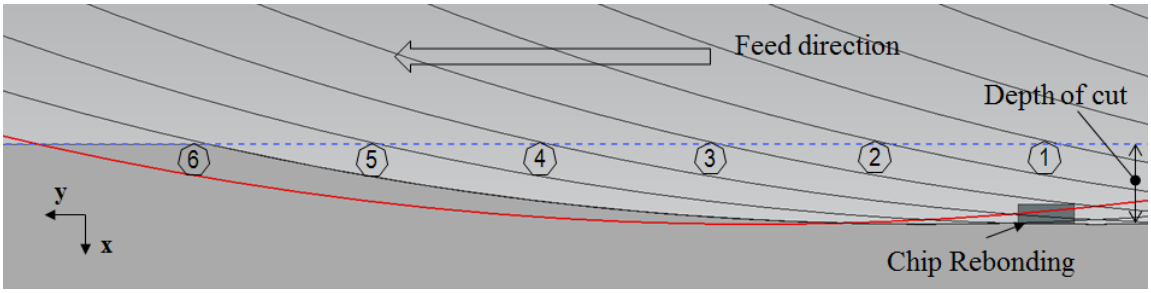

(a) Cross section of sequential cuts in face turning with a round insert

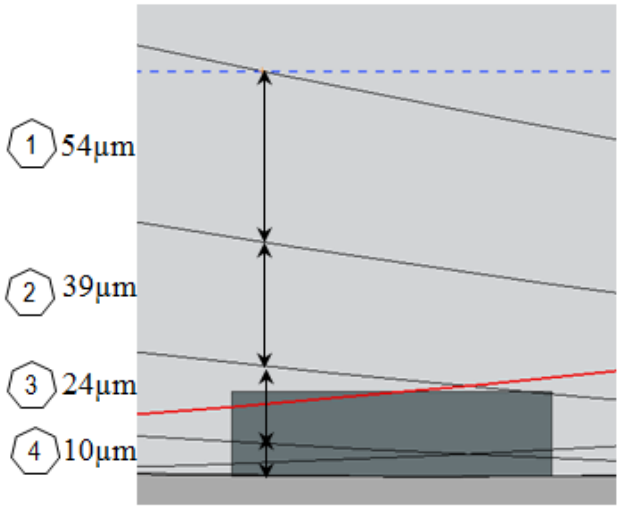

(b) Depth of each cut in the case of DOC of 0.127mm

Figure 3.12 Sequential cuts in face turning with a round insert

To predict residual stresses in the material after sequential cuttings, the material properties for the present cutting are taken from the results obtained for the previous cutting.

3.5 Finite Element Modeling of Chip Rebonding Effect on Residual Stresses

A 2-D FE model is developed to investigate the effect of chip rebonding on residual stresses. Figure 3.13 shows three parts in the chip rebonding simulation: the chip with the calculated temperature, the workpiece with residual stresses, and a tool. The temperature of the chip and the residual stress distribution from sequential cutting passes in the workpiece were calculated in Section 3.3.3 and Section 3.4.3. We assume that the initial size of the rectangular chip is based on the measurement and it will be smeared by the tool as shown in Figure 3.13.

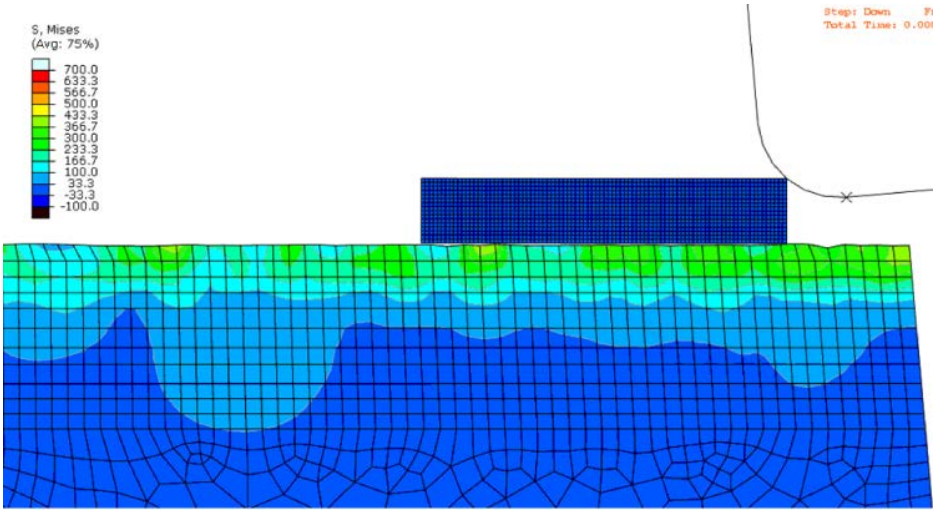

Figure 3.13 2D FE model for chip rebonding occurrence

When chip rebonding occurs, normal and shear forces are applied to the chip by the tool; the tool is assumed to be isothermal and rigid body. In real situations, the flowing chip is

propelled into the gap between the tool insert and workpiece by the force of the flowing chip. In the simulation, the chip's right bottom corner is assumed to be tied to the machined surface to prevent the chip from flying away at the moment when the tool inserts hits the chip. Right after the tool insert has smeared the chip, as shown in Figure 3.14 (a), we assume that the two materials will bond at the interface of the chip and workpiece; adhesion force at the interface will be accounted for by the assumption that nodes of the chip are tied to those of the workpiece. The simulated system cools down to the room temperature, and residual stresses are distributed in the pattern as shown in Figure 3.14 (b).

When the machined surface is exposed to local heating, the rebonded chip, which has higher temperature than the workpiece, expands. At the cooling down stage, the rebonded chip that had formerly been heated is locally shrunk more than the adjacent machined surface, and subsequently subsurface material is now subject to tensile stresses at both ends of the rebonded chip.

(a)

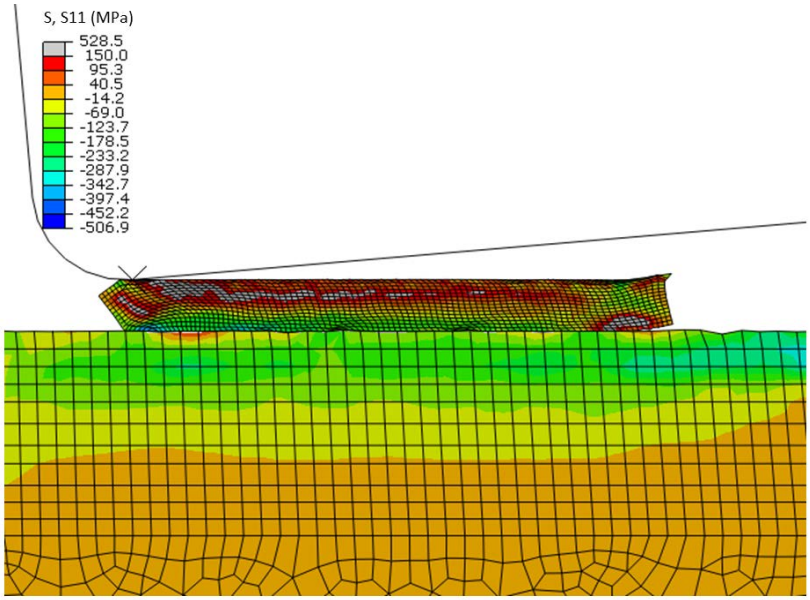

(b)

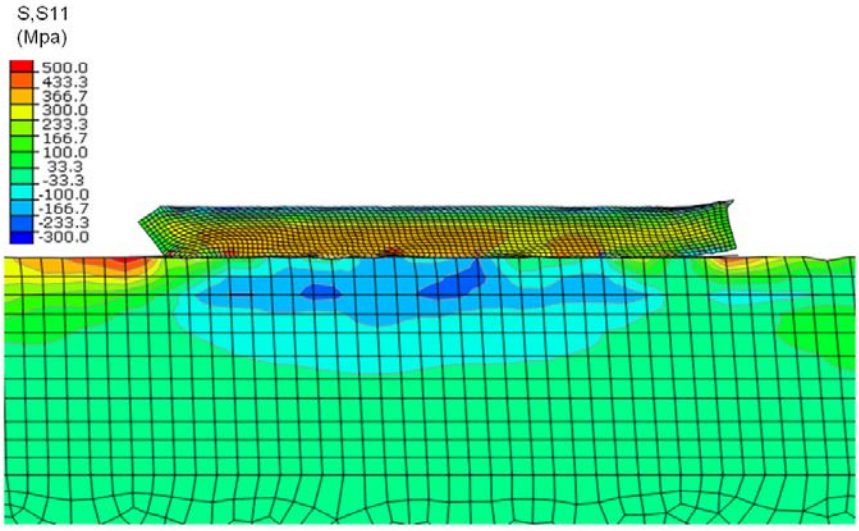

Figure 3.14 Simulation of chip rebonding occurrence (a) after chip has been smeared (b) after materials cool down to room temperature

3.6 Residual Stress Measurement of Base Workpiece with Chip Rebonding

Several different measurement methods have been developed for the evaluation of residual stress; they can be divided into two groups: destructive methods and nondestructive methods. The destructive methods are based on strain relaxation where one or more components are destroyed; these include hole drilling, saw cutting, and layer by layer sectioning techniques. Nondestructive methods leave the component unaltered by the measurement process; these include X-ray diffraction (XRD), Positron Annihilation Spectroscopy (PAS), ultrasonic wave, and neutron diffraction (ND) [76].

The spatial resolution in the above techniques belongs to the millimeter scale and thus is suitable to evaluate the macro residual stress. XRD is one of the most powerful tools for the measurement of residual stresses, but even micro XRD has been limited to modest spatial resolution: the minimum spot focus size is $150 \times 800\ \mu m^2$ [77]: at this scale it is not possible to evaluate residual stresses caused by chip rebonding phenomenon with high accuracy. For the measurement of the effect of chip rebonding on residual stresses, a nanoindentation can precisely measure in the micrometer scale.

The nanoindentation method has been developed in the past two decades for exploring mechanical properties such as micro hardness, elastic modulus, fracture toughness, and creep stress exponent. Recently the nanoindentation methods have been used to evaluate residual stresses for narrow region up to micrometer scales [78-81]. The evaluation of residual stresses by nanoindentation is mainly based upon the load-displacement curve (P-h curve) as shown in Figure 3.15. When the indenter reaches at a fixed penetration, the applied load at an area with a compressive stress state P_C is higher than that at an unstressed

state P_O. If the tensile stress is applied to the loading state, the indentation load P_O is reduced to a load P_T due to the decrease in surface penetration resistance.

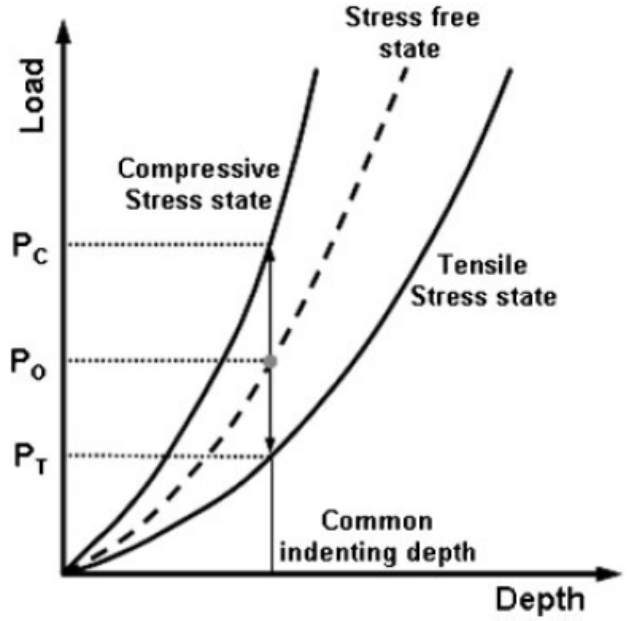

Figure 3.15 Typical nanoindentation load-displacement curves [82]

A surface residual stress is assumed to be in an equibiaxial state and uniform in the near-surface region [83]. The stress tensor is separated into mean stress σ^M (hydrostatic stress) and plastic-deformation-sensitive shear deviator stress σ^D. The surface-normal deviator stress in z direction (normal to the surface of indentation) $\sigma^D{}_z$ is $-2/3\ \sigma_{res}$ by removing the hydrostatic stress $2/3\ \sigma_{res}$ from the surface residual stress σ_{res} and is added to the contact pressure [82]. $P_T - P_O$ is defined as a product of the selected deviator stress component and its corresponding contact area A. Thus, an equation for the residual stress is derived in terms of the indentation load and contact area as the following equation [82]:

$$\sigma_{res} = 3\frac{P_T - P_O}{2A} \tag{3.13}$$

A piece of the workpiece with chip rebonding was cut off and then mounted into resin. The following cutting conditions were used: cutting speed = 100 m/min, depth of cut = 0.076 mm, and feed rate = 0.18 mm/rev. The face of the specimen was then ground and polished. Nanoindentation testing was performed with a Nano Indenter ® II. The maximum depth of indentation was 500 nm and the maximum indentation force was 80 mN.

The first array was located 5 μm under the machined surface and a total of 65 points were tested in the subsurface material, as shown in Figure 3.16. The spacing between adjacent points was 15 μm, 30 times the indentation depth, to avoid indentation size effect.

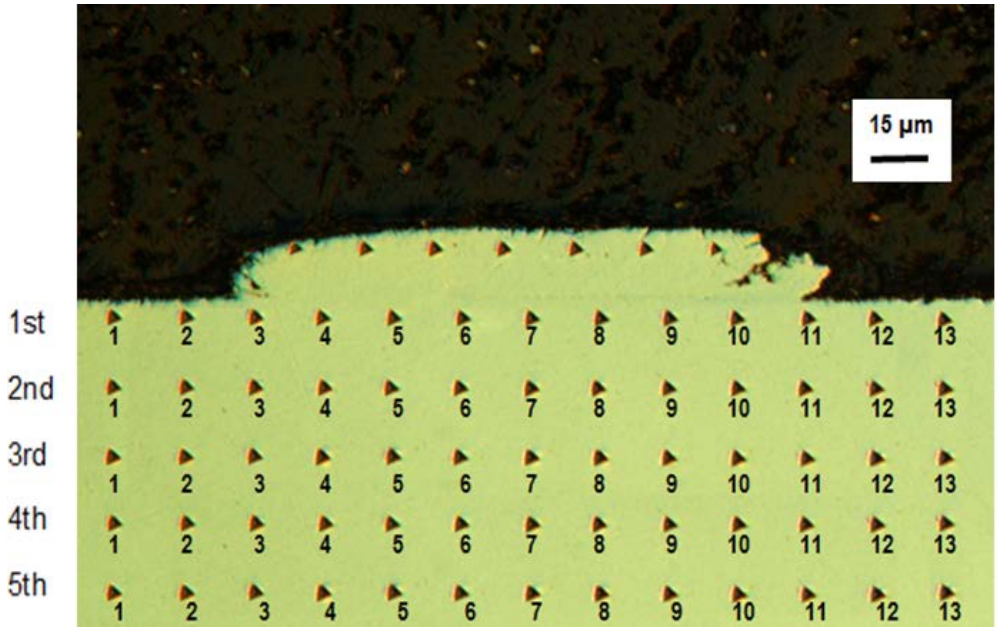

Figure 3.16 Arrays of indentations around chip rebonding in Inconel 718

Figure 3.17 shows the measured P-h curves for the first array and the stress free points. Three points for the stress free curves were measured 3 mm below the machined surface. The P-h curves for indentation numbers 1, 2, 3, 11, 12, 13 were measured below the corresponding stress free P-h curves; this means that the residual stresses at the both ends of the rebonded chip were tensile. The magnitude and distribution of residual stresses under the rebonded chip along the cutting direction are given in Figure 3.18; the maximum tensile stresses occurred at both ends and the maximum compressive stress occurred under the rebonded chip. As the depth of subsurface material increases, compressive residual stress decreases and approaches zero. Appendix A shows the measured P-h curves for the other arrays.

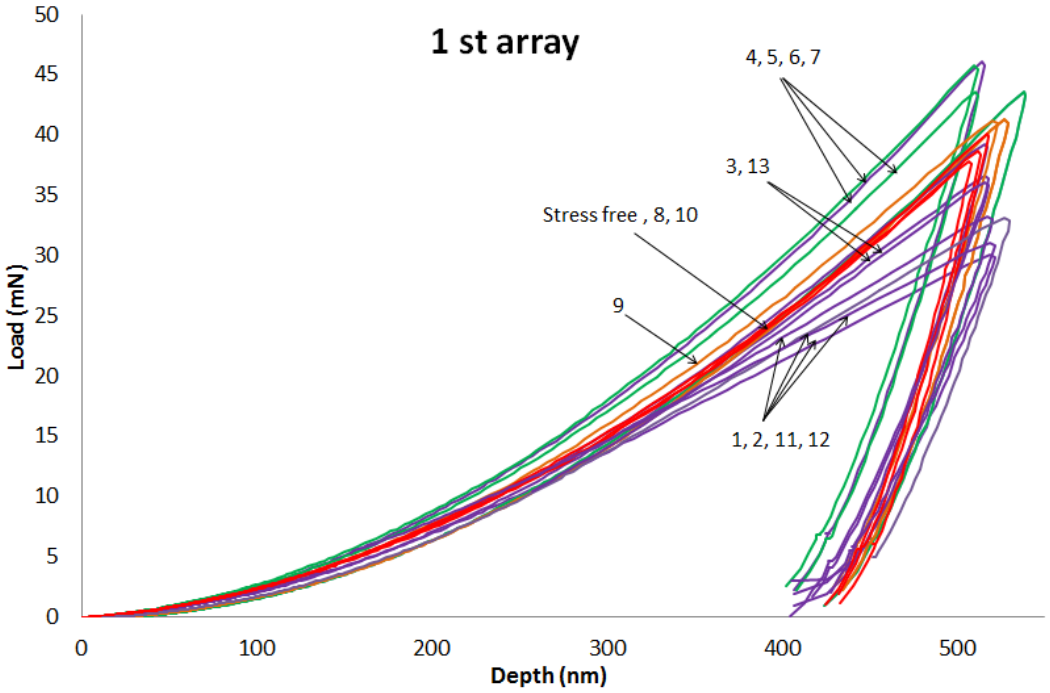

Figure 3.17 Nanoindentation load-displacement curves for the first array

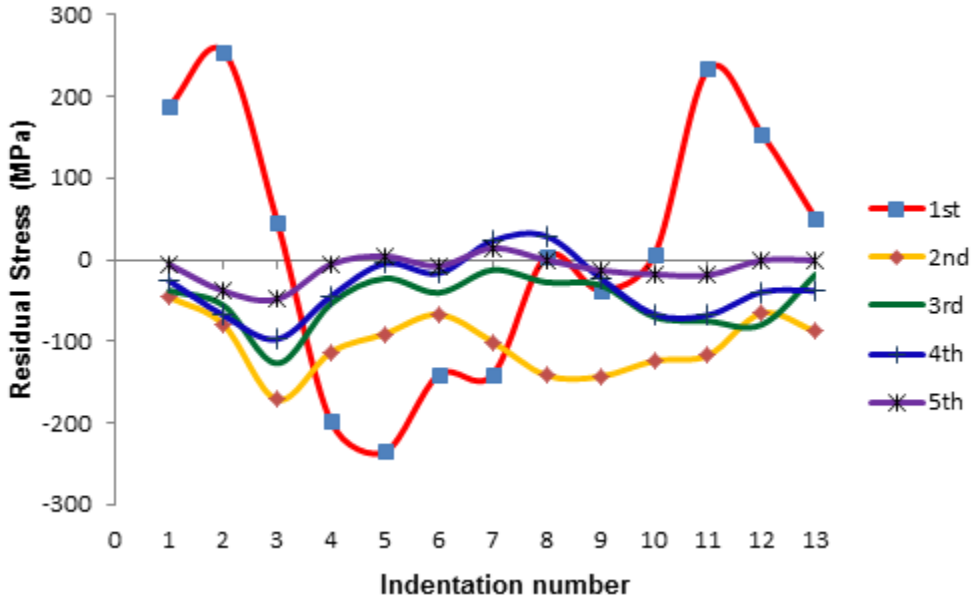

Figure 3.18 Residual stress distribution along each array

3.7 Comparisons of Computational and Experimental Results

In Figure 3.19, the measured chip rebonding shape has been compared with the shape produced by the FE simulation in the cutting direction, and the two are shown to be similar with 15 μm uniform thickness. The results from the residual stress measurements and the computation are compared in Figure 3.20. When the chip is smeared by a tool, the higher temperature in the rebonded chip than the workpiece zone produces higher thermal expansion than in the base material. When the chip cools down, the rebonded chip undergoes more relative contraction, and this leads to compressive stress in the middle section of subsurface material. As the reaction of compressive stresses underneath the rebonded chip, tensile stresses appears near the both ends of the rebonded chip. The computed residual stresses after chip rebonding agree quite well with the measured stresses.

(a) (b)

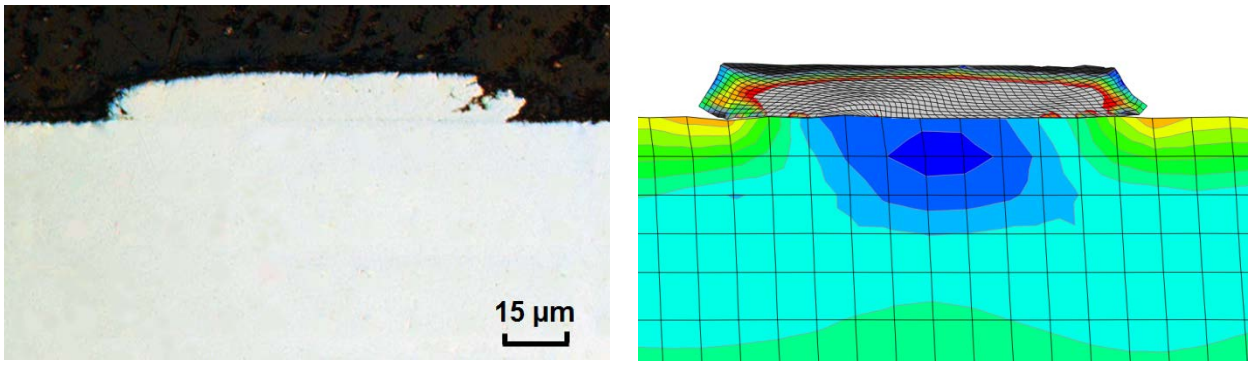

Figure 3.19 Comparison of chip rebonding shape (a) experimental measurement (250×) (b) FE simulation

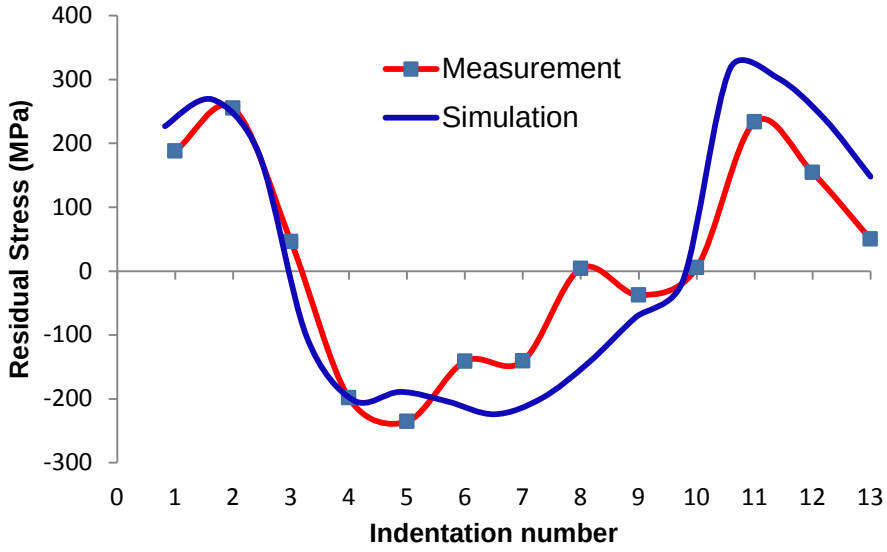

Figure 3.20 Comparison of residual stress distribution between measurement and simulation 5µm under the surface

3.8 Subsurface Residual Stresses in Relation to Bonding Area

When the chip rebonding phenomenon occurs, the full or partial area of the chip can be bonded to the machined surface according to surface quality, chip morphology, or the permeation of MWF. It is necessary to investigate the effect of the bonding area of the rebonded chip on subsurface residual stresses.

The size of bonding area is different even in a single occurrence of the one chip rebonding, as shown in Figure 3.21. Figure 3.21 (a) shows the cross section view of chip rebonding sample along the left dashed line in Figure 3.21 (c); most of the smeared chip was bonded to the machined surface except at both ends. After grinding more up to the right dashed line in Figure 3.21 (c), only the cross section of chip rebonding sample in Figure 3.21 (b) was observed; the middle section of the smeared chip was bonded to the surface with a contact length of around 30 μm.

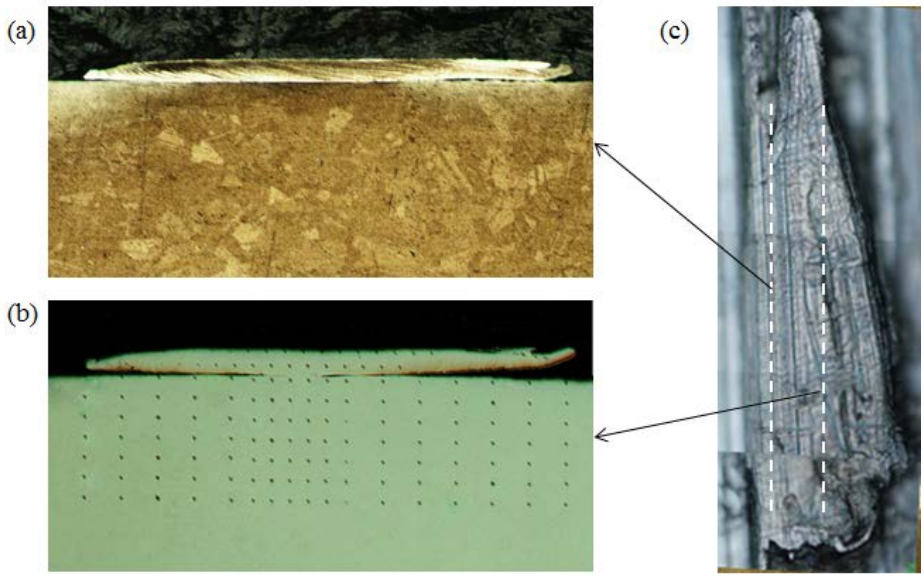

Figure 3.21 Cross section view of the rebonded chip (a) cross section view along left dashed line (100×) (b) cross section view along the right dashed line (100×) (c) top down view (250×)

For the measurements of the residual stresses, a total of 132 points were tested as shown in Figure 3.22. The first array was located 5 μm under the machined surface, and a total of 102 points were tested in the subsurface material. The spacing between indentations from indentation number five to eleven was 25 μm, and at both sides under the rebonded chip, the spacing was 50 μm. Two rows of indentation array were located in the rebonded chip, and a total of 30 points were measured. Appendix B shows the measured P-h curves for each array under the machined surface.

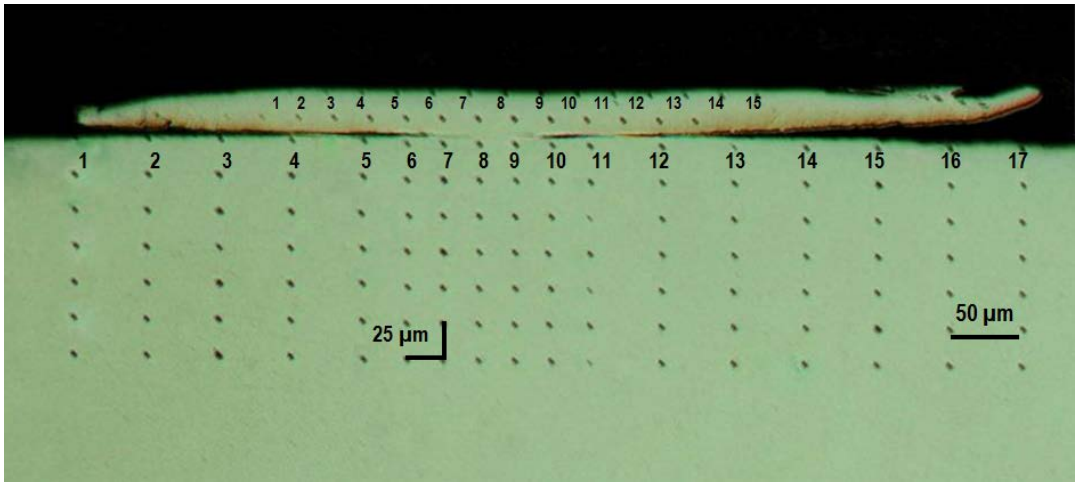

Figure 3.22 Arrays of indentations around rebonded chip in Inconel 718

Figure 3.23 and Figure 3.24 show the P-h curves at the rebonded chip along the upper and lower arrays. In Figure 3.25, residual stress distributions for these two arrays are compared. The rebonded chip has tensile stresses overall. As a tool smears the chip from right to left in Figure 3.22, higher tensile stresses are distributed toward the moving direction. In the upper part, there is compressive stress distribution around the middle section. When the chip is smeared by a tool, the higher temperature in the upper zone produces higher thermal expansion than in lower part. When the chip cools down, the relatively upper part undergoes more contraction, and this leads to subtle compressive stress in the upper middle section of the rebonded chip.

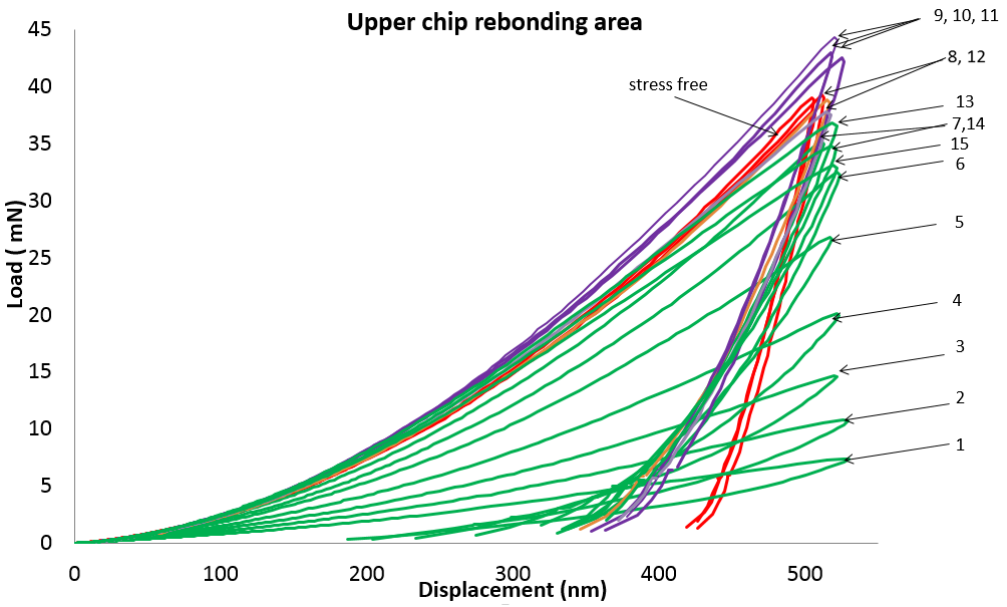

Figure 3.23 Nanoindentation load-displacement curves for the upper array in the smeared chip

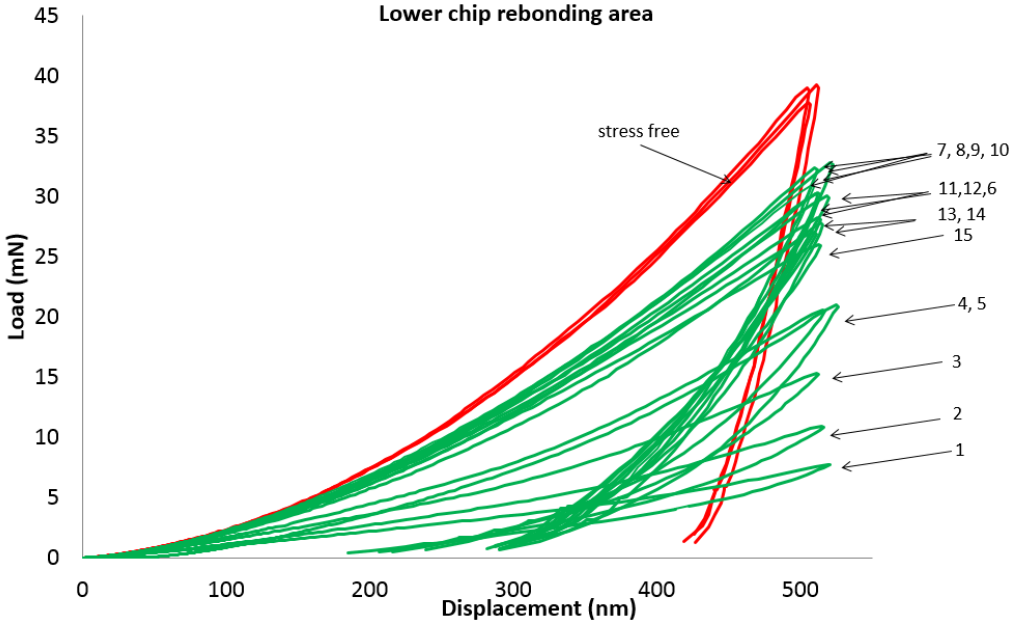

Figure 3.24 Nanoindentation load-displacement curves for the lower array in the smeared chip

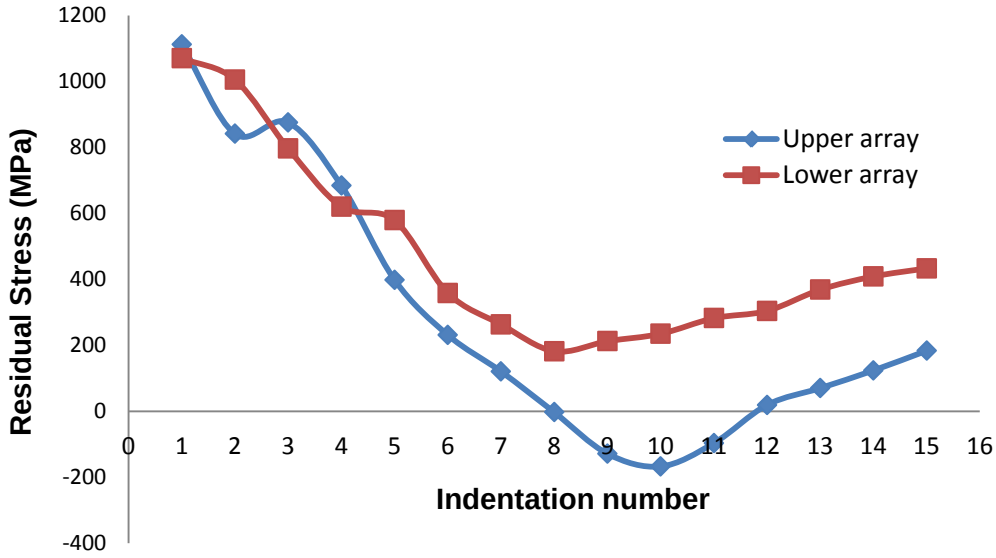

Figure 3.25 Residual stress distribution in the smeared chip

Figure 3.26 shows the case of a fully bonded chip; the experiment is compared with the simulation result. Figure 3.27 shows a partially bonded case is compared between experiment and simulation. In simulation results, the thickness of the rebonded chip is almost uniform over the entire area, but experiment results show that it is subtly thinner at both ends. Subsurface residual stresses are compared between the fully bonded case and the partially bonded case in simulation, and measurement values for the partially bonded case are shown in Figure 3.28; the size of bonded area is around 30 μm for the partially bonded case. Compressive stresses are distributed underneath the rebonded chip, and slight tensile residual stresses are shown at both sides near the rebonded chip. For the simulation of the fully bonded case, compressive stresses are distributed similar as much in the partially bonded case, and much bigger tensile stresses around 400 MPa are distributed near both ends of the rebonded chip.

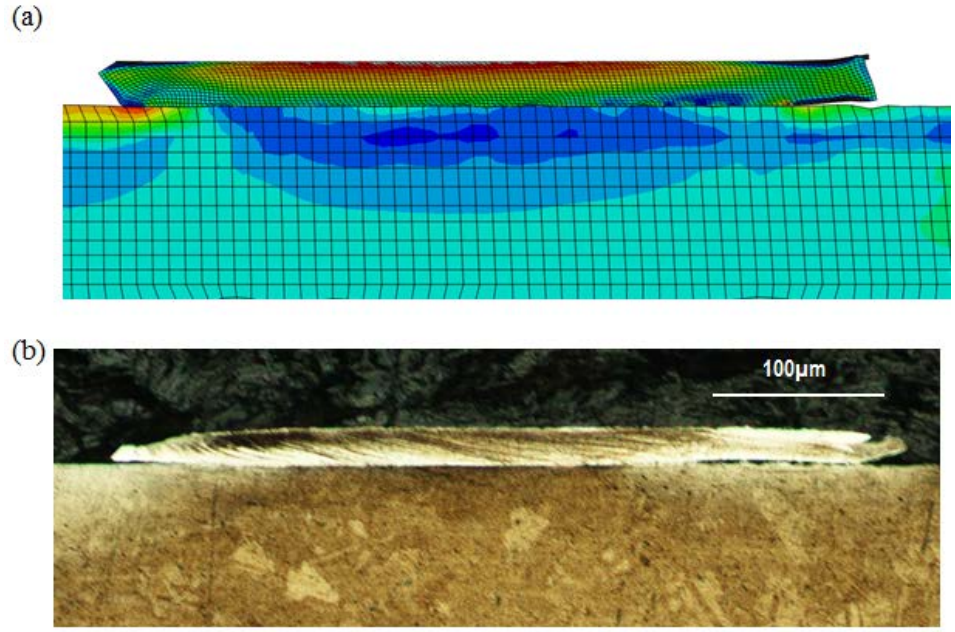

Figure 3.26 Comparison of fully bonded case (a) FE simulation (b) experimental measurement (100×)

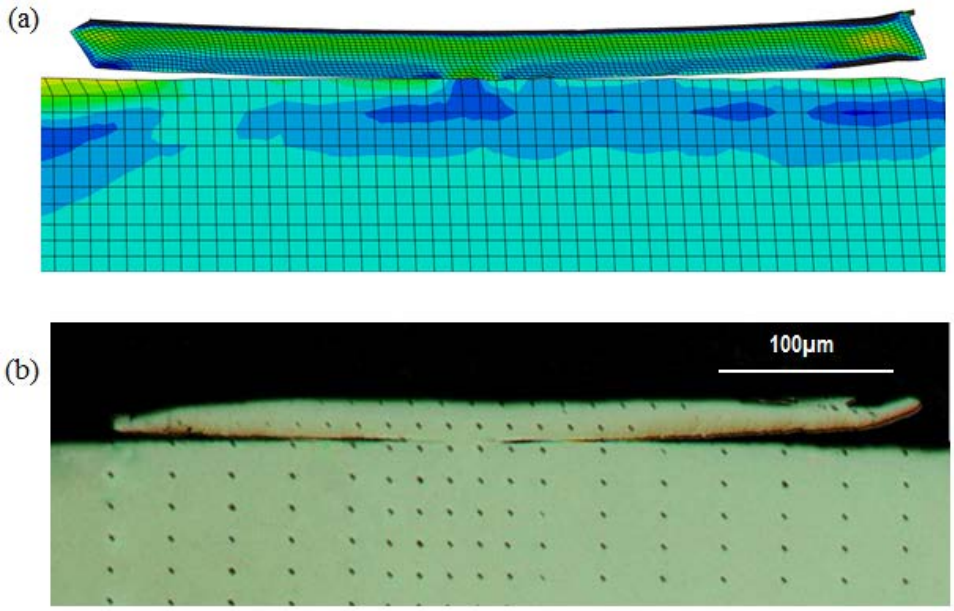

Figure 3.27 Comparison of partially bonded case (a) FE simulation (b) experimental measurement (100×)

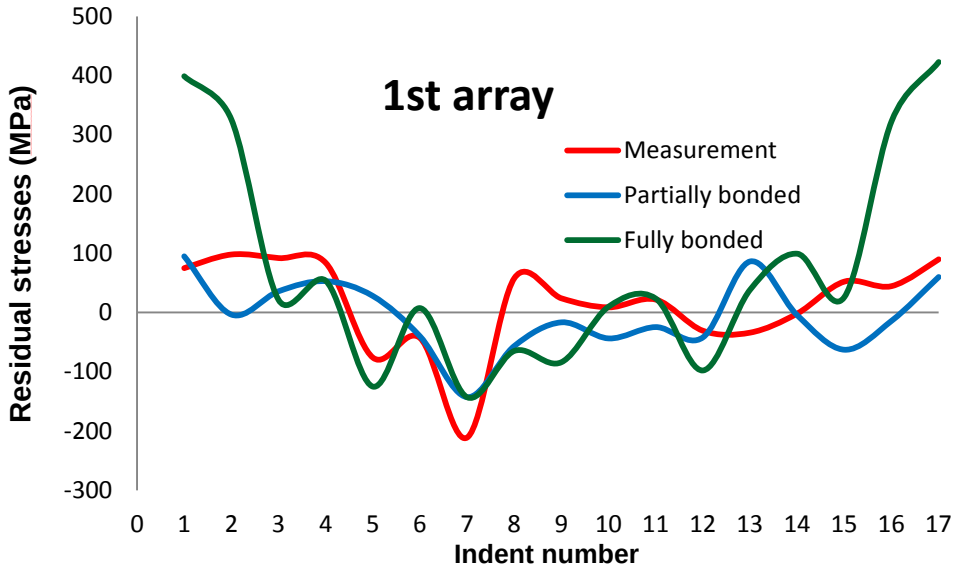

Figure 3.28 Residual stress distribution for fully bonded case and partially bonded case

3.9 Conclusions and Discussion

This chapter presents a 2-D numerical simulation to investigate the effect of chip rebonding on residual stresses. In the current work, an attempt is made to model the residual stress formation related to chip rebonding through a combination of an analytical model and FEM numerical approach.

We carried out an analytical model in face turning process of Inconel 718 with a round ceramic tool to calculate the temperature in the chip before being smeared. From the analytical model, we calculated cutting forces and heat fluxes along the elementary cutting edge. By applying the heat fluxes into the FE model of chip section, the temperature of the chip's side edge was calculated. At both side edges of chip, temperatures were calculated higher than those at the middle section.

In the final stage of modeling, we developed the FE model to simulate the chip rebonding phenomenon; the properties of the base material had been calculated from the 2-D orthogonal cutting FE model and the transient residual stresses from sequential cuttings had been predefined. In the simulation, the chip with high temperature was smeared onto the machined surface and cooled down. The change of residual stress distribution at subsurface material was investigated while chip rebonding occurred and after materials cooled down.

Subsurface residual stresses were measured by nanoindentation method and compared with simulation results. The calculated subsurface residual stresses agreed well with the experiment measurements. When the chip was smeared onto machined surface, subsurface underneath the rebonded chip had a compressive stress. After cooling down, subsurface residual stresses near the both ends of the rebonded chip were changed into tensile stress state.

Chip rebonding area can be changeable depending on cutting conditions, surface quality, or the performance of metal working fluid. Even in one rebonded chip, overall or partial bonded area existed. When high pressure in aircraft engine applies into the gap between the rebonded chip and the base material, and subsurface material adjacent the rebonded chip has the tensile stresses, we can expect the crack easily initiates near chip rebonding.

CHAPTER 4 EXPERIMENTAL INVESTIGATION OF EFFECTS OF CUTTING PARAMETERS ON THE CHIP REBONDING PHENOMENON

4.1 Introduction

To improve surface quality, it is necessary to understand the relationship between cutting process parameters and surface integrity of machined surface. Many factors affect the surface conditions of a machined part (e.g., material properties, cutting tool geometry and rigidity, cutting speed, depth of cut, feed rate, metal working fluid, etc.). Among them, three cutting process parameters including cutting speed, depth of cut, and feed rate are usually considered as the main parameters of a turning operation. The optimized choice of these cutting parameters is very important to determine the required surface quality.

A number of researches have been performed in order to investigate the effect of cutting process parameters on surface quality. It has been found that surface integrity is improved with an increase in cutting speed, a decrease in the depth of cut, an increase in tool rake angle and a decrease in tool wear land length for mild steel and aluminum alloy cut by HSS tools [84-87]. It has been reported that feed rate is the most significant factor affecting surface finish and raising the compressive residual stress, and cutting speed has very little influence on surface finish for machining of hard materials (50 - 70 HRC) [88, 89].

These effects of cutting parameters on surface quality are also applied to machining of Inconel 718. It has been found that the secondary grain boundary carbide particles in

Inconel 718 were attached to the machined surface when machining was done at lower cutting speed and at low feed rate [11, 18]. Sadat and Reddy found that an increase in cutting speed reduced workpiece surface damage by reducing the cutting forces generated due to an increase in cutting temperature and corresponding drop in workpiece mechanical strength [12]. The surfaces showed lesser flaws at the cutting speed of 475 m/min compared to the surfaces generated at 125 m/min [11].

Although there has been extensive research into the effects of operating parameters on surface roughness, tool wear, and residual stress, relatively little research concerns the effects of cutting parameters on surface defects. Among several surface defects, chip rebonding has not been evaluated. The following experimental work has been undertaken to evaluate different cutting parameters and their effects on chip rebonding, when turning Inconel 718 with round ceramic tools. The experiment uses the same setup and surface measurement instrument as the previously reported research in Chapter 2. Results in dry cutting are presented in Section 4.2 and results in wet cutting are shown in Section 4.3.

4.2 Experimental Investigation in Dry Cutting

Recently a number of studies have been performed on the feasibility of dry cutting Inconel 718 [90-92] due to the advantages including manufacturing cost reduction, non-pollution of environment, and hazard reduction to machine operators. In this section, dry machining and high cutting speeds are associated to study the effect of cutting parameters on chip rebonding occurrence during the face turning of Inconel 718 with round ceramic tools. Cutting forces and surface quality are measured, and chip shapes are observed for

various cutting conditions. This research explains the main effects of cutting parameters on chip rebonding.

The three controllable factors under investigation in this study are cutting speed, feed-rate and depth of cut (DOC). For each factor, appropriate levels need to be determined. Typical cutting speeds for machining Inconel 718 with ceramic inserts range from 55 m/min to 240 m/min; feed rate ranges from 0.076 mm/rev to 0.38 mm/rev, and DOC ranges from 0.076 mm to 0.38 mm. Those cutting conditions are widely used in industry and recommended by the tool manufacturer. Using these ranges, a 3×2 design of experiments, shown in Table 4.1, was constructed. A 2^3 (three factors, two levels) full factorial design is used. The test matrix is shown in Table 4.2. Each test was performed three times.

Table 4.1 Control factors in dry machining experiment

Factor \ Level	1	2
Cutting Speed (m/min)	55	240
Feed Rate (mm/rev)	0.076	0.38
Depth of cut (mm)	0.076	0.38

Table 4.2 A 2^3 full factorial design in dry machining experiment

Test run	DOC (mm)	Feed rate (mm/rev)	Cutting speed (m/min)
1	0.076	0.076	60
2	0.076	0.076	240
3	0.076	0.380	240
4	0.076	0.380	60
5	0.380	0.380	60
6	0.380	0.380	240
7	0.380	0.076	240
8	0.380	0.076	60

Note: For each test, a new cutting tool was used. After each test-run, a cleanup pass was made prior to the next test-run.

4.2.1 Interval Plot of R_t and R_a

Figure 4.1 shows an interval plot of R_t and R_a with cutting conditions following the test matrix design. R_a and R_t are the arithmetic average of the absolute values and the range of the collected roughness data points respectively. At the high feed rate, the variations of R_t and R_a at test runs 3, 4, 5, and 6 are small, while variations are large with the low feed rate at test runs 1, 2, 7, and 8 as shown in Figure 4.1. According to the theoretical surface roughness of R_a, R_a should be smaller as the feed rate decreases. However, experimental results show an opposite trend. At the lower feed rate, flowing chips tangled and hit the surface. These actions produced anomalies such as chip rebonding and scratches on the

machined surface. When R_t is below 10µm, chip rebonding is not detected. Chip rebonding occurs in tests 1, 2, 7, and 8 where average height of the profile, R_t, is over 20µm.

(a)

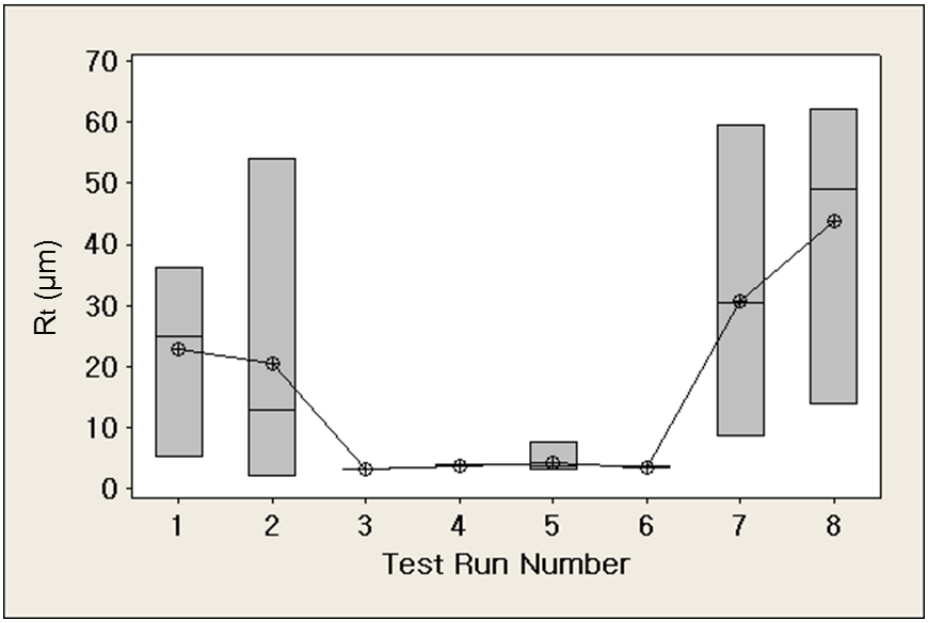

(b)

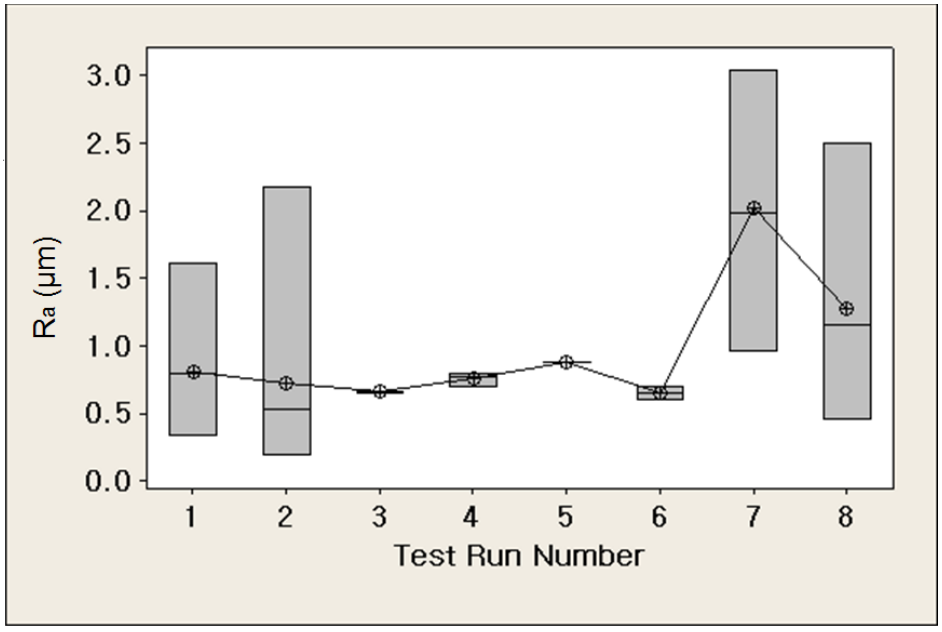

Figure 4.1 Interval plot of (a) R_t and (b) R_a at each test-run

4.2.2 Effects of Parameters on Roughness R_t and R_a in Dry Cutting

The main effects of the three machining parameters on R_t and R_a are shown in Figure 4.2. It is found that the feed rate has significant effect on R_t and R_a. DOC and cutting speed do not affect R_t and R_a as much as feed rate, as shown in Figure 4.2. Furthermore, R_t and R_a decrease as the feed rate increases. In conclusion, the highest feed rate tested produces the lowest R_t.

(a)

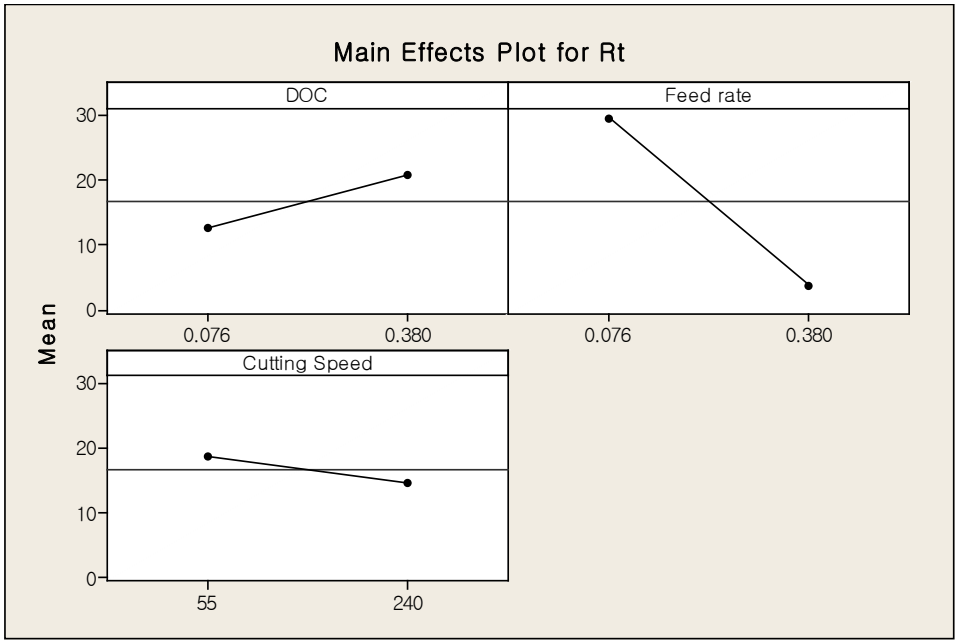

(b)

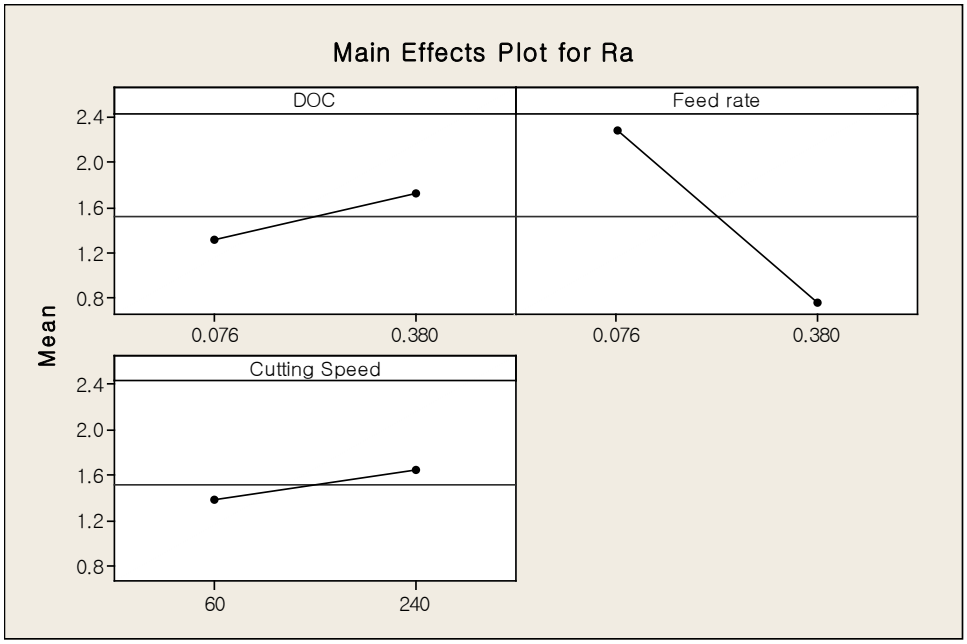

Figure 4.2 Main effects plot for (a) R_t and (b) R_a in dry cutting

4.3 Observation of Chip Flow Direction in Dry Cutting

From the previous analysis of three cutting parameters, it is found that the feed rate has the strongest effect on both chip rebonding and surface quality.

Furthermore, we use a high-speed camera to observe the chip flow direction as well as to produce additional insights into chip rebonding mechanism. At the low and middle feed rates, the chip curves back to the workpiece surface and produces tangled chips, as shown in Figures 4.3 (a) and (b). On the other hand, the chip flows relatively straight, as seen in Figure 4.3 (c) at the high feed rate of 0.38 mm/rev.

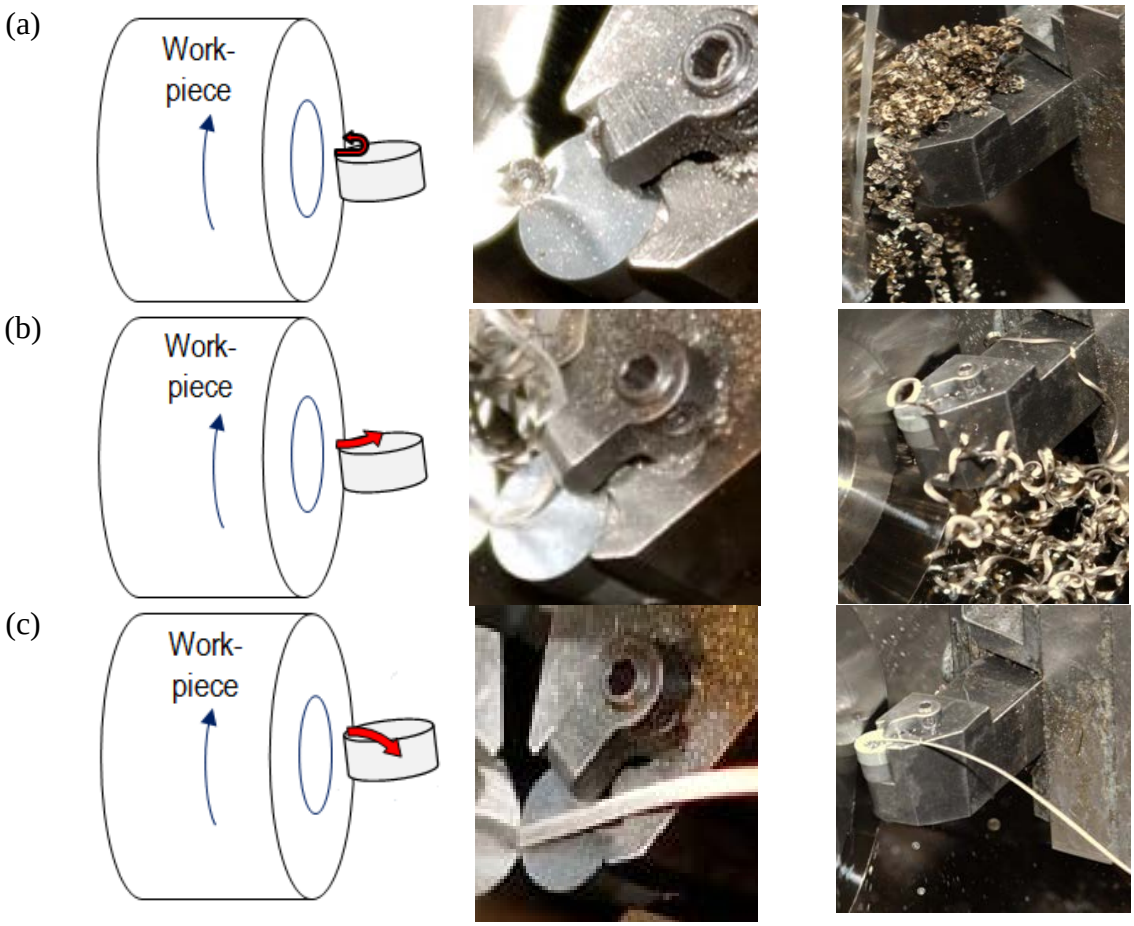

Figure 4.3 Observation of chip flow (a) chip flow at the low feed rate of 0.076 mm/rev (b) chip figure at the middle feed rate of 0.228 mm/rev (c) chip flow at the high feed rate of 0.38 mm/rev

In Chapter 2, we observed that the torn chips at the chip's side edge caused the chip rebonding phenomenon. To investigate the effect of cutting conditions on chip morphology at the side edge of chips, the tests in Table 4.3 were performed and the chip morphologies resulting from each test run are shown in Figure 4.4.

In dry cutting, the feed rate has the strongest effect on chip flow direction. At the lower feed rate, test runs 1, 2, and 3 result in a more curved chip shape than the ones from test runs 4, 5, and 6. In these results, cutting speed has a slight effect on the curvature of the

chip shape. As the cutting speed increases, the curvature of the overall chip shape increases at the lower feed rate. At the higher feed rate, cutting speed does not have significant effect on the overall chip curvature, as shown in test runs 4, 5, and 6.

Torn chip morphology at the side edge of the chip shows a pattern: at low feed rate, both the length of periodicity and size decrease as cutting speed increases. At the high feed rate, periodicity does not change significantly with cutting speed, but size is consistently smaller.

Table 4.3 Test matrix for chip morphology

Test Run	Feed rate (mm/rev)	Cutting speed (m/min)	DOC (mm)
1	0.127	60	0.127
2	0.127	150	0.127
3	0.127	240	0.127
4	0.38	60	0.127
5	0.38	150	0.127
6	0.38	240	0.127

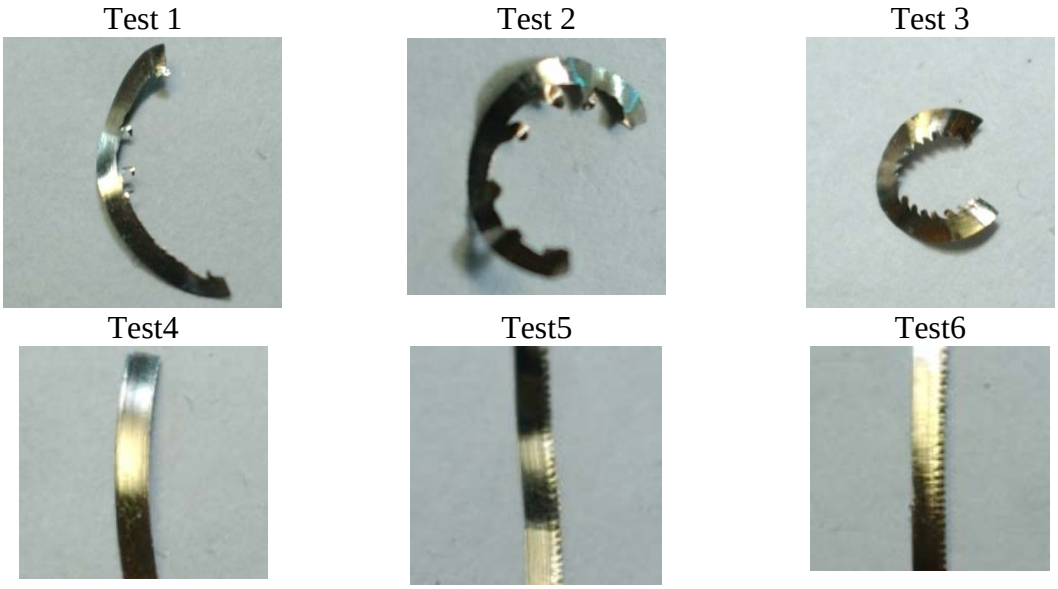

Figure 4.4 Chip morphology depending on cutting conditions

In Chapter 2, overall observations of chip rebonding on the machined surface showed that chip rebonding repeatedly occurs along a feed mark, and that the chip's side edge is periodically torn and curled. Moreover, we confirmed that the low feed rates have the strongest effect on causing chip rebonding in dry cutting.

4.4 Experimental Investigation in Wet Cutting

Though many publications of surface integrity with metal working fluid (MWF) have been studied, there has been insufficient understanding of the effect of MWF on the chip rebonding phenomenon. The following experimental studies are undertaken to evaluate MWFs with different concentrations, viscosity, and their effects on chip rebonding when turning Inconel 718 with ceramic tools. For MWFs, we used pure water and two

commercial lubricants with different concentrations such as CIMTECH 310-1%, CIMTECH 310-3%, CIMTECH 310-5%, CIMTECH 320-1%, CIMTECH 320-3% and CIMTECH 320-5%.

4.4.1 Description of Metal Working Fluid

MWFs in machining operations have been used since early 1900s to achieve the following purposes [93, 94].

- Supply lubrication and cooling
- Decrease cutting forces
- Increase tool life
- Maintain dimensional accuracy
- Improve surface finish
- Carry away debris
- Protect finished surfaces by leaving behind a corrosion-resistant film

To investigate the effect of MWF on chip rebonding, it is necessary to understand what the functions of MWF are and how MWF works during metal cutting. MWF provides a layer of lubricant between a tool and a workpiece to reduce friction, and then the reduced friction leads to decreased cutting force and temperature at the tool-chip interface. MWF also works as a coolant to reduce the heat produced during machining [95]. Further, MWF keeps metal from picking-up on both the tool and the workpiece by flushing away the chips. All of these functions reduce cutting energy requirements, increase tools life, and produce good surface quality on machined product [96].

Generally, MWFs are grouped into four categories: straight (mineral) oils, soluble oils, semisynthetic fluids, and synthetic fluids. Straight oils are solvent-refined petroleum oils and they were the most predominant lubricating fluids used until the early 1980s [97]. Soluble oils have emulsifying agents to maintain the oil-water mix as an emulsion [98, 99]. Semi-synthetic fluids contain fatty acids, phosphorus, sulfur, and chlorine derivatives to provide lubrication for high cutting speeds [97]. Synthetic fluids are oil-less, and consist of dissolved materials including sulfur, chlorine or phosphorous additives to give extreme pressure qualities. Synthetic fluids are usually used for machining of Inconel 718 because they have lubricating properties that can be further improved than other MWFs [97, 98].

As the load increases between two mating surfaces, we can observe three different forms of lubrications in MWFs: boundary lubrication, mixed film lubrication, and hydrodynamic lubrication as shown in Figure 4.5 [100]. In boundary lubrication, the two surfaces come into closer contact at their asperities. In the hydrodynamic regime of lubrication, two surfaces are completely separated from each other by thick fluid film [94]. In mixed film lubrication regime, a thin layer of lubricant film physically adheres to the surfaces by molecular forces or chemical forces [94]. If the protective boundary layer is destroyed, friction and wear will be high. Therefore, the adherence and strength of this film is a very important factor in this regime's effectiveness.

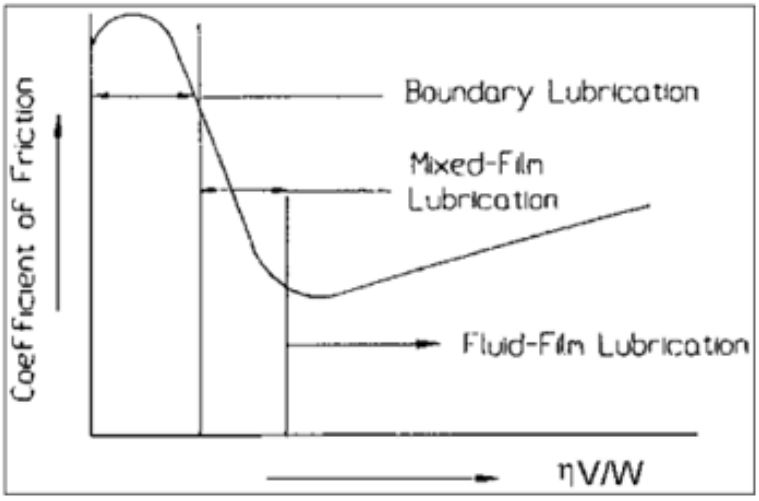

Figure 4.5 Stribeck curve (η: oil viscosity, V: sliding velocity, W: normal load) [100]

To improve the performance of MWF, various additives have been developed [93]. Under severe machining conditions, extreme pressure (EP) additives are added to MWF to form a lubricant film on metal surfaces and prevent welding, metal transfer and surface defects [94, 101, 102]. Chlorine, sulfur, copper or phosphoric compounds are frequently used as EP additives in MWFs. Figure 4.6 summarizes all known EP additives for water soluble MWFs and their effect on friction coefficient depending on activation temperature [102]. Alkanolamines, triethanolamine, diethanolamine, and monoethanolamine are used as organic additives to stabilize pH or inhibit corrosion, [102].

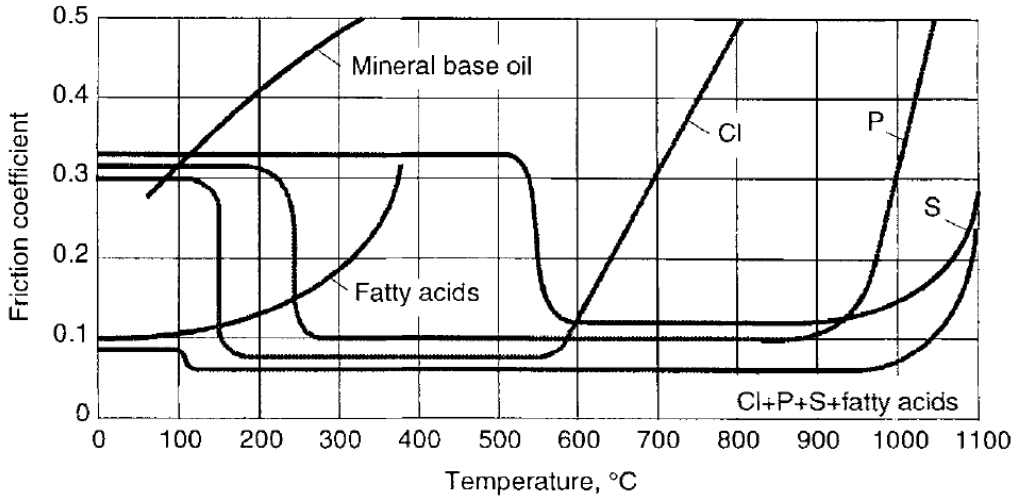

Figure 4.6 Temperature effect on EP additive activity (Cl: Chlorine, P: Phosphorus, S: Sulfur) [102]

In another study, it has been tried to improve the MWF performance by applying MWFs in high-pressure system in the machining of Inconel 718. Sorby compared applying high-pressure MWF to different tool surfaces, and found out that the surface finish was better when applying to flank surface than to rake surface. However, chip adhesion to workpiece surface was still found in high-pressure flank face cooling [103]. It was reported that the use of high-pressure MWFs could reduce cutting force, but resulted in increased workpiece surface roughness due to high levels of built up layer on the tool [104]. Ezugwu found out that redeposited materials occurred on the machined surface when machining with both conventional and high-pressure MWF supplies and under all the cutting conditions [7, 105].

We apply the flood coolant in the following experiments, since high-pressure coolants did not prevent surface defects well and the flood coolants are still widely used in industry. Though many publications of surface quality with MFW have been studied, there has been

insufficient understanding of the effect of MFW on the chip rebonding phenomenon. The following experimental work is undertaken to evaluate different cutting parameters and their effects on chip rebonding in wet cutting when turning Inconel 718 with ceramic tools.

4.4.2 Experimental Setup and Results in Wet Cutting

We use an external MWF reservoir of 40 liters (flood coolant system) and set the flow rate to 2L/min. MWF supplies at pressures around 4 bar. When we use pure water as MWF, test results in Table 4.4 are almost the same as in dry cutting. Under the low feed rate of 0.76 mm/rev, test results show chip rebonding. At the high feed rate of 0.38 mm/rev, no chip rebonding occurs, mainly because the high feed rate makes straight and continuous chip shape.

Table 4.4 Test matrix and results with pure water

Test run	DOC (mm)	Feed rate (mm/rev)	Cutting speed (m/min)	Chip rebonding
1	0.076	0.076	60	O O O O O
2	0.076	0.076	240	O O O O O
3	0.076	0.38	240	X X X X X
4	0.076	0.38	60	X X X X X
5	0.38	0.38	60	X X X X X
6	0.38	0.38	240	X X X X X
7	0.38	0.076	240	O O O O O
8	0.38	0.076	60	O O O O O

* O: Chip rebonding, X: No chip rebonding

To observe the effect of various concentrations with different kinds of MWF on chip rebonding, we consider the cutting conditions described in Table 4.5. We tested with different MWF concentrations such as pure water, CIMTECH 310-1%, CIMTECH 310-3%, CIMTECH 310-5%, CIMTECH 320-1%, CIMTECH 320-3%, and CIMTECH 320-5%, for each test run in Table 4.5.

Table 4.5 Test matrix for various concentrations with different kinds of MWF

Test-Run	Feed Rate (mm/rev)	Cutting Speed (m/min)	DOC (mm)
1	0.076	60	0.076
2	0.076	240	0.076
3	0.38	240	0.076
4	0.38	60	0.076

Figure 4.7 shows the results from each test run for various concentrations with different kinds of MWF. The water as MWF does not improve machined surface quality nor does it prevent chip rebonding at the lower feed rate in Figures 4.7 (a) and (b). This is the same result observed in the previous experiment with dry cutting. When we test with the 5% solution of CIMTECH 310 and CIMTECH 320, which percentage of the solution is generally recommended by the manufacturer, we can observe that 5% solutions prevent chip rebonding even at the cutting conditions where chip rebonding usually occurs in dry cutting. When CIMTECH 310-3% and CIMTECH 320-3% are used as MWF, surface quality is also improved and no chip rebonding occurs.

CIMTECH 310-1% and CIMTECH 320-1% show different performance as MWF for chip rebonding occurrence as shown in Figures 4.7 (a) and (b). Although we use the same concentration of MWF with the same cutting conditions, CIMTECH 310-1% creates chip rebonding on the machined surface. CIMTECH 320-1% showed better performance as MWF than CIMTECH 310-1%. From these results, we conclude that the performance of MWF for surface quality does depend on the concentration of MWF and lubricant components. In the following sections, we investigate which components and properties of lubricants produce the different results for chip morphologies and affect chip rebonding occurrence.

(a)

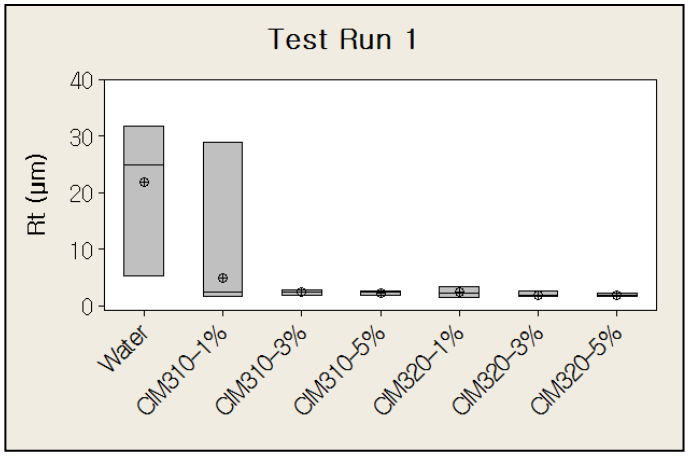

(b)

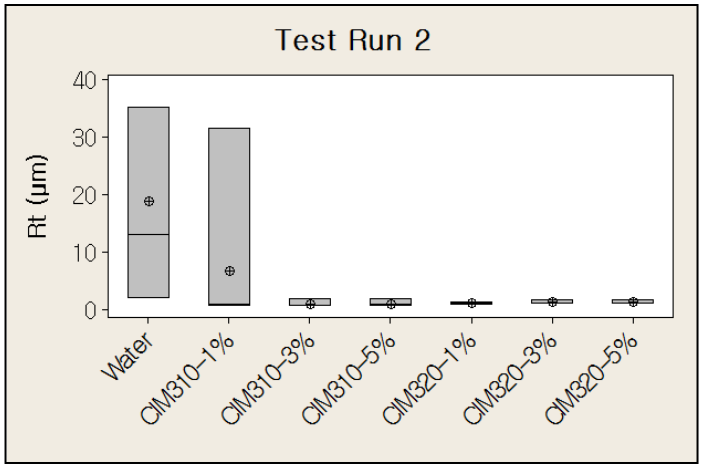

(c)

(d)

Figure 4.7 Test results for various concentrations with different kinds of MWF (a) surface roughness R_t for d = 0.076 mm, f = 0.076 mm/rev, v = 60 m/min (b) surface roughness R_t for d = 0.076 mm, f = 0.076 mm/rev, v = 240 m/min (c) surface roughness R_t for d = 0.076 mm, f = 0.38 mm/rev, v = 240 m/min (d) surface roughness R_t for d = 0.076 mm, f = 0.38 mm/rev, v = 60 m/min

4.4.3 Observation of Chip Morphology with Different Kinds of MWF

In this section, chip morphology at the side edge of the chip is investigated based on the previous test results. In Section 4.4.2, we observed that CIMTECH 310-1% and CIMTECH 320-1% produced different chip rebonding performance at the low feed rate of 0.76 mm/rev. Table 4.6 summarizes the results and cutting conditions according to these different MWFs.

Table 4.6 Test matrix and results with CIMTECH 310-1% and CIMTECH 320-1%

Test Run	MWF	DOC (mm)	Feed Rate (mm/rev)	Cutting Speed (m/min)	Chip Rebonding
1	CIMTech 310-1%	0.076	0.076	60	OXXOX
2		0.076	0.076	240	XOOXO
3	CIMTech 320–1%	0.076	0.076	60	XXXXX
4		0.076	0.076	240	XXXXX

* O: Chip rebonding, X: No chip rebonding

We investigate the torn chip morphologies from each test with CIMTECH 310-1% and CIMTECH 320-1%, because the torn chips at the chip's side edge are the significant factor to cause chip rebonding. Figure 4.8 shows overall chip morphology and magnified torn chip morphology next to the overall chip figure. Under the cutting conditions of test runs 1 and 2, chip rebonding may occur, since the length of the torn chips is long enough to go into the gap between the tool insert and workpiece as shown in Figure 4.9. The geometry is

constructed based on cutting parameters and the measured thickness of rebonded chip around 15 µm from the given cutting conditions. Based on the chip rebonding mechanism described in Chapter 2, chip rebonding may occur in the space around 300 µm between the flowing chip and the chip rebonding position as shown in Figure 4.9. In case of results from test runs 3 and 4, the length of the torn chips is too short for the chip to go into the gap between tool insert and workpiece, when uncut chip section is cut away; the length of torn chips from Test 3 and Test 4 as shown in Figure 4.8 (c) and (d) are much smaller than 300 µm.

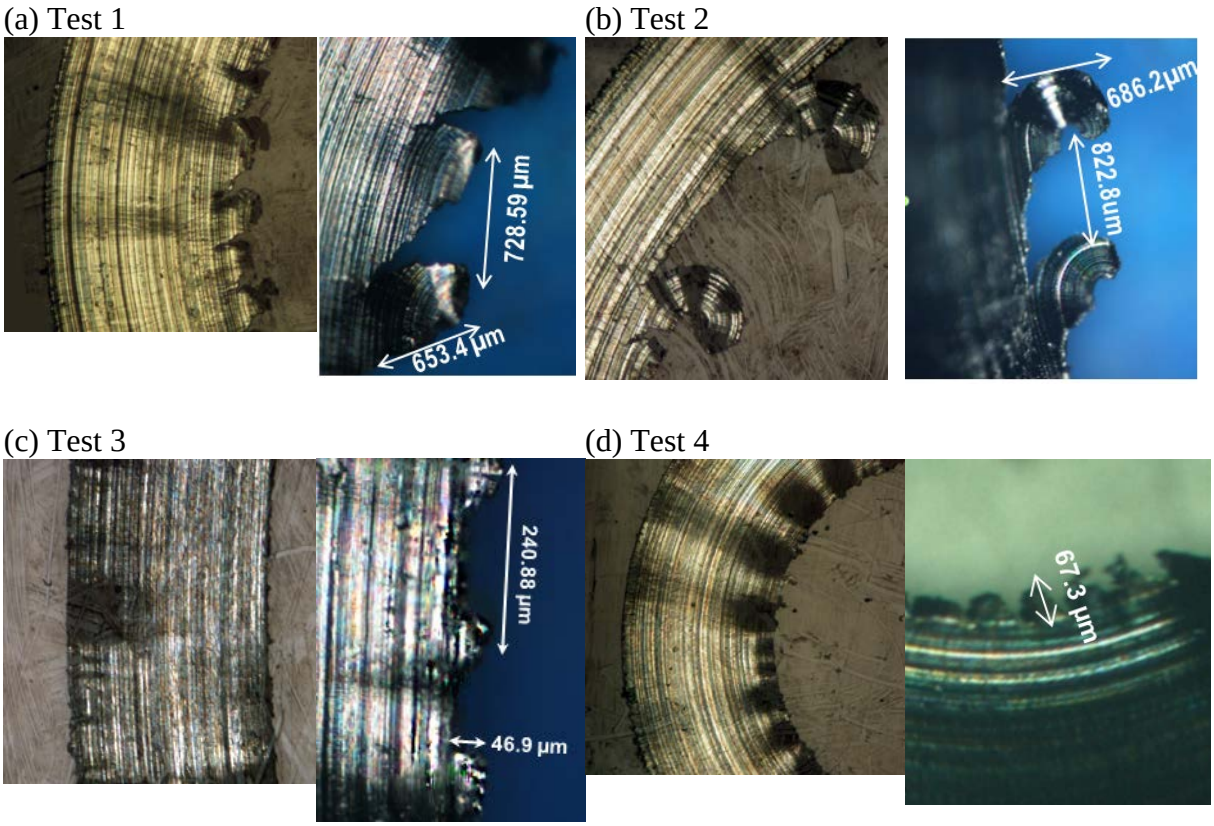

Figure 4.8 Torn chips morphology at the side edge of chip from each test

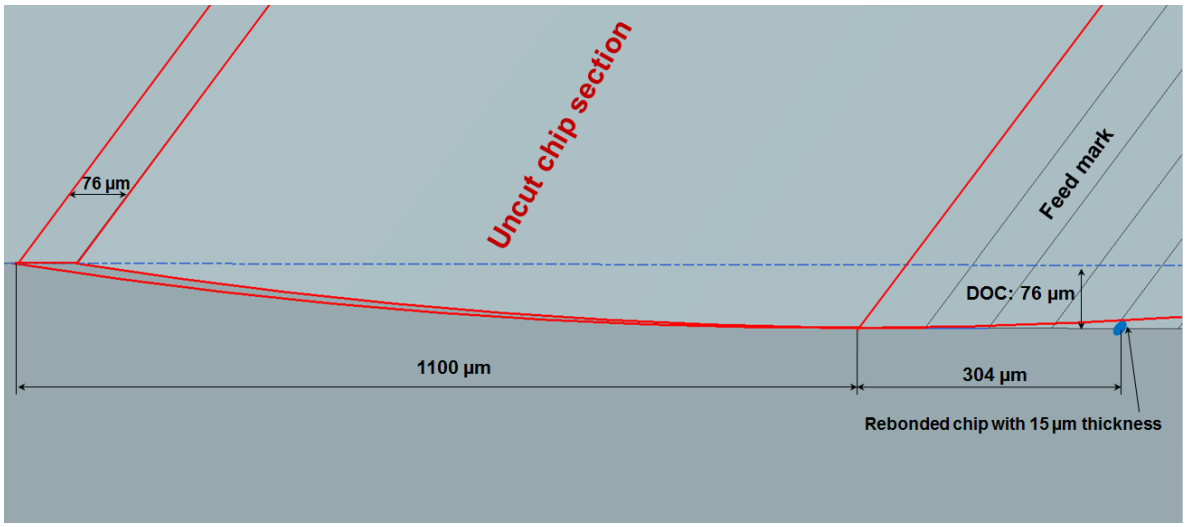

Figure 4.9 Torn chip geometry for chip rebonding occurrence

4.5 Effect of Lubricant Components on Chip Rebonding Occurrence

In Section 4.4.3, test results demonstrated that the performance of the MWF changes chip morphology at the chip's side edge, which decides the occurrence of chip rebonding. In order to investigate which lubricant components produce results presented in Section 4.4.3, each component for CIMTECH 310 and CIMTECH 320 are compared in Table 4.7.

Triethanolamine is used for adjustment and maintenance of pH in lubricants. Neodecanoic acid is used as corrosion inhibitor in synthetic lubricants. Monoisopropanolamine is a multifunctional intermediate for surfactants, dispersion and cross-linking agents as well as pH buffers. Chloride is used for EP additive. Most components in both lubricants have similar amount except the component of nonanoic acid. Only CIMTECH 320 contains nonanoic acid that is used to increase viscosity [106]. Because of this component, CIMTECH 320 has higher viscosity than CIMTECH 310 as

shown in Table 4.8. By comparing these two lubricants, we hypothesize that the viscosity of a lubricant is a main contributor on chip rebonding occurrence.

Table 4.7 Lubricant components in CIMTECH 310 and CIMTECH 320

Component	CIMTECH 310	CIMTECH 320
Triethanolamine (%)	10~30	10-30
Neodecanoic Acid (%)	5~10	7-13
Monoisopropanolamine (%)	1-5	1-5
Nonanoic (Pelargonic) Acid (%)	0	1-5
Chloride (%)	0.09	0.09

Data sources: http://www.cimcool.com

Table 4.8 Physical properties for CIMTECH 310 and CIMTECH 320

	CIMTECH 310	CIMTECH 320
Viscosity (cSt) at 40ºC	24.6	36.8
pH (Mix)	7.8	7.8
Boiling Point (ºC)	100	100
Specific Gravity	1.1	1.1

Data sources: http://www.cimcool.com

To confirm that proper viscosity of lubricant prevents chip rebonding, nonanoic acid is added into CIMTECH 310 to increase viscosity. In Figure 4.10, viscosity is measured by a Brookfield viscometer according to the ratio of CIMTECH 310 to nonanoic acid, and the results show that viscosity increases linearly with increasing nonanoic acid concentration.

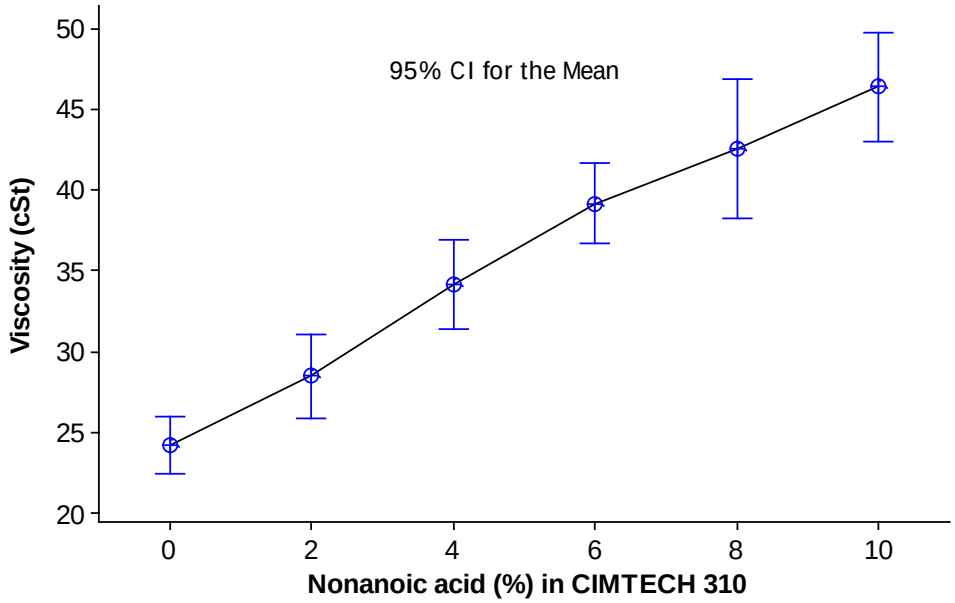

Figure 4.10 Viscosity at 25ºC according to nonanoic acid in CIMTECH 310

Since 1% solution of CIMTECH 310 produces chip rebonding for some tests in Table 4.6, 0.5% solution of CIMTECH 310 is used, which produces chip rebonding for every test. We increase the viscosity of 0.5% solution of CIMTECH 310 until chip rebonding disappears. As shown in Table 4.9, test results show that chip rebonding can be removed by increasing the viscosity of a lubricant. At the same time, we can observe that the cutting force is stabilized as viscosity increases in Figure 4.11. The stabilization of cutting force represents that the size of torn chips at the side edge of flowing chip is small enough not to produce chip rebonding at the interface between the tool and workpiece.

Table 4.9 Test results with 0.5% solution of a mixture of CIMTECH 310 and nonanoic acid

Test Run	Viscosity (cSt)	DOC (mm)	Feed Rate (mm/rev)	Cutting Speed (m/min)	Chip Rebonding
1	24.5	0.076	0.076	60	OOOOO
2		0.076	0.076	240	OOOOO
3	27.5	0.076	0.076	60	OOOXO
4		0.076	0.076	240	OOOXO
5	33	0.076	0.076	60	OXOOX
6		0.076	0.076	240	XOOXO
7	38	0.076	0.076	60	XOXXX
8		0.076	0.076	240	OXXOX
9	43	0.076	0.076	60	XXXXX
10		0.076	0.076	240	XXXXX
11	47	0.076	0.076	60	XXXXX
12		0.076	0.076	240	XXXXX

* O: Chip rebonding, X: No chip rebonding

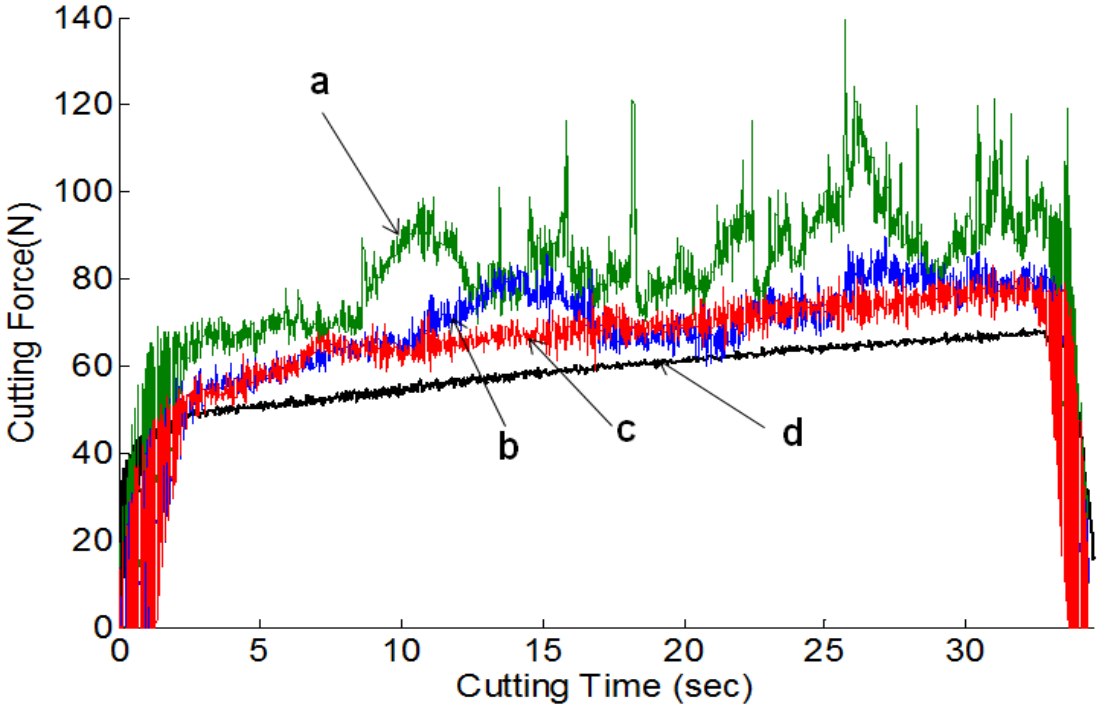

Figure 4.11 Cutting forces according to viscosity for d = 0.076 mm, f = 0.076 mm/rev, v = 240 m/min (a) viscosity of 24.5 cSt (b) viscosity of 33 cSt (c) viscosity of 38 cSt (d) viscosity of 47 cSt

4.6 Conclusions and Discussion

This chapter focuses on the effects of cutting parameters and metal working fluids on chip rebonding occurrence during the face turning of Inconel 718 with a round ceramic insert.

In order to identify the key parameters resulting in chip rebonding, DOE was performed. Our results show that R_t and R_a decrease as the feed rate increases, and that the

feed rate is the most significant parameter in influencing chip flow direction at a given geometry of tool and the range of cutting conditions. We observed the feed rate under 0.38 mm/rev produced curled chip and this flowing chip tangled and hit the surface. These actions produced anomalies such as chip rebonding and scratched on the machined surface. Overall observations of chip rebonding on the machined surface showed that chip rebonding repeatedly occurred along a feed mark and that the chip's side edge was periodically torn and curled. Thus, we confirmed that the low feed rates under 0.38mm/rev had the strongest effect on causing chip rebonding in dry cutting.

In wet cutting, various MWFs including pure water and two kinds of commercial lubricants with varying concentrations were used to investigate the possibility of preventing chip rebonding. Pure water as MWF did not prevent chip rebonding at all, even though water is known to show a good cooling performance. Since temperature at the cutting zone in machining of Inconel 718 goes up to 1300 ºC that is much higher than the boiling point of water, water has limitations for cooling effect.

After testing with various MWFs, we found that chip rebonding occurrence was determined according to the lubricant type, and the concentration and viscosity of MWF. These conditions determine the torn chip size and in turn affect the occurrence of chip rebonding. Even with the same cutting condition, chip rebonding occurrence depends on MWF's performance, and the viscosity of MWF determines its performance. Viscosity can be increased by adding nonanoic acid. When we used the viscosity of 47 cSt, cutting forces are stabilized and chip rebonding completely disappears; appropriate concentration of viscosity decreases friction and temperature between two contacting surfaces.

CHAPTER 5 SUMMARY AND FUTURE WORK

5.1 Summary

This work focused on avoiding chip rebonding phenomenon to improve surface integrity of machined surfaces during machining Inconel 718.

The formation of chip rebonding in machining process can jeopardize the lifetime of the machined components. In order to identify the root causes of chip rebonding, chip rebonding samples were first observed in Chapter 2. From the observation, we found the periodic torn and curled chips at the side edge of the chip are smeared onto the workpiece by the tool. By implementing chip curl blocking device, we confirmed that the chip rebonding formation was mainly due to torn chips.

In Chapter 3, the change of residual stresses caused by chip rebonding in subsurface workpiece was investigated. Residual stresses are considered as the main characteristics of the surface integrity on the machined surface. There are a number of research related to residual stress resulting from cutting; however, little research takes into account the effect of surface defects such as chip rebonding on residual stress. In order to investigate the change of residual stresses caused by chip rebonding, a numerical simulation model was developed. In addition, an analytical model for face turning process of Inconel 718 with a round ceramic tool was used to calculate the cutting forces and the heat fluxes along the cutting edge. As a result, the temperature of the chip was predicted. Next, to calculate

transient residual stresses at the machined subsurface material, 2D FE model considering sequential cuts in turning was used. As a final step, 2D FE model was developed to simulate the effect of chip rebonding on residual stresses and the simulation results were compared with measurements by nanoindenter.

In Chapter 4, DOEs were applied to identify the key variables which influence chip rebonding in dry cutting. At lower feed rates, the chip curls back to the surface of workpiece, while the chip flows away from the cutting region with minimal curl at higher feed rates. Since the chip flow direction is a major factor in determining whether chip rebonding occurs in dry turning of Inconel 718, the feed rate is the dominant parameter for given cutting conditions. In addition, various MWFs including water and two kinds of lubricants with varying concentrations were used to investigate the possibility of preventing chip rebonding. It was found that the viscosity of MWF concentration influences the performance of the MWF and decreases the torn chip size, and in turn avoids the occurrence of chip rebonding with a proper viscosity.

5.2 Contributions

The major contributions of the dissertation are summarized as follows:

1. Among several surface defects, we focused on chip rebonding phenomenon and explained the mechanism of chip rebonding occurrence.
    - We observed individual and overall chip rebonding samples
    - We designed the chip blocker device to verify the hypothesis of chip rebonding occurrence.

- The mechanism of chip rebonding occurrence provided the solution to avoid the root cause of chip rebonding.

2. We analyzed the effect of chip rebonding phenomenon on subsurface residual stresses.
   - We developed a numerical model to predict the changes of residual stresses caused by chip rebonding.
   - We measured residual stress distribution underneath the rebonded chip by nanoindentation method.
   - The FE model is expected to replace the experimental measurement and provide some insight for removing the detrimental effects of chip rebonding on the machined material.

3. We provided how to control the machining conditions to reduce, or even to eliminate chip rebonding.
   - We investigated effects of cutting parameters on chip rebonding occurrence in dry and wet cutting.
   - We investigated effects of MWF on chip rebonding phenomenon.
   - We proposed the proper viscosity of MWF for avoiding chip rebonding occurrence.

5.3 Recommendations for Future Research

To further advance the understanding of chip rebonding phenomenon, the following tasks are worth pursuing in the future:

1. In this dissertation research, only a round insert was tested with a tool holder that has a rake angle and side rake angle of -5°. Because chip flow direction is decided by tool geometry, we need a further investigation for the effects of tool geometry on the chip rebonding phenomenon. This study can provide the information about the optimal geometry to avoid chip rebonding.
2. In order to avoid chip rebonding, a chip blocker device was suggested. It showed the possibility to change chip flow direction mechanically in Chapter 2. This method can be used for machining in a short period time; it can not last long because chip at high temperature and chip flowing force melt the interface between the chip and the chip blocker. Additionally, machining of Inconel 718 produces continuous chip, which results in tangled chip that may cause another surface defects. As another method to avoid chip rebonding mechanically, high-pressure coolant can be used. High-pressure coolant increases the permeation of MWF between two contact surfaces, which will decrease the temperature of chip and increase the lubricity. High-pressure coolant can also adjust chip flow direction and prevent the torn chip from going into the gap between the tool and the machined surface. This study on the effects of pressure in MWF system and applied angle of high pressure can provide a method to avoid chip rebonding.

3. Torn chip model at the side edge of chip can be developed to avoid chip rebonding. Torn chip size and morphology are affected by the performance of MWF and cutting parameters. The temperature model at the chip section can be developed further to analyze the crack initiation and torn chip morphology. This model should reflect the effect of MWF performance. The torn chip model can be validated with the machined chips at the given cutting conditions and it is expected to provide the safe cutting conditions to produce enough short size of torn chips to avoid chip rebonding.

4. The simulation model of chip rebonding occurrence can be developed to define the mechanism of crack initiation on the machined surface with chip rebonding at the low cycle fatigue test. This model can provide the scientific explanation for the material failures near the rebonded chip. In one possible direction, repeated thermal flux can be applied into the chip rebonding simulation model to study effects of thermal fatigue on the material with chip rebonding. Chip rebonding sample can be undertaken low cycle fatigue test and measured residual stresses for the validation. The model is expected to estimate the material failure time with chip rebonding and provide another point of view for workpiece life modeling.

APPENDICES

Appendix A

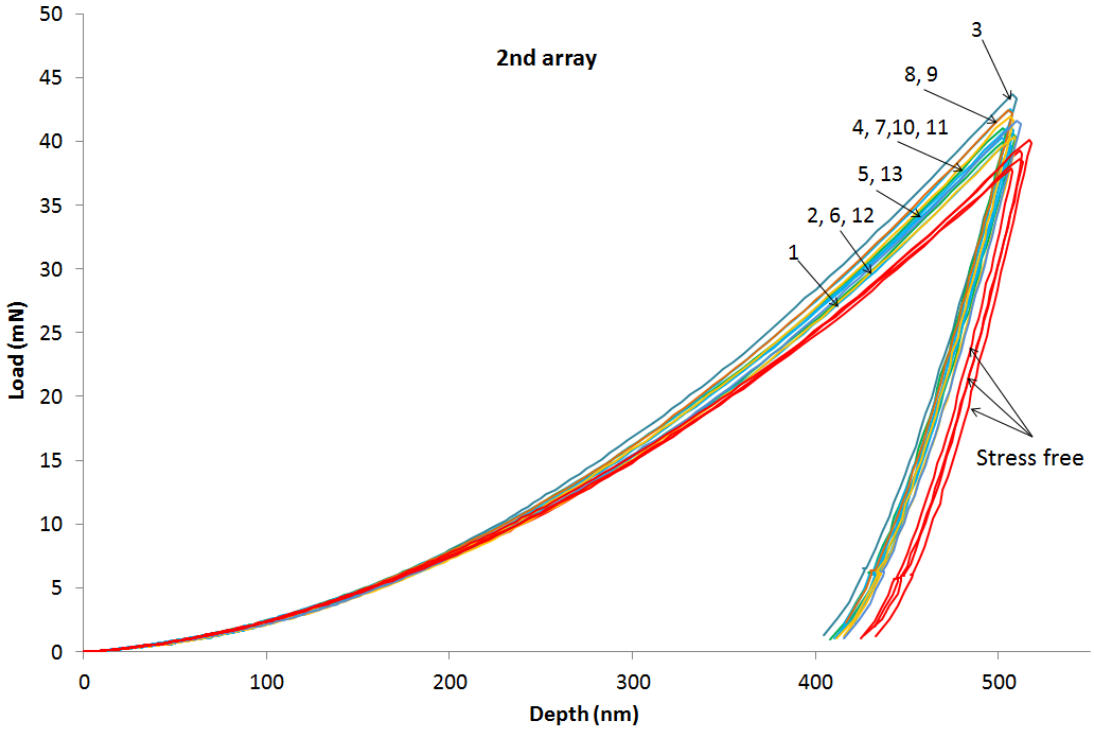

Nanoindentation load-displacement curves for the second array

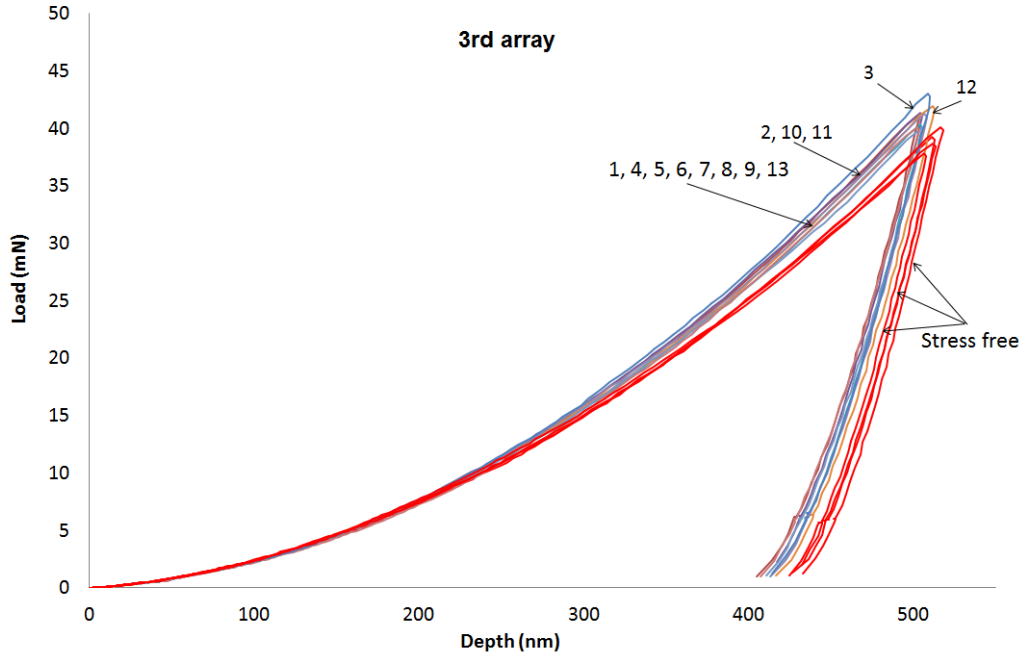

Nanoindentation load-displacement curves for the third array

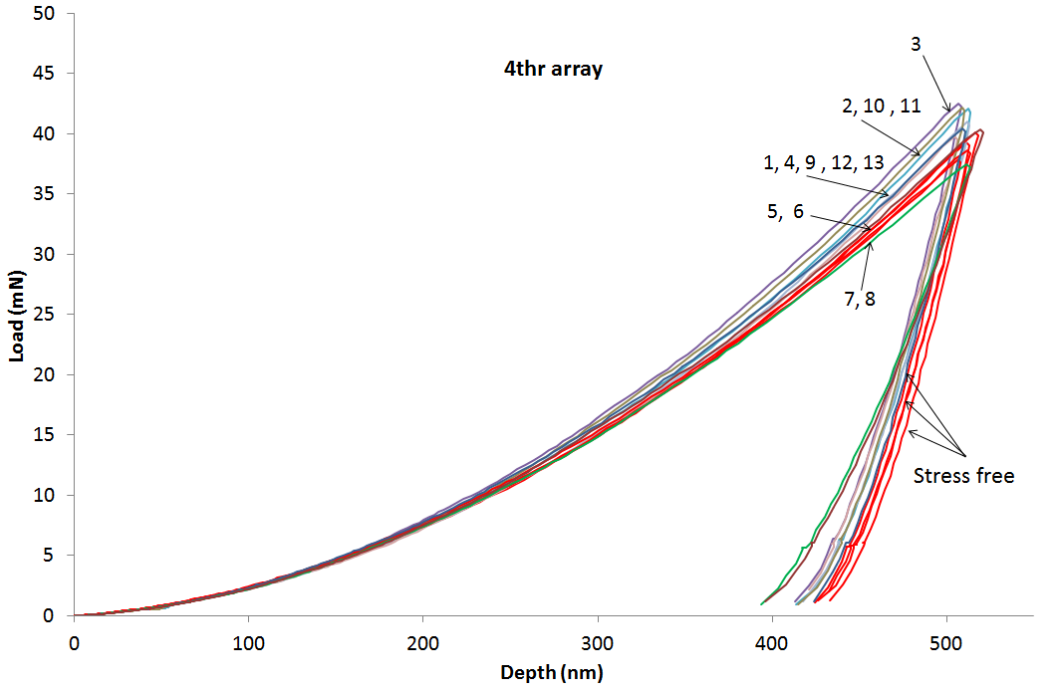

Nanoindentation load-displacement curves for the fourth array

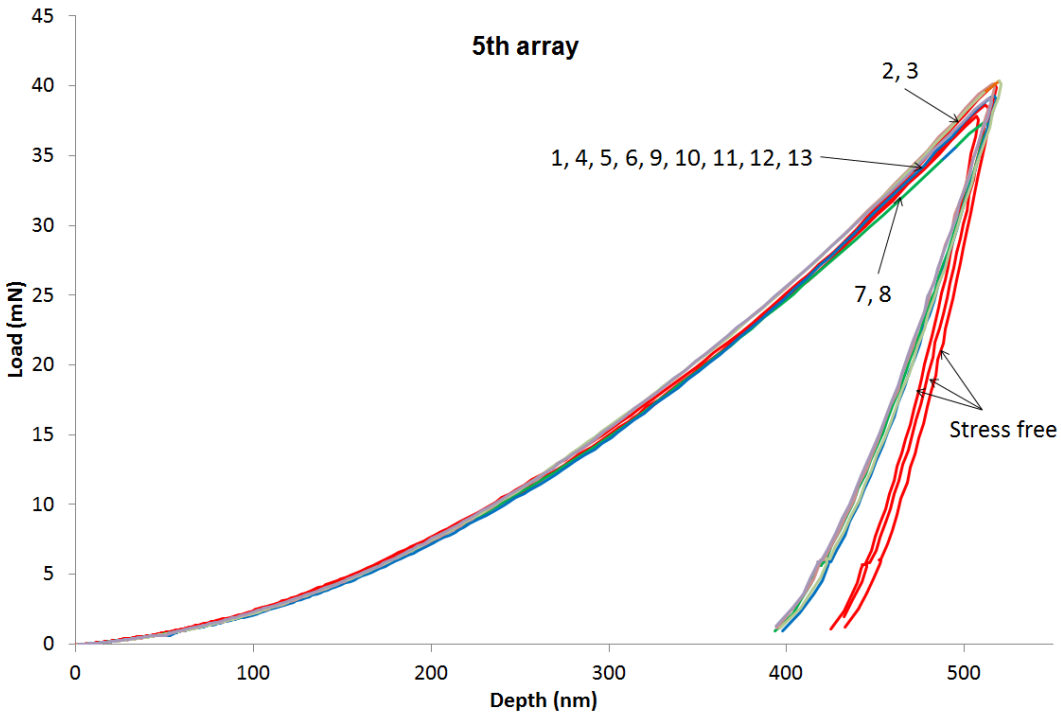

Nanoindentation load-displacement curves for the fifth array

Appendix B

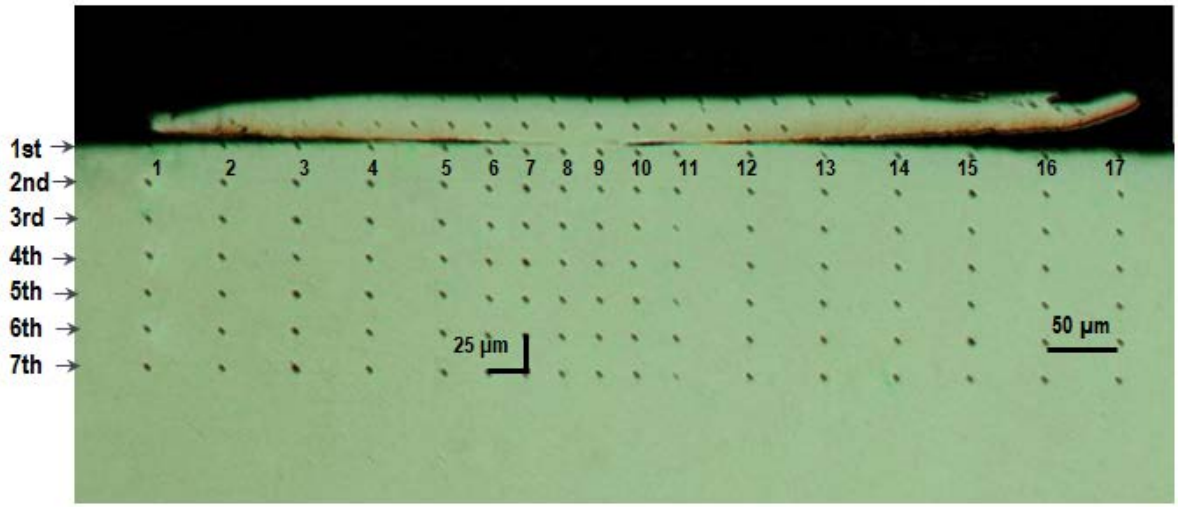

Arrays of indentations under rebonded chip in Inconel 718

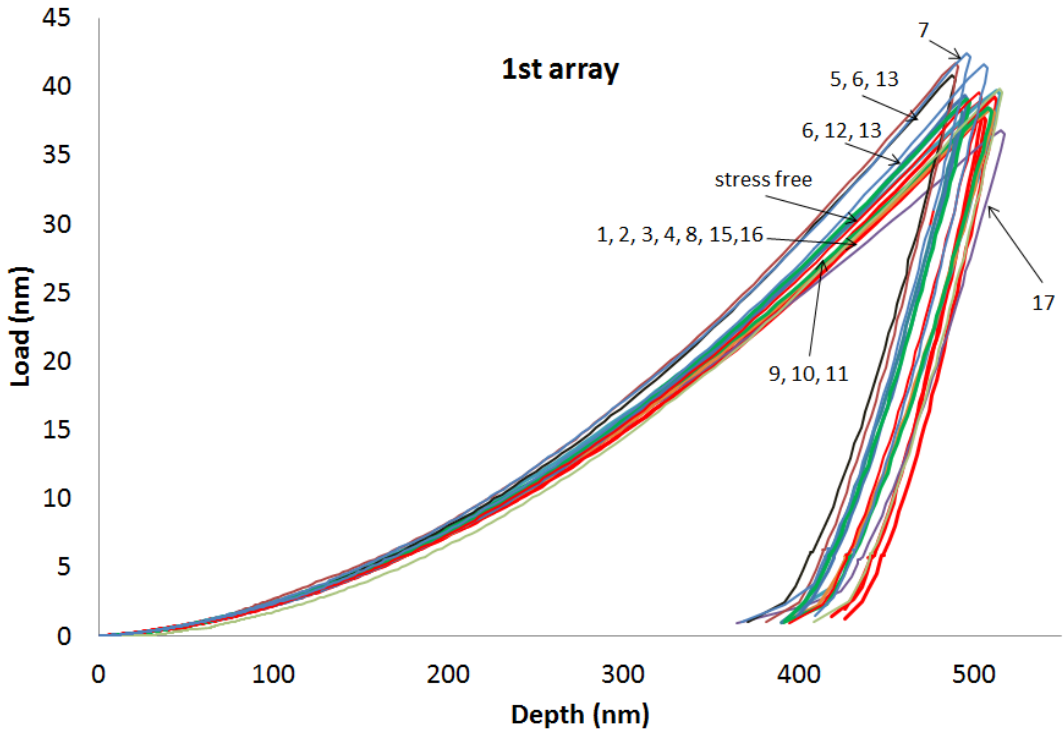

Nanoindentation load-displacement curves for the first array

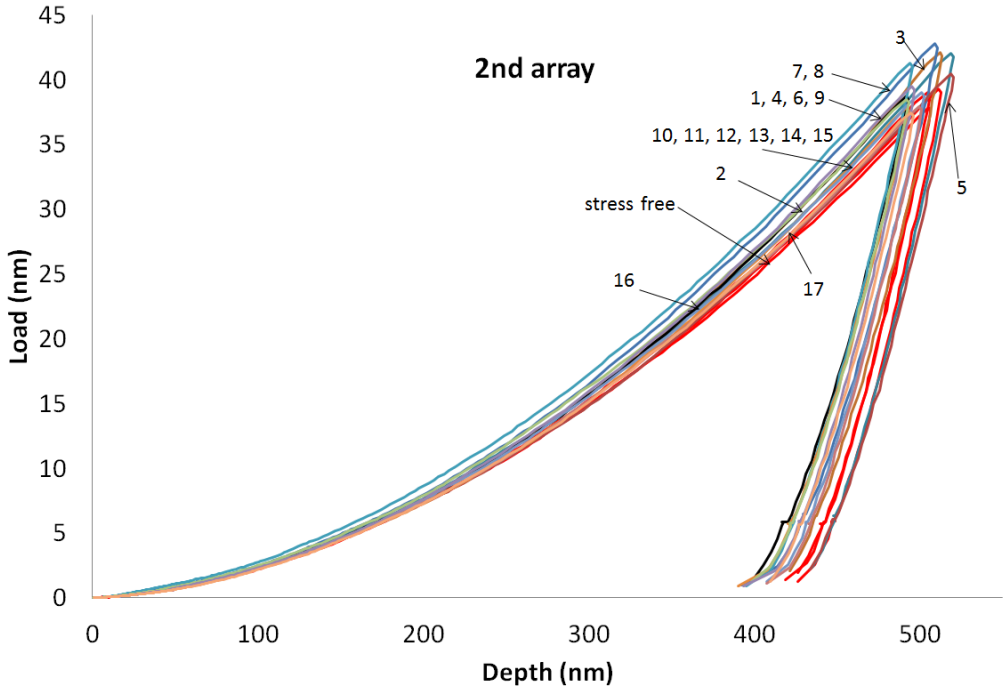

Nanoindentation load-displacement curves for the second array

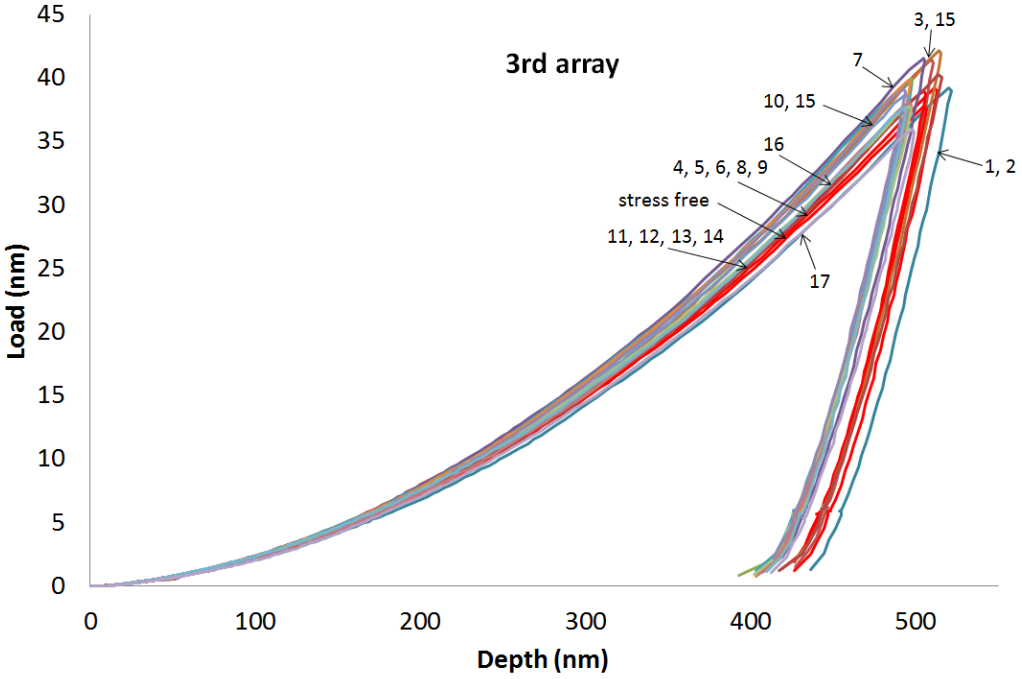

Nanoindentation load-displacement curves for the third array

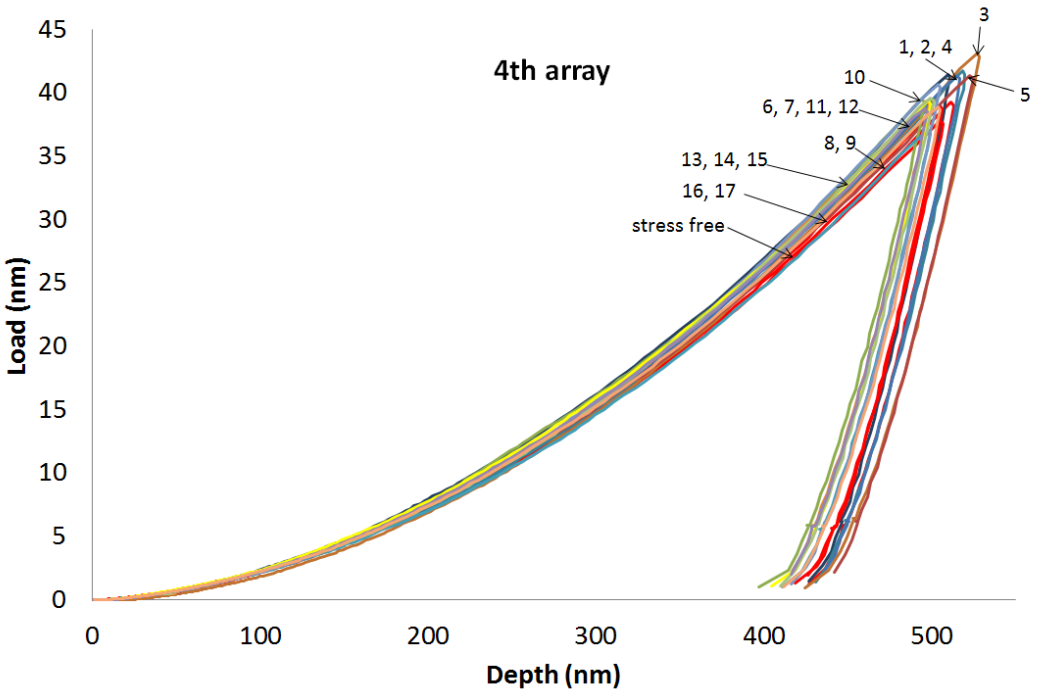

Nanoindentation load-displacement curves for the fourth array

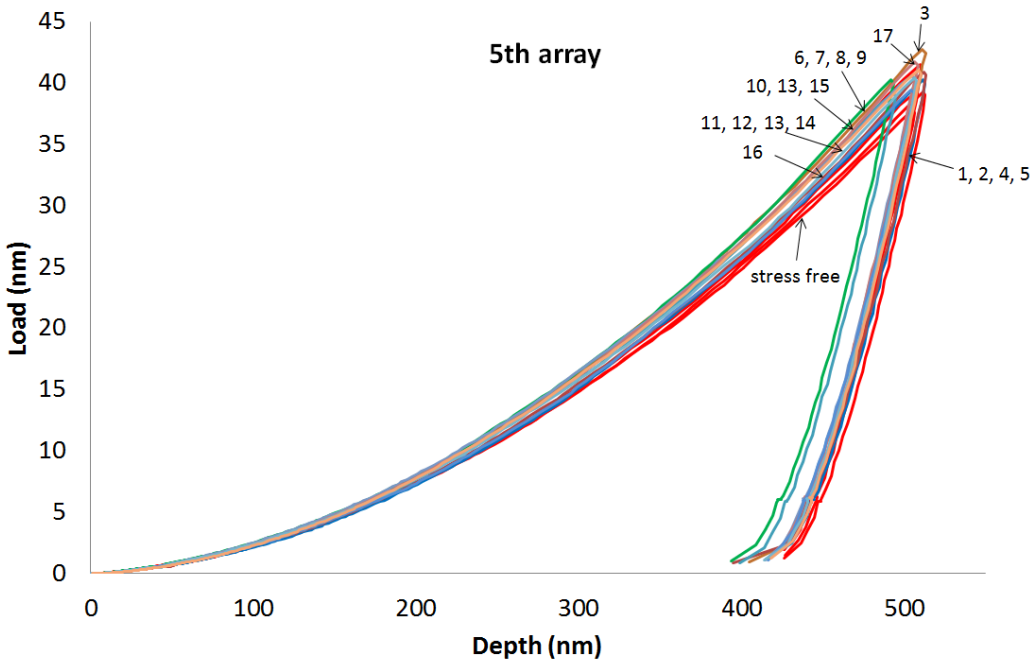

Nanoindentation load-displacement curves for the fifth array

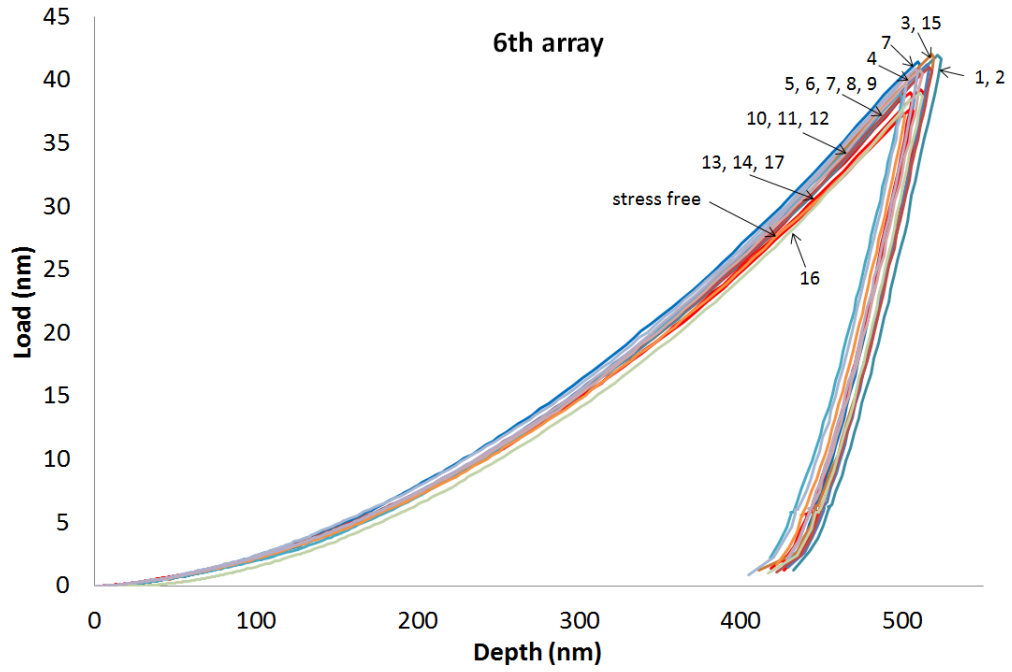

Nanoindentation load-displacement curves for the sixth array

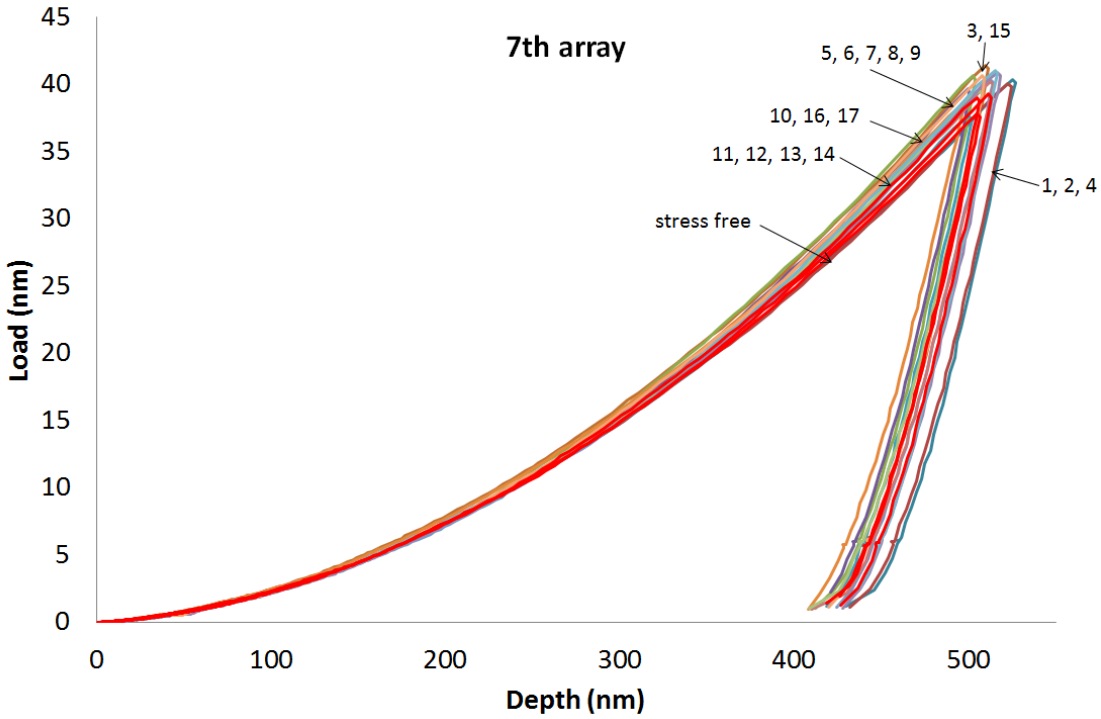

Nanoindentation load-displacement curves for the seventh array

REFERENCES

[1] M. J. Donachie and S. J. Donachie, *Superalloys: A Technical Guide*. ASM International: Materials Park, 2002.

[2] E. O. Ezugwu, Z. M. Wang, and A. R. Machado, "Machinability of Nickel-based Alloys: A Review," *Journal of Materials Processing Technology*, vol. 86, pp. 1-16, 1999.

[3] S. Miller, "Advanced Materials Mean Advanced Engines," *Materials World*, vol. 4, pp. 446-449, 1996.

[4] J. R. Davis, *Nickel, Cobalt, and Their Alloys*: ASM International, 2000.

[5] C. Slama and M. Abdellaoui, "Structural Characterization of the Aged Inconel 718," *Journal of Alloys and Compounds*, vol. 306, pp. 277-284, 2000.

[6] J. C. Lippold, S. D. Kiser, and J. N. DuPont, *Welding Metallurgy and Weldability of Nickel-base Alloys*: John Wiley & Sons, 2009.

[7] E. O. Ezugwu, R. B. Da Silva, J. Bonney, and A. R. Machado, "Evaluation of the Performance of CBN Tools when Turning Ti-6Al-4V Alloy with High Pressure Coolant Supplies," *International Journal of Machine Tools and Manufacture*, vol. 45, pp. 1009-1014, 2005.

[8] H. Schulz, "High-Speed Milling of Dies and Moulds - Cutting Conditions and Technology," *CIRP Annals - Manufacturing Technology*, vol. 44, pp. 35-38, 1995.

[9] M. Rahman, Z. G. Wang, and Y. S. Wong, "A Review on High-Speed Machining of Titanium alloys," *JSME International Journal, Series C* vol. 49, pp. 11-20, 2006.

[10] A. R. C. Sharman, J. I. Hughes, and K. Ridgway, "Workpiece Surface Integrity and Tool Life Issues When Turning Inconel 718™ Nickel Based Superalloy," *LMST*, vol. 8, pp. 399-414, 2004.

[11] R. S. Pawade, S. S. Joshi, P. K. Brahmankar, and M. Rahman, "An Investigation of Cutting Forces and Surface Damage in High-Speed Turning of Inconel 718," *Journal of Materials Processing Technology*, vol. 192–193, pp. 139-146, 2007.

[12] A. B. Sadat, M. Y. Reddy, and B. P. Wang, "Plastic Deformation Analysis in Machining of Inconel 718 Nickel-based Superalloy using Both Experimental and

Numerical Methods," *International Journal of Mechanical Sciences,* vol. 33, pp. 829-842, 1991.

[13] A. B. Sadat and M. Y. Reddy, "Surface Integrity of Inconel-718 Nickel-base Superalloy using Controlled and Natural Contact Length Tools. part I: Lubricated," *Experimental Mechanics,* vol. 32, pp. 282-288, 1992.

[14] M. Field and J. F. Kahles, "Review of Surface Integrity of Machined Components," *Annals of CIRP,* vol. 20, pp. 153-162, 1971.

[15] A. L. Mantle and D. K. Aspinwall, "Surface Integrity and Fatigue Life of Turned Gamma Titanium Aluminide," *Journal of Materials Processing Technology,* vol. 72, pp. 413-420, 1997.

[16] W. D. Feist, F. Niklasson, and K. M. Fox, "The Influence of Manufacturing Anomalies on Fatigue Performance of Critical Rotating Parts in the Aero-Engine," MANHIRP G4RD-CT2000-00400, 2002.

[17] E. O. Ezugwu and S. H. Tang, "Surface Abuse when Machining Cast Iron (G-17) and Nickel-base Superalloy (Inconel 718) with Ceramic Tools," *Journal of Materials Processing Technology,* vol. 55, pp. 63-69, 1995.

[18] R. S. Pawade, S. S. Joshi, and P. K. Brahmankar, "Effect of Machining Parameters and Cutting Edge Geometry on Surface Integrity of High-Speed Turned Inconel 718," *International Journal of Machine Tools and Manufacture,* vol. 48, pp. 15-28, 2008.

[19] S. Ranganath, C. Guo, and S. Holt, "Experimental Investigations into the Carbide Cracking Phenomenon on Inconel 718 Superalloy Material," *ASME Conference Proceedings,* vol. 2009, pp. 33-39, 2009.

[20] S. J. Findlay and N. D. Harrison, "Why Aircraft Fail," *Materials Today,* vol. 5, pp. 18-25, 2002.

[21] G. S. Campbell and R. Lahey, "Survey of Serious Aircraft Accidents Involving Fatigue Fracture," *International Journal of Fatigue,* vol. 6, pp. 25-30, 1984.

[22] R. P. Gangloff and R. O. Ritchie, "Environmental Effects Novel to the Propagation of Short Fatigue Cracks " in *Fundamentals of Deformation and Fracture. Eshelby Memorial Symposium.*, Sheffield, Engl, pp. 529-558, 1985.

[23] N. Narutaki, Y. Yamane, K. Hayashi, T. Kitagawa, and K. Uehara, "High-Speed Machining of Inconel 718 with Ceramic Tools," *CIRP Annals - Manufacturing Technology,* vol. 42, pp. 103-106, 1993.

[24] T. Kitagawa, A. Kubo, and K. Makawa, "Temperature and Wear of Cutting Tools in High-Speed Machining of Inconel 718 and Ti-6Al-6V-2Sn," *Wear*, vol. 202, pp. 142-148, 1997.

[25] I. A. Choudhury and M. A. El-Baradie, "Machinability of Nickel-base Super Alloys: A General Review," *Journal of Materials Processing Technology*, vol. 77, pp. 278-284, 1998.

[26] P. M. Noaker, "Super Speeds for Superalloys," *Manufacturing Engineering*, vol. 107, pp. 63-68, 1991.

[27] R. Arunachalam and M. A. Mannan, "Machinability of Nickel-Based High Temperature Alloys," *Machining Science and Technology*, vol. 4, pp. 127-168, 2000.

[28] E. O. Ezugwu, J. Bonney, and K. A. Olajire, "Evaluation of the Machinability of Nickel-base, Inconel 718, Alloy with Nano-Ceramic Cutting tools," *Tribology Transactions*, vol. 45, pp. 506-511, 2002.

[29] E. O. Ezugwu, J. Bonney, and Y. Yamane, "An Overview of the Machinability of Aeroengine Alloys," *Journal of Materials Processing Technology*, vol. 134, pp. 233-253, 2003.

[30] N. Richards and D. Aspinwall, "Use of Ceramic Tools for Machining Nickel Based Alloys," *International Journal of Machine Tools and Manufacture*, vol. 29, pp. 575-588, 1989.

[31] J. Vigneau, P. Bordel, and R. Geslot, "Reliability of Ceramic Cutting Tools," *CIRP Annals - Manufacturing Technology*, vol. 37, pp. 101-104, 1988.

[32] G. Bellows, "Applying Surface Integrity Principles in Jet Engine Production " *Metals Engineering Quarterly*, vol. 12, pp. 55-58, 1972.

[33] D. Y. Jang, J. H. Liou, T. R. Watkins, K. J. Kozaczek, and C. R. Hubbard, "Characterization of Surface Integrity in Machined Austenitic Stainless Steel," in *Proceedings of the 1995 ASME International Mechanical Engineering Congress and Exposition*, San Francisco, CA, USA, pp. 399-413, 1995.

[34] B. Scholtes, *Residual Stresses Introduced by Machining* vol. 4. Pergamon Press: Advances in Surface Treatments, 1987.

[35] P. Guegan, A. Poitou, and P. Bremond, "High Speed Experimental Analysis of Orthogonal Planing using High Speed Infrared Camera," in *Thermosense XXVIII*, USA, pp. 62050X-1-62050X-5, 2006.

[36] C. E. Leshock and Y. C. Shin, "Investigation on Cutting Temperature in Turning by a Tool-Work Thermocouple Technique," *Journal of Manufacturing Science and Engineering, Transactions of the ASME,* vol. 119, pp. 502-508, 1997.

[37] M. Bono and J. Ni, "A Method for Measuring the Temperature Distribution along the Cutting Edges of a Drill," *Journal of Manufacturing Science and Engineering, Transactions of the ASME,* vol. 124, pp. 921-923, 2002.

[38] M. E. Merchant, "Fundamentals of Cutting Fluid Action," *Lubrication Engineering,* vol. 6, pp. 163-167, 1950.

[39] M. C. Shaw, N. H. Cook, and P. A. Smith, "Mechanics of Three-Dimensional Cutting Operation," *Transactions of the American Society of Engineers,* vol. 74, pp. 1055-1064, 1952.

[40] P. L. B. Oxley, "Mechanics of Metal Cutting," *International Journal of Machine Tool Design and Research,* vol. 1, pp. 89-97, 1961.

[41] M. E. Merchant, "Mechanics of the Metal Cutting Process. I. Orthogonal Cutting and a Type 2 Chip," *Journal of Applied Physics,* vol. 16, pp. 267-275, 1945.

[42] A. Kumar Pal, A. Bhattacharyy, and G. Chandra Sen, "Investigation of the Torque in Drilling Ductile Materials," *International Journal of Machine Tool Design and Research,* vol. 4, pp. 205-221, 1965.

[43] W. J. Endres, J. W. Sutherland, R. E. DeVor, and S. G. Kapoor, "A Dynamic Model of the Cutting Force System in the Turning Process," in *Winter Annual Meeting of the American Society of Mechanical Engineers*, Dallas, TX, USA, pp. 193-212, 1990.

[44] E. J. A. Armarego and J. D. Wright, "Predictive Models for Drilling Thrust and Torque - a Comparison of Three Flank Configurations," *CIRP Annals - Manufacturing Technology,* vol. 33, pp. 5-10, 1984.

[45] F. M. Gu, S. G. Kapoor, and R. E. DeVor, "A Cutting Force Model for Face Milling with a Step Cutter " *Trasactions of the North American Manufacturing Research Institution of SME,* vol. 20, pp. 361-367, 1992.

[46] J. W. Sutherland, G. Subramani, M. J. Kuhl, R. E. DeVor, and S. G. Kapoor, "An Investigation into the Effect of Tool and Cut Geometry on Cutting Force System Prediction Models," *Proc. 16th NAMRC,* pp. 264-272, 1988.

[47] V. Chandrasekharan, S. G. Kapoor, and R. E. DeVor, "Mechanistic Approach to Predicting the Cutting Forces in Drilling: With Application to Fiber-Reinforced Composite Materials," in *Proceedings of the ASME Winter Annual Meeting*, New Orleans, LA, USA, pp. 33-51, 1993.

[48] R. F. Hamade, C. Y. Seif, and F. Ismail, "Extracting Cutting Force Coefficients from Drilling Experiments," *International Journal of Machine Tools and Manufacture*, vol. 46, pp. 387-396, 2006.

[49] Y. Huang and S. Y. Liang, "Cutting Temperature Modeling based on Non-Uniform Heat Intensity and Partition Ratio," *Machining Science and Technology*, vol. 9, pp. 301-323, 2005.

[50] E. Lee and B. Shaffer, "The Theory of Plasticity Applied to a Problem of Machining," *Journal of applied mechanics*, vol. 18, pp. 405-413, 1951.

[51] Y. B. Guo, W. Li, and I. S. Jawahir, "Surface Integrity Characterization and Predicition in Machining of Hardened and Difficult-to-Machine Alloys: a State-of-Art Research Review and Analysis," *Machining Science and Technology*, vol. 13, pp. 437-470, 2009.

[52] E. K. Henriksen, "Residual Stresses in Machined Surfaces," *American Society of Mechanical Engineers*, vol. 73, pp. 69-76, 1951.

[53] P. Leskovar and J. Peklenik, "Influences Affecting the Surface Integrity in the Cutting Process," *CIRP Annals - Manufacturing Technology*, vol. 31, pp. 447–450, 1982.

[54] C. R. Liu and M. M. Barash, "Variables Governing Patterns of Mechanical Residual Stress in a Machined Surface," *Journal of Engineering for Industry* vol. 104, pp. 257-264, 1982.

[55] K. Jacobus, R. E. DeVor, and S. G. Kapoor, "Machining-Induced Residual Stress: Experimentation and Modeling," *Journal of Manufacturing Science and Engineering*, vol. 122, pp. 20-31, 2000.

[56] E. Brinksmeier, J. T. Cammett, W. Koenig, P. Leskovar, J. Peters, and H. K. Toenshoff, "Residual stress-Measurement and causes in machining progresses," *CIRP Annals - Manufacturing Technology*, vol. 31, pp. 491-510, 1982.

[57] M. H. El-Axir, "A Method of Modeling Residual Stress Distribution in Turning for Different Materials," *International Journal of Machine Tools and Manufacture*, vol. 42, pp. 1055-1063, 2002.

[58] S. Mittal and C. R. Liu, "A Method of Modeling Residual Stresses in Superfinish Hard Turning," *Wear*, vol. 218, pp. 21-33, 1998.

[59] D. A. Axinte and R. C. Dewes, "Surface Integrity of Hot Work Tool Steel after High Speed Milling-Experimental Data and Empirical Models," *Journal of Materials Processing Technology*, vol. 127, pp. 325-335, 2002.

[60] R. Komanduri and Z. B. Hou, "Thermal Modeling of the Metal Cutting Process - Part I: Temperature Rise Distribution due to Shear Plane Heat Source," *International Journal of Mechanical Sciences,* vol. 42, pp. 1715-1752, 2000.

[61] R. Komanduri and Z. B. Hou, "Thermal Modeling of the Metal Cutting Process - Part II: Temperature Rise Distribution due to Frictional Heat Source at the Tool-Chip Interface," *International Journal of Mechanical Sciences,* vol. 43, pp. 57-88, 2001.

[62] R. Komanduri and Z. B. Hou, "Thermal Modeling of the Metal Cutting Process - Part III: Temperature Rise Distribution due to the Combined Effects of Shear Plane Heat Source and the Tool-Chip Interface Frictional Heat Source," *International Journal of Mechanical Sciences,* vol. 43, pp. 89-107, 2001.

[63] D. Ulutan, B. Erdem Alaca, and I. Lazoglu, "Analytical Modelling of Residual Stresses in Machining," *Journal of Materials Processing Technology,* vol. 183, pp. 77-87, 2007.

[64] D. Ulutan, M. Sima, and T. Özel, "Prediction of Machining Induced Surface Integrity Using Elastic-Viscoplastic Simulations and Temperature-Dependent Flow Softening Material Models in Titanium and Nickel-Based Alloys," *Advanced Materials Research* vol. 223, pp. 401-410, 2011.

[65] L. Chen, T. I. El-Wardany, and W. C. Harris, "Modelling the Effects of Flank Wear Land and Chip Formation on Residual Stresses," *CIRP Annals - Manufacturing Technology,* vol. 53, pp. 95-98, 2004.

[66] C. R. Liu and Y. B. Guo, "Finite Element Analysis of the Effect of Sequential Cuts and Tool–Chip Friction on Residual Stresses in a Machined layer," *International Journal of Mechanical Sciences,* vol. 42, pp. 1069-1086, 2000.

[67] K. C. Ee, O. W. Dillon Jr, and I. S. Jawahir, "Finite Element Modeling of Residual Stresses in Machining Induced by Cutting using a Tool with Finite Edge Radius," *International Journal of Mechanical Sciences,* vol. 47, pp. 1611-1628, 2005.

[68] G. R. Johnson and W. H. Cook, "A Constitutive Model and Data for Metals Subjected to Large Strains, High Strain Rates and High Temperatrues," in *Proceedings of 7th International Symposium on Ballistics,* The Netherlands, pp. 541-547, 1983.

[69] R. Sievert, H. D. Noack, A. Hamann, P. Loewe, K. N. Singh, G. Kuenecke, R. Clos, U. Schreppel, P. Veit, E. Uhlmann, and R. Zettier, "Simulation der Spansegmentierung beim Hochgeschwindigkeits-Zerspanned unter Berücksichtigung duktiler Schädigung," *Techniche Mechanik,* vol. 23, pp. 216-233, 2003.

[70] J. N. Sweet, E. P. Roth, and M. Moss, "Thermal Conductivity of Inconel 718 and 304 Stainless Steel," *International Journal of Thermophysics,* vol. 8, pp. 593-606, 1987.

[71] V. Suresh Babu, A. S. Paviovic, and M. S. Seehra, "Oxidation Characteristics and Thermal Expansion of Inconel Alloy 718 from 300 K to 1273 K," in *Superalloys 718, 625, 706 and Various Derivatives. Proceedings of the International Symposium*, Warrendale, PA, USA, pp. 689-693, 1997.

[72] C. R. Brooks, M. Cash, and A. Garcia, "The Heat Capacity of Inconel 718 from 313 to 1053 K," *Journal of Nuclear Materials*, vol. 78, pp. 419-421, 1978.

[73] G. Pottlacher, H. Hosaeus, E. Kaschnitz, and A. Seifter, "Thermophysical Properties of Solid and Liquid Inconel 718 Alloy," *Scandinavian Journal of Metallurgy,* vol. 31, pp. 161-168, 2002.

[74] G. R. Johnson and W. H. Cook, "Fracture Characteristics of Three Metals Subjected to Various Strains, Strain Rates, Temperatures and Pressures," *Engineering Fracture Mechanics,* vol. 21, pp. 31-48, 1985.

[75] K. N. Singh, R. Clos, U. Schreppel, P. Veit, A. Hamann, D. Klingbeil, R. Sievert, and G. Künecke, "Versagens Simulation Dynamisch Belasteter Proben Mit Unterschiedlichen Mehrachsigkeitszuständen unter Verwendung des Johnson-Cook-versagens Modells frü eine Nickelbasislegierung," *Techniche Mechanik,* vol. 23, pp. 205-215, 2003.

[76] P. J. Withers and H. K. D. H. Bhadeshia, "Residual Stress Part 1 - Measurement Techniques," *Materials Science and Technology,* vol. 17, pp. 355-365, 2001.

[77] "General Area Detector Diffraction System Version 4.0 Usuer's Manual," Bruker Advanced X-ray Solutions, 1999.

[78] Y. M. Huang, Y. Li, K. He, and C. X. Pan, "Micrometre Scale Residual Stress Measurement in Fusion Boundary of Dissimilar Steel Welded Joints using Nanoindenter System," *Materials Science and Technology*, vol. 27, pp. 1453-1460, 2011.

[79] C. A. Charitidis, D. A. Dragatogiannis, E. P. Koumoulos, and I. A. Kartsonakis, "Residual Stress and Deformation Mechanism of Friction Stir Welded Aluminum Alloys by Nanoindentation," *Materials Science and Engineering A*, vol. 540, pp. 226-234, 2012.

[80] M. K. Khan, M. E. Fitzpatrick, S. V. Hainsworth, and L. Edwards, "Effect of Residual Stress on the Nanoindentation Response of Aerospace Aluminium Alloys," *Computational Materials Science,* vol. 50, pp. 2967-2976, 2011.

[81] N. Ahmed, A. V. Mitrofanov, V. I. Babitsky, and V. V. Silberschmidt, "Analysis of Material Response to Ultrasonic Vibration Loading in Turning Inconel 718," *Materials Science and Engineering: A,* vol. 424, pp. 318-325, 2006.

[82] Y. H. Lee and D. Kwon, "Estimation of Biaxial Surface Stress by Instrumented Indentation with Sharp Indenters," *Acta Materialia,* vol. 52, pp. 1555-1563, 2004.

[83] Y. H. Lee and D. Kwon, "Measurement of Residual-Stress Effect by Nanoindentation on Elastically Strained (100) W," *Scripta Materialia,* vol. 49, pp. 459-465, 2003.

[84] J. A. Bailey, "On Surface Damage during Machining of AISI 4340 Steel," *Wear,* vol. 27, pp. 161-173, 1974.

[85] J. A. Bailey, "Surface Damage during Machining of Annealed 18% Nickel Maraging Steel Part 1 - Unlubricated Conditions," *Wear,* vol. 42, pp. 277-296, 1977.

[86] J. A. Bailey, "Surface Damage during Machining of Annealed 18% Nickel Maraging Steel Part 2 - Lubricated Conditions," *Wear,* vol. 42, pp. 297-303, 1977.

[87] J. A. Bailey, "Surface Damage during Machining of Solution Treated and Aged 18% Nickel Maraging Steel-2. Lubricated Conditions," *Wear,* vol. 44, pp. 371-376, 1977.

[88] W. Koenig, R. Komanduri, H. K. Toenshoff, and G. Ackershott, "Machining of Hard Materials " in *CIRP Annals: Manufacturing Technology, Annals of the International Institution for Production Engineering Research*, Madison, WI, USA, pp. 417-427, 1984.

[89] G. C. Benga and A. M. Abrao, "Turning of Hardened 100Cr6 Bearing Steel with Ceramic and PCBN Cutting Tools," *Journal of Materials Processing Technology,* vol. 143-144, pp. 237-241, 2003.

[90] A. Gatto and L. Iuliano, "Advanced Coated Ceramic Tools for Machining Superalloys," *International Journal of Machine Tools and Manufacture,* vol. 37, pp. 591-605, 1997.

[91] D. Dudzinski, A. Devillez, A. Moufki, D. Larrouquère, V. Zerrouki, and J. Vigneau, "A Review of Developments Towards Dry and High Speed Machining of Inconel 718 Alloy," *International Journal of Machine Tools and Manufacture,* vol. 44, pp. 439-456, 2004.

[92] A. Devillez, F. Schneider, S. Dominiak, D. Dudzinski, and D. Larrouquere, "Cutting Forces and Wear in Dry machining of Inconel 718 with Coated Carbide Tools," *Wear,* vol. 262, pp. 931-942, 2007.

[93] J. P. Byers, *Metalworking Fluids*: Manufacturing Engineering and Materials Processing 2006.

[94] E. S. Nachtman and S. Kalpakjian, *Lubricants and Lubrication in Metalworking Operations*. CRC Press, 1985.

[95] E. L. H. Bastian, I. Rozalsky, and K. F. Schiermeter, "New Developments in Metal Working," *Lubrication Engineering,* vol. 17, pp. 40-47, 1961.

[96] M. C. Shaw, "On Action of Metal Cutting Fluids at Low Speeds," *Wear-Usure-Verschleiss,* vol. 2, pp. 217-227, 1959.

[97] R. W. Bruce, *CRC Handbook of Lubrication: Theory and Practice of Tribology,* vol. 2. Ohio: CRC, 1988.

[98] J. O. Cookson, "Machine Tool Design and Use in Relation to Cutting Fluids," *Annals of Occupational Hygiene,* vol. 14, pp. 181-190, 1971.

[99] P. Menter, W. Harrison, and W. G. Woodin, "Patch Testing of Coolant Fractions," *Journal of Occupational and Environmental Medicine,* vol. 17, pp. 565-568, 1975.

[100] R. Stribek, "Die Wesentlichen Eigenschaften der Gleit-und Rollenlager (The essential conditions of sliding and roller bearings)," *Zeitschrift des Vereines Deutscher Ingenieure,* vol. 46, pp. 1341-1348, 1902.

[101] M. C. Shaw, "Chemico-Physical Role of Cutting Fluid," *Metal Progress,* vol. 42, pp. 85-88, 1942.

[102] R. Mandakovic, "Assessment of EP Additives for Water-Miscible Metalworking Fluids," *Journal of Synthetic Lubrication,* vol. 16, pp. 13-26, 1999.

[103] K. Sorby and K. Tonnessen, "High-pressure Cooling of Face-Grooving Operations in Ti-6Al-4V," *Proceedings of the Institution of Mechanical Engineers, Part B,* vol. 220, pp. 1621-1627, 2006.

[104] A. R. C. Sharman, D. K. Aspinwall, R. C. Dewes, and P. Bowen, "Workpiece Surface Integrity Considerations when Finish Turning Gamma Titanium Aluminide," *Wear,* vol. 249, pp. 473-481, 2001.

[105] E. O. Ezugwu, J. Bonney, R. B. Da Silva, and O. Cakir, "Surface Integrity of Finished Turned Ti-6Al-4V Alloy with PCD Tools using Conventional and High Pressure Coolant Supplies," *International Journal of Machine Tools and Manufacture,* vol. 47, pp. 884-891, 2007.

[106] H. Noureddini and M. L. Rempe, "Pelargonic Acid in Enhanced Oil Recovery," *Journal of the American Oil Chemists' Society*, vol. 73, pp. 939-941, 1996.